Subcellular Investigation of Poxvirus Coinfections and the Impact on the Evolution of Cidofovir Resistance

by

Stephen Zachary Lee

A thesis submitted in partial fulfillment of the requirements for the degree of

Master of Science

in

Virology

Department of Medical Microbiology and Immunology
University of Alberta

Abstract

The Orthopoxviruses remain important re-emerging pathogens, yet there are only two monotherapy antiviral drugs for treating infections. One of the two approved drugs is brincidofovir, which is a prodrug of the acyclic nucleoside phosphonate cidofovir (CDV). CDV inhibits the vaccinia virus DNA polymerase E9, and substitutions in the polymerase confer resistance to the drug. The molecular mechanisms explaining how rare, CDV-resistant (CDV^R) mutants emerge in a population are poorly understood. It is unclear how a rare mutant would ever gain a foothold in a predominantly wildtype population. We were particularly interested in understanding how coinfection between CDV^R and CDV-sensitive (CDV^S) viruses would impact the selection for this rare trait. To this end, we assembled recombinant CDV^R or CDV^S vaccinia viruses expressing EGFP or mKate2 fluorescent proteins fused to the λ bacteriophage cro DNA binding peptide. The cro-EGFP and cro-mKate2 proteins were useful markers to distinguish virus plaques in cell cultures and fluorescent labels for tracking the expansion of virus factories, cytoplasmic sites of replication for poxviruses.

Surprisingly, we showed that in coinfection experiments with CDV treatment, CDV^R viruses appeared to lose their selective advantage over CDV^S viruses. When the viruses replicated in separate cells, there was a strong selection for the CDV^R viruses, which showed that the presence of CDV^S viruses somehow interfered with the selection for CDV^R viruses during coinfection. This prompted us to look at the subcellular behavior of the two viruses using fluorescence microscopy. In single infections with CDV treatment, the CDV^R virus displayed a significantly higher virus factory growth rate than the CDV^S virus. However, when the two viruses were present in the same cell, there was

no difference in the growth of the CDV^R and CDV^S viruses despite the presence of CDV. Additionally, increasing the number of CDV^S viruses in the cell significantly slowed factory growth across both CDV^R and CDV^S viruses. Thus, in a coinfected cell, the CDV^S virus parasitized the growth advantage of the CDV^R virus. This allowed the CDV^S virus to survive the strong selective pressure from CDV treatment. However, when the two viruses replicated in isolated cells, the CDV^S virus could not gain this advantage. Thus, the purifying selection from CDV treatment can only act when viruses remain in separate cells and cannot interact. These data suggest that mechanisms that maintain single infections could play an important role in maintaining fitness in a population of poxviruses.

Preface

I performed all the experiments in this thesis independently except for the cloning and virus purification in Chapter **3.2.** Nolan Bird assisted me in cloning and I am very grateful for his help. Additionally, Dr. Ryan Noyce helped with generating the sequencing data in the Appendix. All introductory figures and figures **4.1**, **4.2**, **5.8**, **5.15**, and **6.1** were generated in BioRender.

Acknowledgments

First, I would like to acknowledge my supervisor, Dr. David Evans. I am extremely grateful for the opportunity to have worked in the Evans Lab. I was relatively inexperienced with virology – I had never taken a virology course or done a plaque assay – and Dr. Evans took me on. I owe much of my knowledge of viruses, how I think about viruses, and general scientific thinking to Dr. Evans' teaching. Thank you for taking a chance on me and for teaching me so much about science, for fostering my research interest in virology, and for your continued support as I look to take on new projects in the field. I gained an interest in virology during my undergrad, but working on this project has turned this interest into a passion. I would also like to acknowledge my supervisory committee, Drs. Rob Ingham and David Marchant. I was lucky to have a very supportive committee. I never felt anxious to hold a committee meeting; I really enjoyed the discussions that we've had and the guidance. I could not have asked for a better committee!

The Evans Lab has been an excellent training environment with excellent people. Thank you to Dr. Ryan Noyce who was the research associate in the lab and is now an independent professor. I am very grateful for his assistance and teaching during my degree. Thank you to Dr. Yi-Chan (James) Lin who was indispensable during my studies and the discussions we had have really shaped the way I approach experiments. Thank you to Nicole Favis for keeping our lab running. The projects in the Evans and Noyce Labs would not succeed without such an awesome lab manager to support the work. Huge thanks to Suzy Wang, who joined the lab at the same time and was a lifeline. I really appreciated having another grad student around not just for socializing, but another person who understood the struggle and was experiencing it themselves. Also, thanks to Nolan Bird, who I had the opportunity to mentor during his final undergrad project. I really appreciated the opportunity to mentor a student, and Nolan was a terrific student who has become a great scientist too.

I could not have succeeded without the exceptional support of various facilities within the Faculty of Medicine & Dentistry. In particular, the MMI Office is a huge reason why the students in our department are successful. Thanks to Tabitha Nguyen and Debbie Doudiet for everything they did and continue to do that helps us in our academic

journeys. The FoMD Cell Imaging Core was also key to this project's success. Thanks to Kiera Smith for training me and for maintaining the confocal microscopes, Dr. Hilmar Strickfaden for his troubleshooting and support to get FISH working, and honorary member Quinten Kieser for teaching me live-cell imaging.

I would finally like to thank everyone in my support network for helping me during this challenging project. The students in MMI have been amazing friends and I have made some truly unforgettable memories. I am extremely grateful for the chance to work and learn alongside everyone in MMI. Special shoutout to the folks in the MMI GSA who continue to do awesome jobs representing our interests in the department. I could not have gotten through this degree without my parents Michael and Maureen Lee. I am forever grateful for everything that you do for me. Thanks to my brother Greg and sister-in-law Betsy for supporting me, for listening to me talk about my studies, and for encouraging me in my studies. And to my partner Grace, thank you for all the love and support. I truly could not have finished my project without your endless encouragement.

Soli Deo Gloria!

Table of Contents

List of Tables

Chapter 2

Chapter 3

List of Figures

Abbreviations

ANOVA	Analysis of variance
BDV	Brincidofovir
BSA	Bovine serum albumin
CDV	Cidofovir
CDV^R	Cidofovir-resistant or Cidofovir resistance
CDV^S	Cidofovir-sensitive
CFP	Cyan fluorescent protein
CMC	Carboxymethylcellulose
Cy5	Cyanine 5
DAPI	4',6-diamidino-2-phenylindole
DMEM	Dulbecco's modified Eagle's media
DMSO	Dimethyl sulfoxide
dsDNA	Double-stranded DNA
DTT	Dithiothreitol
EDTA	Ethylenediaminetetraacetic acid
EdU	5-ethynyl-2'-deoxyuridine
EGFP	Enhanced green fluorescent protein
eIF4F	Eukaryotic initiation factor 4F
EM	Electron Microscopy
EV	Extracellular virion
FBS	Fetal bovine serum
FISH	Fluorescence *in situ* hybridization
FITC	Fluorescein isothiocyanate
FP	Fluorescent protein
GPT	Xanthine guanosine phosphoribosyltransferase
Ig	Immunoglobulin
Kb	Kilobase
mAb	Monoclonal antibody
mCherry	Monomeric Cherry fluorescent protein
MEM	Minimal Essential Media
mKate2	Monomeric Kate2 fluorescent protein
MOI	Multiplicity of infection
MPA	Mycophenolic acid
MPXV	Monkeypox virus
MV	Mature virion
MYXV	Myxoma virus
NHS	Succinimide
LacZ	B-galactosidase
LUT	Lookup table
ORF	Open reading frame
PAA	Phosphonoacetic acid
PCR	Polymerase chain reaction
PBS	Phosphate-buffered saline
PBS-T	PBS with 0.1% v/v Tween-20
PFA	Paraformaldehyde

PFU	Plaque forming units
PKR	Protein kinase R
RFP	Red fluorescent protein
ROI	Region of interest
SIE	Superinfection exclusion
ssDNA	Single-stranded DNA
SSB	Single-stranded DNA binding protein
SSC	Saline sodium citrate
TIF	Tagged image file
TK	Thymidine kinase
TRITC	Tetramethylrhodamine isothiocyanate
Ts	Temperature sensitive
VACV	Vaccinia virus
VDG1.3	Vaccinia virus strain Don Gammon clone 1.3
WR	Western Reserve
YFP	Yellow fluorescent protein

Chapter 1: Introduction

1.1 The *Orthopoxvirus* Genus & Lifecycle

1.1.1 Orthopoxviruses as human pathogens

The *Orthopoxvirus* genus comprises multiple human pathogens of historic and clinical relevance. Currently, the most clinically-relevant *Orthopoxvirus* is monkeypox virus (MPXV), which causes the disease mpox. MPXV is endemic in West Africa but caused multiple zoonotic infections in North America after importation of infected animals (1). In 2022, a global outbreak of MPXV spread the virus to all continents except Antarctica (2–5). Despite the zoonotic threat, there only two antiviral therapies to treat *Orthopoxvirus* infections. As such, developing additional antiviral drugs targeting multiple stages of poxvirus replication is an important goal for biomedical research.

1.1.2. The Poxvirus Lifecycle

The use of vaccinia virus (VACV) as a model has allowed a comprehensive understanding of poxvirus replication (**Figure 1.1**) I will summarize the steps in VACV replication, beginning with entry into the host cell and the eventual assembly of progeny.

1.1.2.1. Entry, Fusion, & Uncoating

The mechanism of poxvirus entry is complex due to the existence of two infectious forms of the virus. The mature virion (MV) is the predominant form of the virus, comprising more than 98% of assembled particles in a cell (6). Extracellular virions (EV) have a different protein composition on the outside of the virion and acquire an additional membrane from the Trans Golgi network. MVs bind to glycosaminoglycans, laminin A, or β1 integrins, permitting broad tissue tropism (7–11). The receptor binding proteins A26, A27, D8, and H3 localize to the flank of the virion (12). Receptor binding combined with phosphatidylserine in the virion membrane initiate mitogenic signaling and macropinocytosis via apoptotic mimicry, engulfing the particle into an endocytic vacuole for fusion (11, 13–15). The acidification of the endosome promotes EV membrane rupture and permits MV fusion, although low pH is not necessary for all VACV strains to undergo fusion (16, 17). VACV assembles a large entry/fusion complex with multiple proteins contributing to fusion (18). The fusion proteins A21, A28, F9, J5, H2, and L1 assemble at the tip of the virion, and this

subdomain is where fusion with the endosomal membrane occurs (19). It remains unclear what conformational changes underlie the fusion process, especially given the multitude of proteins involved.

Membrane fusion delivers three proteinaceous structures into the cytoplasm: the virion core and two lateral bodies. After fusion, core proteins initiate early transcription and extrude early mRNAs (20, 21). Early mRNAs encode important factors involved in uncoating, as inhibiting RNA synthesis prevents core disassembly. RNA-interference identified the viral primase/helicase D5 protein as the critical mediator in the uncoating process (22). Core uncoating also requires the ubiquitin-proteasome system, as the core proteins receive K48-linked ubiquitination during assembly to facilitate uncoating (23). The two lateral bodies flanking the core also undergo proteasome-dependent disassembly (24). This releases important immunomodulatory factors and other enzymes that modify the host cell metabolism to favour virus replication (25).

1.1.2.2. Genome Replication

The poxvirus genome is a linear DNA duplex with covalently-closed ends (26) Historically, *HindIII* restriction endonucleases were used to map the genome, with gene and protein names reflecting the *HindIII* fragment carrying the given sequence. The ends of the genome consist of duplicated inverted terminal repeat regions and a short telomere containing multiple mismatches that create extrahelical loops (26). The hairpin ends result from the resolution of concatemeric intermediates during genome replication (27) (see Chapter **1.2.2.** for further detail). The mismatches in the telomere play an essential role in genome encapsidation (28). Vaccinia virus encodes multiple proteins that replicate the genome. These proteins will be extensively discussed in Chapter **1.2**. The core replication machinery consists of a heterotrimeric complex of the DNA polymerase E9, the uracil DNA glycosylase D4, and A20 linking the two enzymes (29–31). One study reported a replication rate of 86-130 basepairs/second, or a complete genome every 30 minutes (32). The model of genome replication will be discussed in Chapter **1.2.2**.

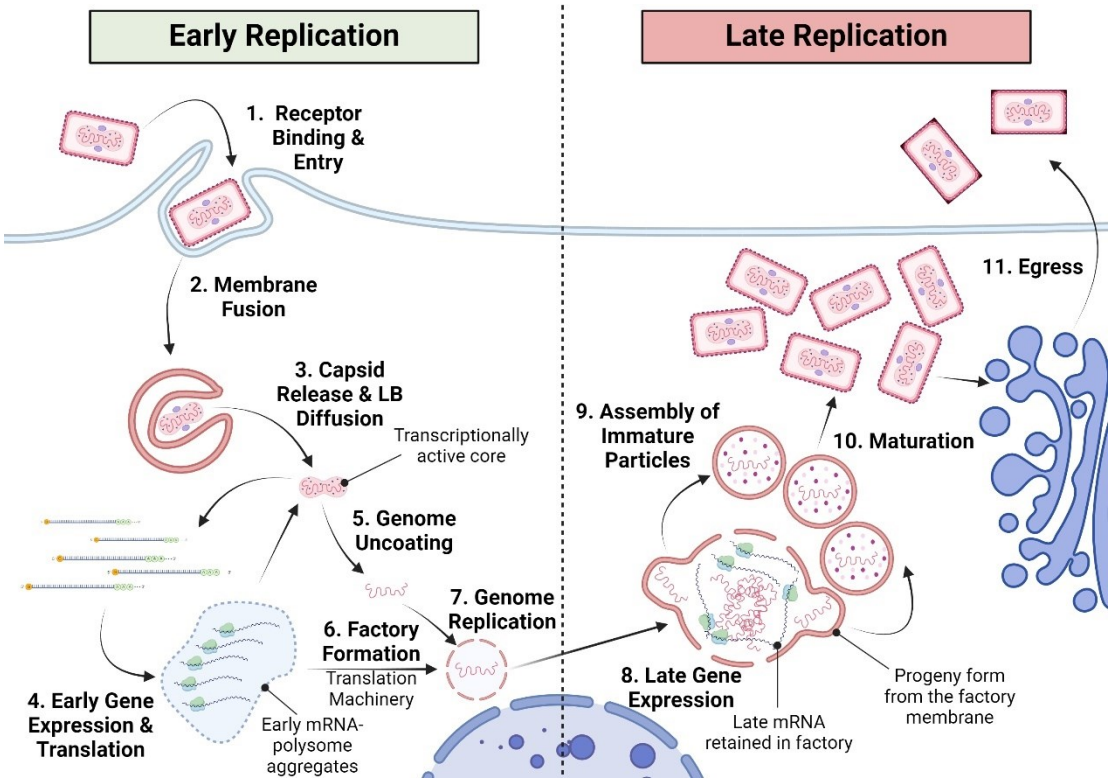

Figure 1.1. Detailed lifecycle of VACV. 1) VACV binds to host cell receptors on the plasma membrane, initiating macropinocytosis, which engulfs the virion into an endosome. 2) Fusion of the virion and endosomal membranes. 3) Fusion allows the capsid to be released into the cytoplasm. The two lateral bodies flanking the capsid undergo proteolytic disassembly, causing proteins to diffuse into the cytoplasm and exert their effects to modulate host functions. 4) The core is transcriptionally active and extrudes mRNA into the cytoplasm. The early transcripts aggregate with polysomes. 5) The capsid undergoes proteolytic disassembly. This requires early gene expression, notably the primase/helicase protein D5 synthesized in the cytoplasm returning to the virion to help uncoating. This releases the genome into the cytoplasm. 6) Multiple viral proteins bind to the genome and assist in nucleating a virus factory. Simultaneously, components of the eIF4F complex relocate into the factory. 7) Multiple viral proteins, in particular E9, D4, A20, I3, G5, D5, and A50 facilitate genome replication. 8) Genome replication allows late gene expression and translation inside the virus factory. 9) Late proteins cannibalize the factory membrane for assembling immature virions. Genome encapsidation is concomitant with virion membrane biogenesis. 10) Proteases cleave the virion core components, resulting in the characteristic MVs. 11) Some MVs transit to the trans Golgi and acquire an additional membrane and viral proteins, generating the EVs.

Poxvirus replication occurs in cytoplasmic virus factories (33). The virus factory forms from pre-replication foci, which include the incoming genome and viral proteins B1, H5, and I3 (34–37). H5 is a soluble protein with non-specific nucleic acid binding and lipid binding capabilities (38, 39). H5 contains multiple intrinsically disordered

motifs, which likely allow self-aggregation of the protein. These biophysical properties suggest that H5 may initiate factory formation. The result is that the endoplasmic reticulum associates with the H5- and I3-bound genome (35, 40). The enclosing ER may concentrate the enzymes and metabolites needed to rapidly replicate the genome.

1.1.2.3. Late Gene Expression, Assembly, & Egress

Genome replication permits late gene expression inside the virus factory. Translation machinery in the virus factory also allows late protein synthesis (41–43). Viral structural proteins associate with the factory membrane, most importantly the A17 and A14 proteins (44, 45). To generate the virion membrane, non-structural proteins L2 (46, 47), A30.5 (48), A11 (49), A6 (50, 51), and H7 (52) create transient breaks in the ER membrane surrounding the virus factory. This generates crescents that eventually join into a single continuous membrane. The A17 and A14 proteins embedded in these membranes associate with D13, which creates a honeycomb-like lattice that induces curvature of the membrane (53). Studies from the Evans and Traktman Laboratories showed that the telomeres are essential during encapsidation and maturation of the virion. During this process, the telomere binding protein I6 may help encapsidate the genome by binding to the A32 ATPase, though precisely how the genome enters the virion is unclear (28, 33, 54, 55). The second telomere binding protein I1 likely initiates maturation as immature virions with encapsidated DNA accumulate when this protein is non-functional (56). After encapsidation, the core protease I7 cleaves A17, which releases the D13 lattice from the virion and allows the membrane to adopt the brick-like shape characteristic of the MV (57). Another protease G1 processes the core proteins, generating the characteristic dumbbell-shaped capsid surrounding the genome, and the F17 protein provides a scaffold for assembling the lateral bodies (24). Following maturation, a portion of the MVs transit to the trans Golgi network and receive a second membrane (58). This process generates EVs that can egress from the cell. However, EVs are rare in the cell and the MV is the predominant infectious form of the virus (6).

1.2. Poxvirus Genome Replication & Homologous Recombination

1.2.1. Proteins involved in genome replication

VACV encodes multiple proteins to replicate the 200 kilobase (kb) genome (**Figure 1.2**). Genome replication is an attractive target for antiviral drug development. Nucleoside analogues can arrest virus growth at a critical stage of replication prior to assembly of progeny virions. This section covers the biochemical properties of the DNA replication machinery and the contributions of VACV proteins to genome replication. Additionally, poxvirus DNA replication and homologous recombination are intrinsically-linked processes. Therefore, an understanding of DNA replication requires some discussion of homologous recombination as a mechanism for DNA repair.

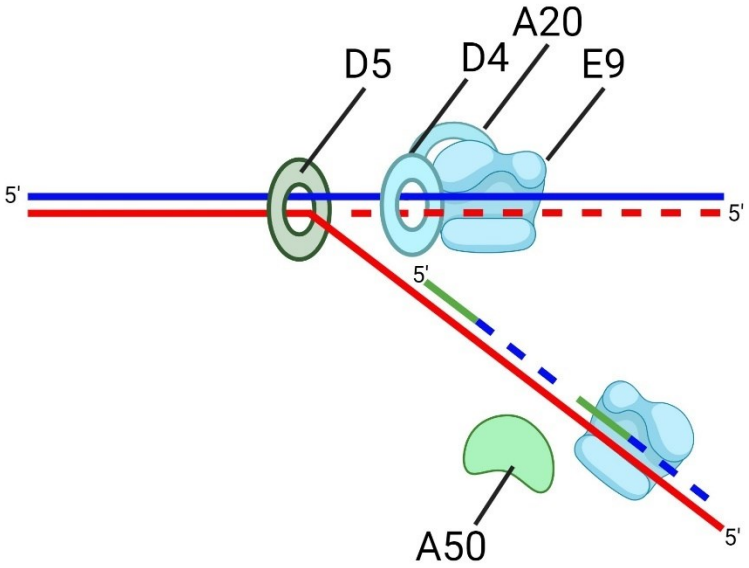

Figure 1.2. VACV replication fork proteins. The D5 helicase unwinds the dsDNA genome and possesses primase activity. The holoenzyme complex consisting of E9, D4, and A20 synthesizes the daughter strand (dash line). The processivity factor forms a forward clamp and associates with the N-terminus of E9. D5 primase can also synthesize short oligonucleotide primers (solid green) for initiating lagging strand synthesis. The A50 DNA ligase repairs the phosphodiester bond in the daughter strand. Host DNA ligase I also contributes to repairing the phosphodiester backbone.

1.2.1.1. DNA polymerase E9

The VACV gene *E9L* encodes a DNA-dependent DNA polymerase called E9. The initial identification of the DNA polymerase and biochemical characterization provided mechanistic insight into its activity and regulation. The earliest report of a virally encoded DNA polymerase showed that DNA polymerase activity increased in VACV-infected cells (59). Initial purification of a DNA polymerase from VACV-infected cells identified a 115-kilodalton protein with polymerase activity (60). Using bacteriophage DNA as a substrate, the authors showed that the DNA polymerase required $MgCl_2$ for maximum activity and functioned in a pH range of 8.0-9.2. The DNA polymerase also possessed exonuclease activity in a 3′-5′ polarity. Later characterization of the DNA polymerase on phage DNA showed that the protein is inherently distributive, possessing an incorporation rate of 500-1200 nucleotides/hour (61). Interestingly, these experiments showed that a template sequence containing secondary structures prevented efficient elongation of the primer strand. Later experiments showed that the incorporation rate of the DNA polymerase increased when single-stranded DNA binding proteins (SSBs) from *Escherichia coli* were added to the reaction (62).

The techniques for identifying the gene encoding the VACV DNA polymerase involved mapping drug resistance or temperature-sensitive (ts) alleles to the VACV genome. Serial passaging VACV in the presence of phosphonoacetic acid (PAA) selected for a PAA-resistant mutant VACV that encoded a DNA polymerase with significantly higher activity than the wildtype polymerase in the presence of PAA (63). The Condit laboratory identified a PAA-resistant mutant with a ts allele at the same position (64). Notably, marker rescue using the HindIII E fragment restored virus replication at high temperature, which showed that the DNA polymerase gene maps to this fragment. The transcript for the DNA polymerase also mapped to the *E9L* gene in S1 nuclease protection assays (65). Analysis of the *E9L* nucleotide sequence showed that the polymerase is a family B polymerase and has homology with the DNA polymerases encoded by Epstein-Barr Virus and Adenovirus (66). Later structural studies with E9 and the MPXV homolog F8 confirmed that E9 is a family B polymerase (29, 67, 68). E9 possesses the characteristic palm, finger, and thumb domains that resemble a closed hand around the template strand. The template strand enters near the N-terminus of the protein,

with multiple residues from the palm domain coordinating the Mg^{2+} ion in the active site (68). Together with the residues from the finger domain, this creates the active site of the polymerase that catalyzes the nucleophilic attack from the 3′OH of the growing strand onto the dNTP in the nucleotide binding pocket.

1.2.1.2. Uracil DNA glycosylase D4 and processivity factor A20

E9 is inherently distributive and requires a processivity factor for efficient synthesis of the genome. The VACV processivity factor consists of the D4 uracil DNA glycosylase and A20 protein (29, 69). D4 catalyzes base excision repair, although abolishing the enzymatic activity of the protein does not affect virus replication *in vitro* (70). However, loss of D4 activity does reduce virulence, which suggests that this activity may be essential *in vivo*. The apparent coupling of DNA replication and base excision repair ensure high fidelity of replication. A20 initially co-purified with the DNA polymerase holoenzyme, showing that A20 was a component of the heterotrimeric complex (71). Temperature-sensitive mutations in the *A20R* gene severely disrupt genome replication and prevent the purification of a processive DNA polymerase (69). X-ray crystallography solved the structure of the DNA polymerase holoenzyme and provided insight into the mechanism of processivity (29). E9 contacts A20 through residues L578 and I582, while D4 and A20 bind through a large interface with several residues (30). Mutagenesis studies showed that substitutions R167A and P173G in D4 or W43A in A20 destabilize the heterodimer. While E9 itself will detach from the template strand, A20 creates a bridge between E9 and D4. These interactions ensure that E9 remains bound to the template during synthesis. Later cryo-EM structures of the MPXV holoenzyme showed that A20 and D4 allow the formation of a "forward sliding clamp" closely associated with the N-terminus of the polymerase, where the template strand enters the enzyme (67, 68) (**Figure 1.2**).

1.2.1.3. Single-stranded DNA binding protein I3

The SSB I3 is a 35-kilodalton protein that is essential to high fidelity replication. Initial identification of I3 showed that the protein is expressed early during replication and displays very strong binding to single-stranded DNA (ssDNA) (37).

Immunofluorescence microscopy (IF) using an antibody that binds to I3 showed I3 localizing to the DNA-filled virus factories (35). I3 colocalizes with DNA stains like Hoechst or 4′,6-diamidino-2-phenylindole (DAPI), although some protein is also freely distributed in the cytoplasm (37). The I3 protein is essential for genome replication, as knocking down the mRNA with RNA interference significantly reduces the accumulation of virus genomic DNA (72). The C-terminus of I3 drives oligomerization, allowing cooperative binding to ssDNA, and attempts to delete the C-terminus failed, suggesting that binding cooperativity is essential for replication (73). Isolation of a VACV lacking full-length I3 required a cell line to complement the I3 protein and confirmed that I3 is essential for genome replication (74).

Understanding the function of I3 in DNA replication requires an understanding of E9-catalyzed homologous recombination (**Figure 1.3**). A recent review provided an in-depth discussion of poxvirus recombination (75). Classically, homologous recombination during double-strand break repair involves proteins binding the ends of the DNA and resecting in a 5′-3′ direction, stabilization of the ssDNA, and strand invasion which generates Holliday junctions and the possibility for crossover (76, 77). Poxviruses employ a recombination mechanism closer to the 2-component systems of λ bacteriophage and herpes simplex virus 1 (75). E9 catalyzes strand transfer reactions *in vitro* that generate higher molecular weight, linear duplexes (78). Adding the I3 protein to this reaction enhances strand transfer. The 3′-5′ exonuclease domain of E9 processes the 3′ end of the substrates, exposing ssDNA (79). I3 stabilizes this 3′ overhang like how Rad51 operates in homology-directed repair in eukaryotic nuclei (77). The combined processing and strand-transfer activities likely evolved to repair broken replication forks (80). A replication fork colliding with a nick in the template strand would prevent further extension of the daughter strand. The strand transfer activity of E9 and I3 ensures that broken replication forks will not be catastrophic to virus replication. This process also permits the rapid generation of recombinant viruses *in vitro* (75). Poxviruses can use recombination to incorporate transfected DNA molecules, provided there is homology between the virus genome and the transgene.

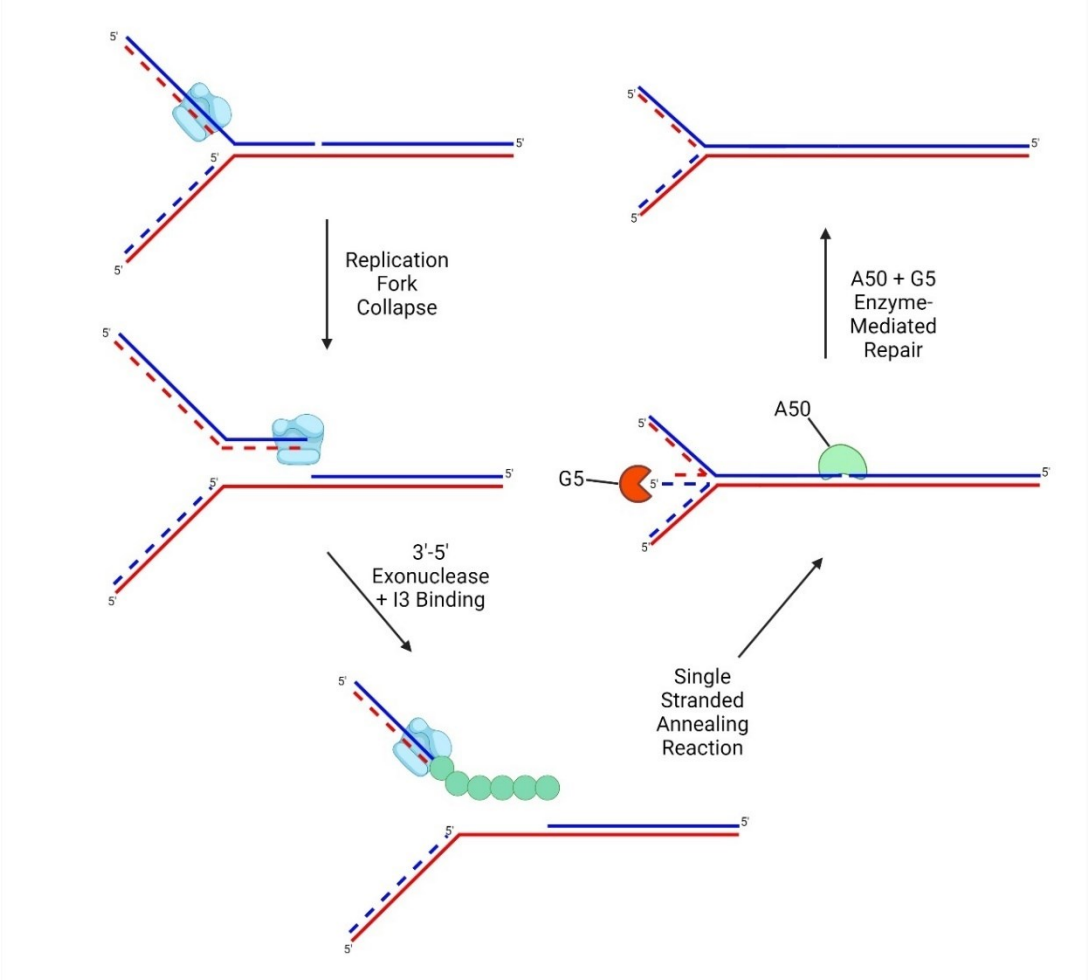

Figure 1.3. Poxvirus homologous recombination. Recombination starts when an extending replication fork collapses. An example shown is if the replication fork encounters a nick in the template strand (solid lines). The polymerase stops synthesis and puts the daughter strand (dashed lines) into the 3′-5′ exonuclease domain. The polymerase resects the daughter strand and I3 stabilizes the exposed ssDNA. E9 and I3 catalyze the strand transfer, resulting in recombinant DNA molecule with an extended flap. The G5 FEN1-like nuclease and A50 DNA ligase repair the joint molecule, resulting in an intact duplex. DNA synthesis can reinitiate from this point. Adapted from (75).

1.2.1.4. FEN1-like nuclease G5

As depicted in **Figure 1.3**, the recombinant junctions generate a “chicken foot” structure with an extended flap. VACV encodes a FEN1-like nuclease in the *G5R* gene that is essential for generating a full-length genome (81). G5 can resolve the recombinant junction and given how recombination is likely essential for DNA repair, the resolution of the recombinant joint is required for efficient genome replication. Viruses that do not

express full-length G5 synthesize fragmented genomes, likely reflecting the collapse and improper repair of replication forks.

1.2.1.5. Primase/Helicase D5

The D5 protein – in addition to its role in uncoating the genome – has an essential function in DNA synthesis. Early studies identified a gene essential for DNA replication that mapped to the HindIII D fragment, and the transcript produced an 82-kilodalton protein (82). An AAA+ domain in the C-terminus of the protein hydrolyzes ATP into ADP and an inorganic phosphate molecule (83). This C-terminal domain confers helicase activity. Conversely, the N-terminus of the protein has a primase domain (84). Interestingly, a yeast two-hybrid screen showed that D5 and D4 interact, further supporting that D5 is associated with replication forks. Temperature sensitive alleles in the *D5R* gene cause rapid loss of DNA synthesis after shifting cultures of virus to a non-permissive temperature, which also suggests that the protein is intimately associated with replication forks. Recent studies generated high-resolution structures of the VACV and MPXV D5 proteins (85, 86). The D5 holoenzyme is a homohexamer with incomplete symmetry because of different conformations reflecting ATP-bound, ADP-bound, or unbound states. Two residues – R585 and F587 – coordinate the movement of the template through the central, basic portal of the hexamer. The coordinated hydrolysis of ATP to ADP allows conformational changes that pull the template through the hexamer. The close interaction between D5 and D4 suggests that D5 and the DNA polymerase holoenzyme could be functioning in concert.

1.2.1.6. DNA Ligase A50

The VACV *A50R* gene encodes a 61-kilodalton protein that possesses ligase activity (87, 88). *In vivo*, viruses lacking A50 are attenuated, suggesting that this protein is essential for virulence (89). However, A50 is non-essential in tissue culture (90, 91). Host DNA ligase I can mask the effects of deleting A50 in tissue culture (92). Thus, A50 may allow the virus to initiate DNA replication prior to recruiting host DNA ligase I. A50 also seems to allow replication in non-proliferating cells, as viruses that do not express A50 replicated to a significantly lower titer than wildtype viruses. Another unusual

feature of the poxvirus DNA ligase is that it recruits cellular topoisomerase II into the virus factories (93). VACV encodes a topoisomerase I for initiating transcription (94). Host topoisomerase II may be the enzyme that decatenates tangled genomic DNA formed during DNA replication. As will be discussed below, the presence of lagging strand DNA synthesis requires a ligase like A50 to repair the phosphodiester backbone (**Figure 1.2**). Additionally, A50 likely also helps repair the backbone after recombination (**Figure 1.3**).

1.2.2. Model of Poxvirus Genome Replication

The most popular model for poxvirus genome replication – the Moyer-Graves model – involves a rolling hairpin for initiation (95). This model involves self-priming from a nick near the termini (96). Because the hairpin sequences are complementary, the holoenzyme complex is thought to loop backwards (33, 95) (**Figure 1.4**).

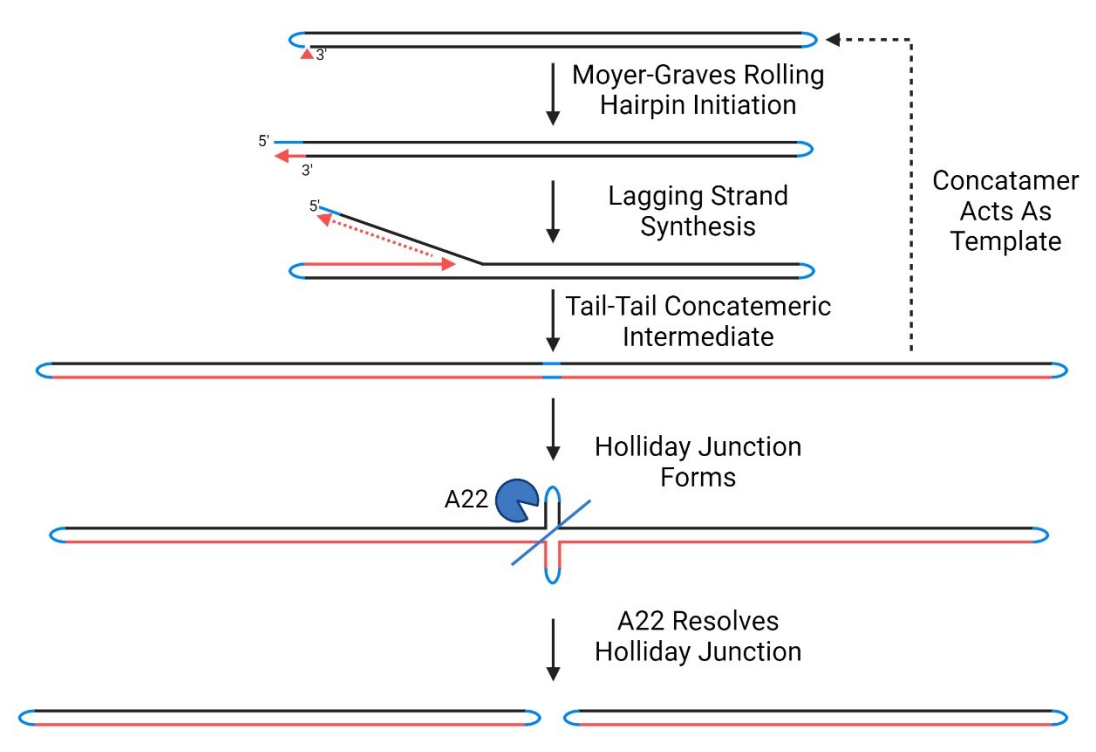

Figure 1.4. Model for poxvirus genome replication. The model is a synthesis of the Moyer-Graves rolling hairpin model and the discovery of lagging strand synthesis (95–98). The rolling hairpin initiates replication from a nick, while lagging strand synthesis (dashed line) occurs from the ssDNA displaced during extension of the leading strand. Either the A22 Holliday junction resolvase resolves the concatemeric intermediate or the concatemer acts as a template for further replication. Replication could initiate from the tail-tail junction and generate bidirectional replication forks.

At the other end of the genome, the same hairpin loop allows the holoenzyme to repeat this process. The result is the generation of high molecular-weight concatemers consisting of genomes linked in a tail-to-tail configuration. The viral enzyme A22 is a homolog of bacterial Holliday junction resolvases that converts the concatemers to single genomes (99, 100). One of the key facets of this model is that the hairpin would function as an origin of replication. However, the holoenzyme complex can replicate transfected plasmids independent of an origin of replication (101). Adding the telomere sequence does enhance replication and generates linear minichromosomes from the plasmids, but the telomeres are not essential for replication (27). This would suggest that the self-priming model is not the only mechanism for initiating DNA replication. Precisely what causes the nick for initiating DNA replication is also unclear. Additionally, the existence of Okazaki fragments near the telomeres and the D5 primase/helicase suggest that there is a lagging strand during DNA replication (84, 98). Without lagging strand synthesis, the rolling hairpin would expose a large amount of ssDNA. Having a lagging strand would naturally stabilize the genome and help replicate the nicked end (**Figure 1.4**). The presence of Okazaki fragments near the telomeres also suggests that DNA replication could initiate from the tail-to-tail junction between the concatemers (98). This would follow the common leading-lagging strand model that Beatriz Pogo initially proposed before Moyer & Graves proposed a rolling hairpin (97). Whether another nick is needed to initiate in this model is unclear. Collectively, the Moyer-Graves rolling hairpin is too simple to explain multiple findings since the initial publication in 1981.

1.3. Genome Replication as a target for antiviral drugs

1.3.1. Cidofovir

Cidofovir (CDV) is a nucleoside analog of deoxycytidine monophosphate (**Figure 1.5A**). The active form of CDV is CDVpp (see Chapter **4.1** for further discussion of CDV metabolism). E9 incorporates CDV into the primer strand across from a deoxyguanosine molecule in the template strand (102). E9 can add one nucleotide after incorporating CDV into the primer strand. However, the rate of extension significantly decreases after the n+1 position, in which "n" refers to the position of CDV in the primer strand. Thus, CDV will be the penultimate nucleotide before synthesis stops. This mechanism is called

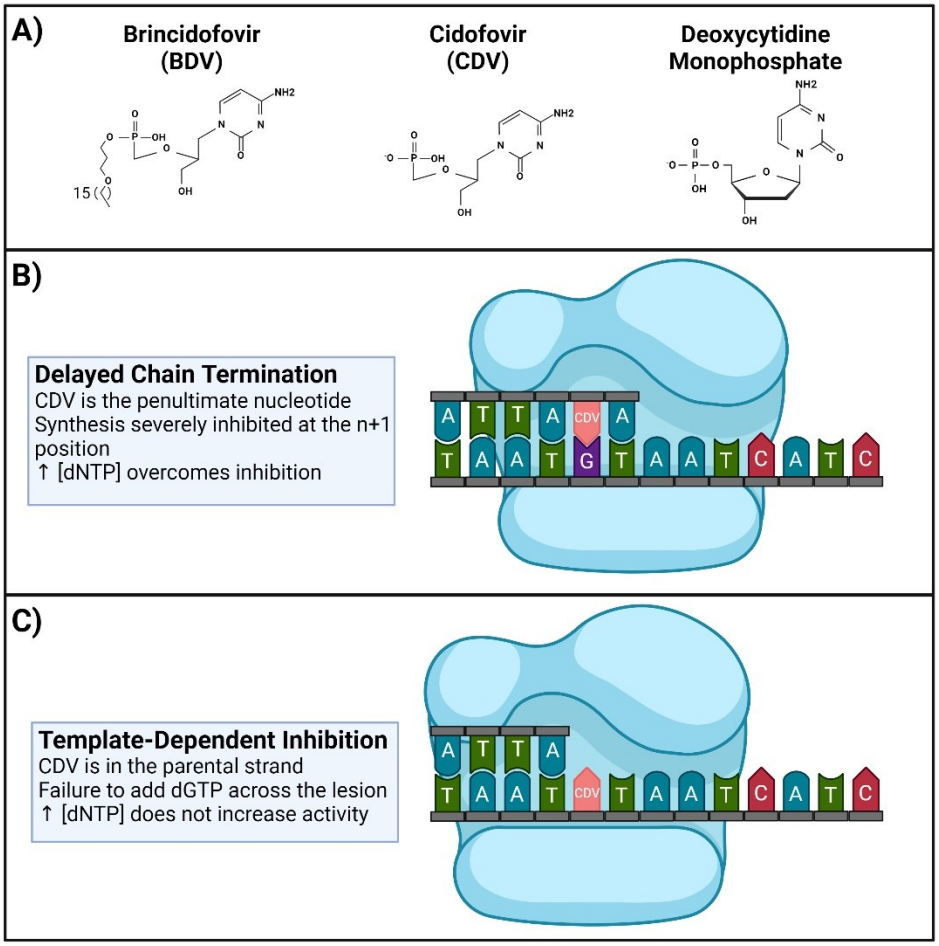

Figure 1.5. CDV and its antiviral mechanisms against E9. A) Chemical structures of CDV, BDV, and dCMP for comparison. BDV is the prodrug of CDV and has an added alkoxy ether modification that masks the negatively-charged phosphonate moiety. CDV lacks the full ribose ring (i.e. the compound is acyclic). The nitrogenous base is identical to cytidine. B) CDV exhibits delayed chain termination with extension stopping at the n+1 position. Increasing the concentration of dNTPs in the reaction can overcome chain termination. C) CDV exhibits a template-dependent effect on E9 that completely stops synthesis at that position. This effect is resistant to increasing nucleotide concentration.

delayed chain termination. The 3′-5′ exonuclease also cannot efficiently remove CDV after incorporation (102). The incorporation of a CDV molecule will therefore trap the polymerase at this position: it is unable to excise CDV and may try extending the daughter strand, only to stop after the n+1 position (**Figure 1.5B**).

One possible result of E9 incorporating CDV is that the molecule may remain in the daughter strands from a single round of synthesis. During subsequent rounds of replication, the polymerase may use a CDV-embedded template (**Figure 1.5C**). *In vitro*

primer extension assays showed that E9 cannot extend a primer strand when CDV is in the template (103). Furthermore, the template-dependent effect on DNA synthesis is more potent than delayed chain termination. Increasing the concentration of nucleotides in the reaction allowed extension after CDV incorporation into the primer strand (102). Conversely, the presence of CDV in the template strand completely prevented primer extension (103). Thus, in addition to stopping DNA synthesis through delayed chain termination, if E9 successfully incorporated CDV during the first round of DNA synthesis, the resulting daughter strands would be poor templates for replication.

1.3.2. Brincidofovir

Despite CDV inhibiting the replication of multiple poxviruses *in vitro* and protecting animals in challenge experiments, there has been limited use in humans for treating poxvirus infections (104). Limited bioavailability is frequently reported because of the negatively-charged phosphonate moiety (**Figure 1.5A**). Many studies reported decreased renal function after administering CDV to patients. These observations motivated efforts to improve the clinical efficacy of CDV. The most successful of these prodrug derivatives is brincidofovir (BDV). An alkoxy ether modification on the phosphonate group masks the negative charge (**Figure 1.5A**). This modification enhanced the bioavailability of the compound (105). Multiple studies found that BDV protects animals from lethal poxvirus challenges (106–109). This ultimately led the Food and Drug Administration to approve BDV for use in humans. However, patients still reported renal toxicity after administration (110). Therefore, there remains a need for a safe and effective poxvirus treatment that targets DNA replication. Additionally, there is concern that drug resistance will arise with widespread use of a monotherapy targeting E9.

1.3.3. Cidofovir resistance maps to the *E9L* gene

The Evans laboratory previously characterized a CDV-resistant (CDV^R) strain of VACV. Serial passage of VACV Lederle strain in increasing concentrations of CDV identified two substitutions in the E9 protein (111). The A314T and A684V substitutions – which comprise the CDV^R *E9L* allele – confer a 10-fold increase in the half maximal

effective concentration (EC_{50}) of CDV. Linkage experiments showed that both substitutions contribute to CDV^R, as viruses bearing either A314T or A684V alone were more sensitive to CDV than a virus with both substitutions. Further studies characterized the effects of these substitutions on E9 activity. The A314T substitution maps to the exonuclease domain of E9 and allows E9 to position the CDV molecule into the active site for excision. Proof of this mechanism came from studies using recombination substrates with CDV embedded at the 3′ end (112). Wildtype, CDV-sensitive (CDV^S) E9 proteins cannot perform strand transfer reactions when CDV is at the 3′ end. Conversely, the CDV^R E9 can perform this reaction, excising the CDV prior to strand transfer. The A684V substitution is less studied, and the precise mechanism underlying resistance is unclear. The 684 position in E9 or the analogous residue in the MPXV polymerase F8 is adjacent to the nucleotide binding site (29, 67, 68). The A684V substitution induces a mutator phenotype and alters the susceptibility of the virus to other compounds when compared to strains bearing the CDV^S *E9L* allele (111, 113, 114). These observations suggest that position 684 has a role in nucleotide selection, and the A684V substitution probably weakens E9 binding to CDVpp prior to incorporation. Fortunately, studies using CDV^R VACV routinely demonstrate that this virus is attenuated in mice. CDV^R viruses are significantly less virulent in immunocompetent mice than CDV^S viruses (111, 113). Interestingly, CDV treatment could still protect mice from weight loss after challenge with the CDV^R virus (111). The mechanism that explains this attenuation is unclear. However, given that there has been limited use of CDV or BDV in humans, it is unclear whether a virulent CDV^R strain could emerge with extensive drug treatment.

1.4. Factors influencing the evolution of CDV^R VACV

The evolution of a CDV^R VACV is a compelling and challenging problem. Because CDV is a monotherapy, CDV^R could arise in circulating populations of poxviruses. However, it is unclear how an exceedingly rare mutant like CDV^R could ever establish itself in a population. Most viruses would not encode a CDV^R allele. Without a strong selective pressure for the trait, CDV^R viruses would likely become too dilute in the population to meaningfully affect drug sensitivity and virulence. This thesis aims to understand how – at a very early stage in the selection – a rare, advantageous mutation

can become dominant in the population. The following sections will discuss molecular factors relevant to the work presented in later chapters.

1.4.1. Poxvirus coinfection

Poxvirus coinfection is a phenomenon relevant to drug resistance. The generation of recombinant poxviruses in circulating populations shows that coinfection can occur *in vivo* (115–118). Coinfection between a CDV^R and a CDV^S strain could impact the selection for CDV^R in the population. It is unclear how a CDV^R and CDV^S strain would interact during a coinfection. One possibility is that the CDV^R virus rescues the replication of the CDV^S strain through complementation. In this case, the CDV^S virus in a coinfected cell would interfere with the selection for the CDV^R virus. Conversely, it is possible that there is a competitive interaction between the CDV^R and CDV^S strains. Selection would operate as if the CDV^S virus replicated in isolation from the CDV^R virus. One would expect that the CDV^R virus would rapidly outcompete the CDV^S virus, leading to a predominantly CDV^R population.

At the molecular level, poxvirus coinfections display several features that could create competition between CDV^R and CDV^S strains. As discussed in Chapter **1.1.2.2.**, poxvirus genomes replicate in cytoplasmic factories that form from the rough ER (40). The Evans laboratory has provided greater detail about the behavior of virus factories in cells coinfected with genetically-distinct VACVs. The λ bacteriophage cro peptide – when fused to a fluorophore like EGFP – directs fluorescent proteins to virus factories, allowing one to visualize virus factories using fluorescence microscopy (119). Host-encoded EGFP-cro allowed for live-cell imaging of virus replication and recombination between coinfecting VACV strains (6, 120). Fluorescence *in situ* hybridization (FISH) allowed for correlating live-cell and fixed images of reporter viruses encoding β-galactosidase (LacZ) or T7 RNA polymerase (T7) (121). The different factory DNAs hybridized to either a LacZ or T7 probe, but not both, showing that virus factories form from a single genome. This functionally segregates each coinfecting virus into a separate replication compartment at an early stage in the lifecycle.

One immediate consequence of segregating coinfecting genomes is that there is a barrier to homologous recombination between two viruses (121). Because coinfecting

viruses replicate in separate factories, recombination between the two strains would require that the factories fuse and that the DNA polymerases catalyzing recombination could access both genomes. In coinfected cells, virus factories often collided, but FISH showed that the genomes remained separated despite the collision (121). The presence of two ER membranes would continue to separate the genomes, preventing recombination until the membrane broke down. Later studies used reporter VACV strains that carry separate fragments of an mCherry-cro construct to determine the timing of recombination between coinfecting viruses (120). One virus carried the intact mCherry-cro gene without a promoter, and the coinfecting virus carried the promoter but a truncated mCherry-cro gene. Expression of mCherry-cro in cells infected with these viruses required homologous recombination to restore the gene with a promoter. Experiments with these viruses showed that mCherry-cro expression coincided with the expression of late proteins, showing that there is a delay between genome replication and inter-virus recombination (120). Further studies followed this observation to determine what cellular structures can interfere with the complete fusion of the virus factories (6). These studies correlated live-cell imaging with transmission EM, showing that ER, mitochondria, and other cellular structures prevented factory fusion. Additionally, the viscosity of the two virosomes delayed mixing past the DNA replication phase (6). Thus, even after factory collision would permit recombination between the two genomes, the gradual loss of DNA polymerase activity and initiation of assembly would prevent a high level of recombination between coinfecting viruses. This would mean that two coinfecting viruses are less likely to yield recombinant progeny.

1.4.2. Complementation

Despite a low level of recombination between coinfecting viruses, there remains the possibility that two viruses could share proteins, resulting in complementation. Complementation describes a general genetic phenomenon in which two mutant organisms generate wildtype progeny during a cross (122). Historically, complementation mapping of ts mutants is the best-described example for VACV (123–127). A ts virus will yield significantly fewer progeny when grown at high temperature (e.g. 39.5^{o}C) compared to low temperature (e.g. 32^{o}C). Researchers used ts strains in crosses at a high

multiplicity of infection (MOI) to determine the location of two mutations (128). If two ts strains yielded a high number of progeny from a coinfection, then the two mutations were in different genes and protein-protein complementation rescued the two viruses (**Figure 1.6A**). Conversely, if two ts strains yield the same number of progeny from a high-temperature coinfection as the two viruses replicating in separate cultures, then the two ts mutations are in the same gene (**Figure 1.6B**).

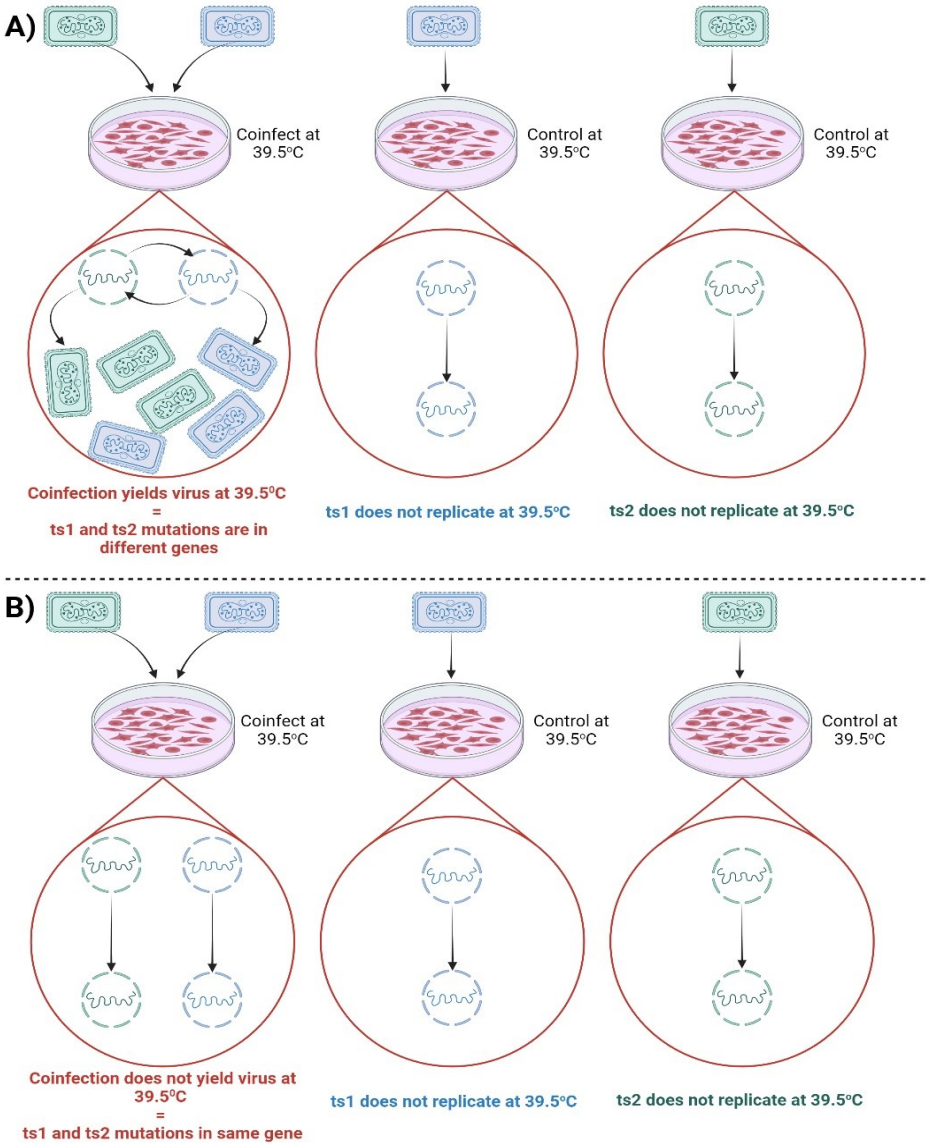

Figure 1.6. Complementation mapping of ts mutations. A) The two ts mutations are in different genes. When the two viruses replicate in separate cultures at high temperature, there are few progeny generated. In coinfected cells, ts1 complements ts2 by providing the functional copy of the protein, and vice versa. The result is that both viruses yield progeny. B) The two ts mutations are in the same gene. The yield will be the same as if ts1 and ts2 replicated in separate cultures.

One critical mechanism underlying the complementation test is that the proteins encoded by two coinfecting viruses must leave the virus factory and act on the other virus. Thus, despite factories isolating the genomes, there must be interaction between coinfecting viruses at the protein level. The consequence for evolution is that coinfection could mask the effects of deleterious mutations. If one coinfecting virus had a mutation in *E9L* and another virus in the cell had a mutation in *D5R*, the immediate effect of those mutations would disappear because of complementation. In the case of drug resistance, a CDV^S virus could survive the selective pressure from CDV treatment if a coinfecting CDV^R virus provided a functional E9 protein, leading to interference with the selection for CDV^R.

1.4.3. Evidence for a barrier to complementation

There is some evidence that complementation is not always possible during a poxvirus coinfection. First, studies from the Moss laboratory examined the localization of viral transcription and protein synthesis in infected cells. This seminal study showed that poxvirus transcription and translation happen in the virus factory (43). Viral mRNA and poly(A) binding protein colocalized in the virus factory. Additionally, components of the eukaryotic initiation factor 4F (eIF4F) complex localized to the virus factory. The authors showed that a virally-encoded LacZ protein stayed inside the virus factory after synthesis. Additionally, the authors used two reporter viruses that encoded a recombinant VACV core protein A5 fused to cyan or yellow fluorescent protein (A5-YFP or A5-CFP). When A5-CFP and A5-YFP coinfected cells, the resulting virus factories were YFP or CFP positive. These experiments suggested that the virus factory might retain some newly synthesized proteins and prevent protein-protein complementation.

Additional evidence for a barrier to complementation came from the Evans laboratory. VACVs expressing mCherry-cro or EGFP-cro from a synthetic early/late promoter allowed for continuous expression of the fluorophore and the ability to track virus factories based on fluorescent protein labelling (120). In coinfected cells, these viruses generated factories with either mCherry or EGFP fluorescence, but not both. Examining two colliding virus factories showed that despite physical contact, the factories retained the mCherrry-cro or EGFP-cro label. This observation suggested that

DNA binding proteins could get retained in the virus factory after synthesis. The use of an early/late promoter is notable because the studies from the Moss laboratory examined intermediate or late gene expression (43, 120). The early transcripts do not localize to the factory like the late transcripts. Studies showed that early during infection, the early transcripts formed aggregates in the cytoplasm that did not colocalize with virus factories (129, 130). Thus, it is unclear what might constrain early proteins to a given virus factory. A more systematic investigation is needed to determine whether there is a barrier to protein-protein complementation at an early stage of the virus lifecycle and how this affects evolution.

1.5. Hypotheses & Goals of the Thesis Project

The objective of this thesis was to understand how coinfection between two VACV strains affects the selection for a rare, advantageous mutant like CDV^R. These studies aimed to determine whether CDV^R viruses have a competitive growth advantage over coinfecting CDV^S viruses, and how the subcellular interaction between CDV^R and CDV^S viruses affects the population. Given the previous findings outlined in Chapter **1.4.3**, I hypothesized that CDV^R and CDV^S coinfections are competitive and a CDV^R virus would not rescue the coinfecting CDV^S strain. I hypothesized that CDV^R viruses would outcompete CDV^S viruses, resulting in the outgrowth of the CDV^R strain in the population. These studies aimed to further our understanding of poxvirus evolution and help address the discrepancies between different studies on the ability of the virus factory to sequester transcripts at an early or late stage of replication (43, 120, 129, 130).

To this end, I generated recombinant viruses expressing cro-EGFP or cro-mKate2 recombinant proteins. Using CDV^R and CDV^S strains, I showed that in single infection models, CDV significantly reduced the replication of the CDV^S strain by inhibiting DNA synthesis, whereas the CDV^R strains displayed higher levels of DNA replication. Surprisingly, coinfection studies showed that cro-EGFP and cro-mKate2 colocalized in virus factories, which contradicted previous findings (120). Additionally, the presence of a CDV^S virus in a coinfection interfered with the selection for CDV^R viruses. I observed this interference at the subcellular level and in plating assays, showing that despite the presence of CDV, a CDV^R virus lost its competitive advantage in coinfected cells.

However, when the two strains replicated in separate cells, there was rapid selection for the CDV^R strain. These studies showed that the exchange of proteins between the virus factories allows CDV^S viruses to parasitize the growth advantage of the CDV^R viruses. Coinfections are therefore unfavourable for maintaining fitness and will prevent the outgrowth of rare, advantageous mutants like drug resistance.

Chapter 2. Materials & Methods

2.1. Cell Culture & Routine Virus Propagation

2.1.1. Cell Culture

The cells used in these studies were African green monkey kidney epithelial cells (BSC-40). Cells were originally purchased from ATCC and maintained in 150mm tissue culture dishes in 1x modified Eagle's medium (Gibco) supplemented with 5% FetalGro or fetal bovine serum (FBS) and 1% each non-essential amino acids, L-glutamine, sodium pyruvate, and antibiotic/antimycotic (1x complete MEM). For routine passage, cell cultures at >90% confluency were washed in sterile 1x phosphate-buffered saline (PBS), then dissociated from the dish using 3mL 0.25% trypsin-EDTA (Gibco) for 5-10 minutes. When all the cells were detached from the dish, new 1x complete MEM was added to neutralize the trypsin (minimum 2 volumes/volume of trypsin). The resulting cell suspension was used to seed new 150mm monolayers of cells. When accurate cell counts were needed - such as for seeding cells for infection or calculating multiplicities of infection (MOI) - after dissociation, 10µL of cell suspension was mixed with 10µL of Trypan Blue and cells were counted using a Countess 3 FL Automated Cell Counter (Invitrogen).

2.1.2. Virus strains

VACV Western Reserve (WR) was used as a "wildtype" strain originally obtained from ATCC and a clonal population was generated through plaque purification by previous members of the Evans laboratory. VACV VDG1.3 is a CDV^R mutant derived from WR (111). The mutations conferring cidofovir resistance were originally identified by serial passage of VACV Lederle strain, and these mutations were then inserted into a nonclonal WR strain by marker rescue.

Table 2.1. Virus strains used in this thesis.

Strain	**Origin**	***E9L* Allele**	***J2R* Locus**
Western Reserve	Originally acquired from ATCC; a plaque-purified clone was previously generated by our lab	Wildtype (A314/A684)	Wildtype
VDG1.3	See (111).	Mutant (A314T/A684V)	Wildtype
pE/L-cro-EGFP	This thesis	Wildtype (A314/A684)	Disrupted *J2R* pE/L-cro-EGFP, gpt cassette
pE/L-cro-mKate2	This thesis	Wildtype (A314/A684)	Disrupted *J2R* pE/L-cro-mKate2, gpt cassette
pE/L-cro-EGFP VDG1.3	This thesis	Mutant (A314T/A684V)	Disrupted *J2R* pE/L-cro-EGFP, gpt cassette
pE/L-cro-mKate2 VDG1.3	This thesis	Mutant (A314T/A684V)	Disrupted *J2R* pE/L-cro-mKate2, gpt cassette

2.1.3. Generation of crude VACV stocks

For crude stocks of virus, BSC-40 cells were seeded in 150mm dishes and infected at low MOI (MOI<0.03). For recombinant viruses expressing the *Escherichia coli* xanthine-guanine phosphoribosyltransferase gene (gpt), viruses were grown with 1x mycophenolic acid selection media (1x MEM with 25µg/mL mycophenolic acid, 250µg/mL xanthine, and 15µg/mL hypoxanthine). Virus replication proceeded for 48-72 hours or until >95% cytopathic effect was observed. The infected monolayer was harvested using a sterile cell scraper and infected cells were pelleted by centrifugation at 2000xg for 10 minutes. The resulting cell pellet was washed in sterile 1x PBS and pelleted at 2000xg for 10 minutes. The cells were resuspended in 10mM Tris-HCl pH 8 and subjected to three freeze/thaw cycles to release infectious virus.

2.1.4. Generation of purified VACV stocks

Purified virus stocks were prepared by infecting large volumes of BSC-40 cells (20-30 150mm dishes) at low MOI following the same infection protocol for generating crude stocks in **2.1.3**. Once >95% cytopathic effect was observed, the monolayers were harvested using a sterile cell scraper, then pelleted by centrifugation at 2000xg for 10 minutes, washed in 1x sterile PBS, then re-pelleted. This pellet was suspended in 10mM Tris-HCl pH 9 with 2mM $MgCl_2$ then transferred to a sterile Dounce homogenizer. The suspension was plunged 20-30 times to lyse the cells using hydrodynamic force. Remaining cells and cellular debris were pelleted at 2000xg for 10 minutes. The supernatant containing virus was taken and the pellet was resuspended in 10mM Tris-HCl pH 9 with 2mM $MgCl_2$ and returned to the Dounce homogenizer for a second lysis step. After pelleting the remaining debris, the two supernatants from lysis were pooled and treated with benzonase (50U/mL) for 30 minutes at 37ºC. Nuclei and unprotected viral DNA were then removed by centrifugation at 2000xg for 10 minutes. The resulting supernatant was then overlaid on 19mL of 36% sucrose in 10mM Tris pH 9 and centrifuged at 26,500xg for 90 minutes in a JS13.1 swinging bucket rotor. The pellet containing purified VACV was resuspended in 10mM Tris pH 8 and stored in aliquots at -80ºC until use.

2.1.5. Titration of VACV in BSC-40 cells

VACV titers were determined by plaque assay using BSC-40 cells. Cells were seeded in 12-well tissue culture plates for confluency the next day. Viruses were serially diluted in serum-free 1x complete MEM. Cells were inoculated with 300µL diluted virus for 1 hour at 37ºC with rocking every 10 minutes to ensure the cell monolayer did not dry out. At 1 hour post-infection, the inoculum was removed and cells were overlaid with 1% medium viscosity carboxymethylcellulose (Sigma, CAS No. 9004-32-4) in 1x complete MEM. Plaque formation proceeded for 48 hours, then wells were fixed with 1 volume of crystal violet stain (1.3% w/v crystal violet, 5% v/v EtOH, 11% v/v formaldehyde, in ddH_2O) for a minimum of 1 hour. Plaques were then counted to calculate the titer in plaque forming units (PFU) per mL.

2.2. Generation of fluorescent reporter viruses

2.2.1. Cloning

Two fluorescent reporter constructs were ordered from Genscript or GeneArt. The constructs consisted of a fluorescent protein fused to a bacteriophage λ cro DNA binding peptide (119). Cro is a protein involved in the lysogeny pathway with a specific recognition sequence; however, cro also binds to DNA non-specifically and has been used in live cell microscopy experiments by our laboratory (119). Enhanced green fluorescent protein (EGFP) and mKate2 were chosen as the fluorophores because of their fast maturation time, similar acid sensitivity, and similar brightness (**Table 3.1**). The cro peptide was fused to the N-terminus of the proteins with a short, flexible linker peptide (Appendix A.2 and A.3). Constructs with C-terminal cro fusions were also generated (Appendix A.4 and A.5). Expression of the fusion protein was controlled by a consensus early/late VACV promoter for continuous expression throughout the viral life cycle.

Both constructs were subcloned into the shuttle vector pTM3 (Appendix A.1). pTM3 encodes sequences homologous to the VACV *J2R* locus. *J2R* encodes a thymidine kinase (TK) that is non-essential in cell culture. The two TK sequences flank a multiple cloning site and the *Escherichia coli* xanthine-guanine phosphoribosyltransferase gene (gpt). The pE/L-cro-FP constructs were directionally cloned into pTM3 using *Sac*I and *Xho*I restriction enzymes and T4 DNA ligase. pTM3-pE/L-cro-EGFP and pTM3-pE/L-cro-mKate2 were each electroporated into OneShot DH10B *E. coli* plated on LB/Amp100 plates. Colonies were screened using colony PCR against the TK region of pTM3. Positive clones were then grown in LB/Amp100 broth for plasmid isolation with the Qiagen Midi Prep Kit (Qiagen). Plasmids were then digested with *Sac*I, *Xho*I, *Xba*I, and *Pvu*I restriction enzymes to confirm successful cloning and subsequently Sanger sequenced (Appendix A.6).

2.2.2. Assembly and purification of recombinant viruses

To generate recombinant viruses expressing the cro-FP constructs, BSC-40 cells were seeded in 60mm dishes and infected with VACV WR or VACV VDG1.3 at an MOI of 0.5. At 1 hour post-infection, the inoculum was replaced with warmed Opti-MEM media (Gibco). Transfection mixes were prepared with 2μg of linearized plasmid and

10μL of Lipofectamine 2000 in a total volume of 1mL Opti-MEM. At 2hpi, the transfection mixes were added dropwise. The infections were allowed to progress for 48 hours before the cell monolayer was harvested and subjected to three freeze/thaw cycles to release virions into the supernatant, creating a crude stock of recombinant virus.

The resulting recombinant viruses would express the cro-FP construct and the *E. coli* gpt cassette, allowing for selection of fluorescent plaques and metabolic selection with mycophenolic acid (MPA). Thus, to obtain purified stocks of each virus, the supernatants from the crude stocks were used to inoculate BSC-40 cells in 1x liquid mycophenolic acid (MPA) selection media (see **2.1.3** for media composition). After 48 hours, the monolayer was harvested, subjected to three freeze/thaw cycles, and the supernatant was used for a second round of liquid selection. After two rounds of liquid selection, the supernatant was used to inoculate BSC-40 cells, and at 1hpi, the cell monolayer was overlaid with 1x MPA media containing 0.85% noble agar. At 72hpi, fluorescent plaques were picked and used as the inoculum for another round of selection. Each fluorescent virus was repeatedly plaque picked (>5 rounds) to generate pure populations. After the final round of plaque purification, each supernatant was used to inoculate two wells of a 6-well plate: one for assessing the purity and another to create a passage 0 seed stock.

2.2.3. Genetic analysis of recombinant viruses

To assess the purity of the plaque purified viruses, the infection was allowed to progress until >90% of the cells were infected based on cytopathic effect. At this time, the cells were harvested and lysed with lysis buffer for genomic DNA extraction overnight at 37°C (0.2mg/mL proteinase K, 1.2% sodium dodecyl sulfate, 50mM Tris-HCl pH 8, 4mM EDTA pH 8, 4mM $CaCl_2$). DNA was purified from the lysate using phenol/chloroform extraction and ethanol precipitation. Purified DNA was then used as the template DNA for a polymerase chain reaction (PCR) with primers against the *J2R* locus. Amplicons were resolved on 0.8% agarose in 1x Tris-buffered acetate with EDTA.

Virus stocks that appeared homogeneous by PCR were then used to generate larger stocks of virus by infecting BSC-40 cells at an MOI of 0.01 in 1x MPA selection media. After 2-3 days – or when the monolayer reached greater than 90% cytopathic

effect – the cells were harvested and lysed by Dounce homogenization. Each resulting supernatant was treated with benzonase, then centrifuged through a 36% sucrose cushion and resuspended in 10mM Tris-HCl pH 8. High-titer virus stocks were then aliquoted, freeze/thawed once, sonicated, and titrated on BSC-40 cells.

2.3. Characterization of fluorescent reporter viruses

2.3.1. Determination of virus replication kinetics

The replicative fitness of each fluorescent virus was assessed by comparing the plaque size and by comparing replication rates in low-MOI growth curves. For the plaque size measurements, BSC-40 cells were seeded in 60mm dishes and infected with 50 PFU of each recombinant virus and overlaid with 1x MEM containing 1% CMC. At 48hpi, the monolayer was stained with crystal violet. Each plate was then imaged, and the plaque size was measured in Fiji (131). The data were plotted in and analyzed in GraphPad Prism (see **2.7**).

For low-MOI growth curves, BSC-40 cells were seeded in 6-well plates and infected at an MOI of 0.01. At 1hpi, 1mL of warmed 1x MEM was added to each well. The cells were harvested at 0, 3, 6, 12, 24, and 48hpi. Virions were released by repeated freeze/thaw cycles and titrated on BSC-40 cells in triplicate. The data were plotted and analyzed in GraphPad Prism (see **2.7**).

2.3.2. Determination of the EC_{50} for cidofovir by plaque reduction assay

To assess the drug sensitivity of the recombinant viruses, a plaque reduction assay was used. BSC-40 cells were seeded into 12-well plates and each plate infected with 50 PFU of recombinant viruses. At 1hpi, the inoculum was replaced with 1x MEM with 1% CMC and increasing concentrations of cidofovir. At 48hpi, the plates were stained with crystal violet and plaques were counted. The plaque count at each concentration was normalized to untreated wells to calculate the plating efficiency. The data were then fitted to a nonlinear regression curve in GraphPad Prism (see **2.7**) to determine the half maximal effective concentration (EC_{50}).

Table 2.2. Primers and plasmids used in this thesis.

Primers		
Primer Name	**Sequence (5′-3′)**	**Tm in 50mM NaCl (°C) (Based on Integrated DNA Technologies Custom Oligo Tool[1])**
TK Forward	TATTCAGTTGATAATCGGCCCCATGTTT	58.5
TK Reverse	GAGTCGATGTAACACTTTCTACACACCG	58.7
pTM3-Fluor-Seq-Fwd	AACAAGGGGCTGAAGGATGC	58.1
pTM3-Fluor-Seq-Rev-2	GCAGCCAACTCAGCTTCCTTTC	58.8
Plasmids		
Plasmid Name	**Origin**	**Uses**
pTM3	Dr. Bernard Moss	Shuttle vector encoding homology to VACV *J2R*
pMK-RQ pE/L-cro-EGFP	GeneArt/This thesis	Encodes chemically synthesized pE/L-cro-EGFP construct
pUC57 pE/L-cro-mKate2	GenScript/This thesis	Encodes chemically synthesized pE/L-cro-mKate2 construct
pTM3 pE/L-cro-EGFP	This thesis	Generation of recombinant viruses expressing cro-EGFP
pTM3 pE/L-cro-mKate2	This thesis	Generation of recombinant viruses expressing cro-mKate2

[1] Link: https://www.idtdna.com/pages/products/custom-dna-rna/dna-oligos/custom-dna-oligos

2.3.4. Live-cell and correlative microscopy

The localization of the cro-FP proteins was assessed by live cell microscopy. BSC-40 cells were seeded on 35mm glass-bottom dishes and placed on ice for 15 minutes prior to inoculation with virus at an MOI of 5 to stop endocytosis, synchronizing virus entry into the cells. Virus binding proceeded for 1 hour at 4ºC. The inoculum was then replaced with 2mL of warmed FluoroBrite^{TM} DMEM supplemented with 2% FBS and 10mM HEPES buffer. The cells were replaced to a 37ºC CO_2 incubator for 1 hour. At 1hpi, the cells were mounted in a heated chamber with 5% CO_2 atmosphere and imaged using an Olympus IX-81 spinning disk confocal microscope with a 60X/1.5-numerical aperture oil objective. For live-cell imaging, a 40µm z-stack with 1µm z-step was used to ensure the cells would stay in focus throughout the time course. EGFP was detected using a 491nm excitation laser and a 515/30nm FITC filter. mKate2 was detected using a 561nm excitation laser and a 650/100nm RFP filter. Exposure conditions were optimized based on the fluorescent protein signal at 4-6hpi. Images were collected every 10 minutes for 11 hours to follow a complete infection. For image processing, the z-stacks were compressed, and the maximum display intensity was adjusted for optimal visualization of the fluorophores during early stages of factory development (3-8hpi). Timestamps and scale bars were added in Fiji (131).

To confirm that the cro-FP proteins labelled viral factories, a correlative approach was taken that combined live-cell microscopy with immunofluorescence. In these experiments, BSC-40 cells were seeded on 35mm dishes engraved with an alpha-numerical grid. The cells were synchronized on ice for 15 minutes and infected at an MOI of 5. Virus binding proceeded for 1 hour at 4ºC before the inoculum was replaced with 2mL of warmed FluoroBrite^{TM} DMEM supplemented with 2% FBS and 10mM HEPES buffer. At 5hpi, the dish was mounted in a heated chamber with 5% CO_2 atmosphere and imaged using an Olympus IX-81 spinning disk confocal microscope with a 60X/1.5-numerical aperture oil objective. A z-stack was taken to image the entire cell with a 0.3µm z-step. EGFP was detected using a 491nm excitation laser and a 515/30nm FITC filter. mKate2 was detected using a 561nm excitation laser and a 650/100nm RFP filter.

After imaging the live fluorophore, the cells were fixed in 2% paraformaldehyde (PFA) for 10 minutes at room temperature. Free aldehydes were quenched with 0.1M glycine in 1x phosphate-buffered saline (PBS) for 20 minutes. The cells were washed three times with 1x PBS before permeabilization with 0.2% TritonX-100 in 1x PBS for 2 minutes. The cells were washed again then blocked in 3% w/v bovine serum albumin in 1x PBS overnight at 4^{o}C. Viral factories were stained with mouse anti-I3 monoclonal antibody (1:500) in 3% BSA for 2 hours at room temperature. Excess primary antibody was removed by washing in 1x PBS with 0.1% Tween-20 (1x PBS-T) three times, then the cells were stained with donkey anti-mouse secondary antibodies conjugated to AlexaFluor 488 (1:2000) and 100µg/mL DAPI in 3% BSA for 1 hour at room temperature. The cells were washed in 1x PBS-T three times. Stained cells were then imaged by confocal microscopy as above. For DAPI, a 405nm excitation laser and 460/50nm DAPI filter were used. Images were then pseudocolored in Fiji (131).

2.4. Studies investigating the effect of cidofovir on factory growth

2.4.1. Microscopy

All experiments described in this section used a Quorum Technologies WaveFX spinning disk confocal microscope attached to an Olympus IX-81 camera. All images were acquired with a 60X/1.5-numerical aperture oil objective. All experiments also used the same excitation lasers and filters. For DAPI, a 405nm excitation laser and 460/50nm filter were used. For EGFP or AlexaFluor 488, a 491nm excitation laser and 515/30nm emission filter were used. For mKate2, a 561nm excitation laser and 650/100nm emission filter were used. For AlexaFluor 647, a 642nm excitation laser and 700/75nm emission filter were used.

For live-cell imaging experiments, the excitation parameters were kept consistent for every independent experiment (**Table 2.4**). 40µm Z-stacks were acquired with 1µm sections to ensure rapid imaging. For fixed-cell imaging experiments, the excitation parameters were changed based on the strength of signal which varied between independent experiments. Z-stacks were acquired with 0.3µm sections and the size of each stack varied per point.

Table 2.3. Reagents used in immunofluorescence experiments.

Antibodies			
Antigen	**Isotype**	**Source**	**Dilution**
αVACV I3 (10D11)	Mouse IgG	Purified from a lab-made hybridoma by Nicole Favis in June, 2022	1:500
αMouse IgG-Alexa Fluor 488	Donkey IgG	ThermoFisher (Catalog # A-21202)	1:2000
Nucleotide-based Probes			
Molecule	**Use**	**Source**	**Dilution**
5′-Ethnyl-2'-deoxyuridine (EdU)	Metabolic labeling of nascent DNA synthesis	Acquired from a Click-iT™ EdU Alexa Fluor™ 594 Imaging Kit (ThermoFisher Catalog # C10339)	10μM final concentration
5-(3-aminoallyl)-dUTP	Fluorescence *in situ* hybridization (FISH)	ARES® 647 Labeling Kit (Molecular Probes)	0.06mM final concentration
Fluorescent Dyes			
Molecule	**Use**	**Source**	**Dilution**
4′,6-diamidino-2-Phenylindole (DAPI)	DNA Counterstain	ThermoFisher (Catalog # D1306)	1:100 (10μg/mL)
AlexaFluor(R) 647 Azide	Labeling EdU	ThermoFisher (Catalog # A10277)	4.8μM final concentration
AlexaFluor(R) 647 NHS	Labeling FISH probes	ARES® 647 Labeling Kit (Molecular Probes)	Kit does not specify, used as directed in manual

Table 2.4. Settings used for all live imaging experiments.

Filter	**FITC (EGFP)**	**RFP (mKate2)**
Exposure Time	0.1s	0.1s
Gain	3	3
Sensitivity (photomultiplier effect)	220	150
Transmission (% of laser strength used)	50	50

2.4.2. Live-cell imaging of factory growth in the presence of cidofovir

BSC-40 cells were seeded on 35mm glass-bottom dishes. For experiments involving pretreatment, CDV was diluted in the culture media to 330μM. The cells were incubated overnight and synchronized on ice for 15 minutes, then infected at an MOI of 5. Virus binding proceeded for 1 hour at 4ºC on a rocker before the inoculum was replaced with 2mL warmed FluoroBrite™ media with 2% FBS and 10mM HEPES buffer. The cells were returned to a 37ºC CO_2 incubator for 3 hours before mounting in a heated chamber with 5% CO_2 atmosphere and imaged as described above. Images were collected every 10 minutes from 3-6hpi.

2.4.3. Measurement of virus factory volume by immunofluorescence microscopy

BSC-40 cells were seeded on 18mm glass coverslips with or without 330μM CDV diluted in the media. The cells were incubated overnight and synchronized on ice for 15 minutes, then infected at an MOI of 3 to reduce the likelihood of factory collisions (121). Virus binding proceeded for 1 hour at 4ºC on a rocker before the inoculum was replaced with 2mL warmed complete MEM with 5% FetalGro or FBS. At 6 hours post-infection, the cells were fixed in 2% PFA at room temperature for 10 minutes followed by quenching with 0.1M glycine in 1x PBS pH 7.4. Cells were permeabilized in 0.2% TritonX-100 for 2 minutes then washed three times with 1x PBS pH 7.4 and blocked for

1 hour in 3% BSA. Viral factories were stained with mouse anti-I3 monoclonal antibody (1:500) in 3% BSA for 2 hours at room temperature. Excess primary antibody was removed by washing in 1x PBS with 0.1% Tween-20 (1x PBS-T) three times, then the cells were stained with donkey anti-mouse secondary antibodies conjugated to AlexaFluor 488 (1:2000) and 100µg/mL DAPI in 3% BSA for 1 hour at room temperature. Cells were washed with 1x PBS-T twice, then once with 1x PBS. Coverslips were mounted in SlowFade Gold Antifade Mountant (Invitrogen) and sealed with nail polish, then stored at 4ºC until imaging.

2.4.4. Assessment of E9 activity by immunofluorescence using EdU pulse labeling

For EdU pulse labeling experiments, the same protocol was followed for other IF experiments except that at 5 hours post-infection, the media was changed to complete MEM with 10µM EdU. Cells were pulsed for 30 minutes, then fixed in 2% PFA at room temperature for 10 minutes followed by quenching with 0.1M glycine in 1x PBS pH 7.4. Cells were permeabilized in 0.2% TritonX-100 for 2 minutes then washed three times with 1x PBS pH 7.4. For click chemistry, the reaction was assembled in the order shown in **Table 2.5**. After assembling the reaction mixture, 500µL was added to each coverslip and labeling proceeded in the dark for 30 minutes. After click chemistry, the reaction mixture was discarded, and the samples were processed as in **2.4.3**.

Table 2.5. Reaction components for click labeling of EdU (Adapted from Kieser *et al.* (119)).

Component	Volume (µL)	Final Concentration
0.1M Tris-HCl pH 9.0	430	86mM
0.1M $CuSO_4$	20	4mM
AlexaFluor™ 647 Azide (2mM in DMSO)	1.2	4.8µM
0.1M $NaC_6H_7O_6$	50	10mM

2.5. Coinfection studies of CDV-sensitive and CDV-resistant vaccinia viruses

2.5.1. Live imaging of coinfected cells

The live imaging was performed as described in **2.4.2** except that the cells were coinfected with VACV pE/L-cro-EGFP VDG1.3 (CDV^R) and VACV pE/L-cro-mKate2 (CDV^S) at a combined MOI of 5. The ratio of mutant to wildtype was 1:1 or changed to 1:5.

2.5.2. Generation of fluorescent probes for *in situ* hybridization

To make probes for *in situ* hybridization experiments, the plasmid pMK-RQ-pE/L-cro-EGFP was used as a template for nick translation. A modified nucleotide 5-(3-aminoallyl)-dUTP was incorporated into the fragments to allow labeling the terminal amino moiety with an AlexaFluor™ succinimidyl ester; these reagents were provided by the ARES® 647 Labeling Kit (Molecular Probes). The nick translation reaction is shown in **Table 2.6**. Reactions were assembled as a master mix before aliquoting into 250µL PCR tubes and adding the enzymes. The reaction was conducted at 16ºC for 2 hours before the samples were purified using the QIAquick® PCR Purification Kit (QIAGEN). A small volume was loaded onto a 1% agarose gel to confirm that the reaction successfully generated smaller DNA fragments, which would run as a smear in an agarose gel.

To generate the fluorescent probe, 1-5µg of DNA was used in the labeling protocol provided by the kit. The reaction was assembled as in **Table 2.7**. Labeling proceeded for 1 hour at room temperature in the dark before purifying the DNA using the QIAquick® PCR Purification Kit (QIAGEN). The resulting fluorescent DNA was quantified using a NanoDrop spectrophotometer before storage at -20ºC until use.

Table 2.6. Reaction conditions for nick translation of DNA

Reaction Component	Volume	Final Concentration
Nuclease-Free Water	21.5µL	N/A
10X Nick Translation Buffer (0.5M Tris-HCl, 50mM $MgCl_2$, 0.5mg/mL nuclease-free BSA, pH 7.8)	5µL	1x
0.1M DTT	5µL	10mM
d(GAC)TP Mix (0.5mM each dATP, dCTP, dGTP)	4µL	40µM each
0.5mM dTTP	1µL	10µM
0.5mM 5-(3-aminoallyl)-dUTP	6µL	60µM
1µg/µL Template DNA	1µL	0.02µg/µL
DNase I Stock (1mg/mL in 20mM Tris-HCl, 50mM NaCl, 1mM DTT, 100µg/mL nuclease-free BSA, 50% v/v glycerol, pH 7.6); I used DNaseI from StemCell Technologies which has the same activity (2000 Kunitz units/mg)	5µL	0.1mg/mL
DNA Polymerase I, 10U/µL	1.5µL	0.3U/µL

Table 2.7. Labeling terminal amines with AlexaFluor™ NHS-Esters

Reaction Component	Volume	Final Concentration
Nick translated DNA	5µL	1-5µg/reaction
1M $NaC_2H_4O_2$	3µL	0.1M
AlexaFluor™ 647 NHS Ester (Reconstituted in DMSO directly before the reaction)	2µL	Kit does not specify

2.5.3. Fluorescence *in situ* hybridization to vaccinia virus DNA

For FISH experiments, BSC-40 cells were seeded on 18mm glass coverslips. The cells were treated with 330µM CDV overnight, then synchronized on ice for 15 minutes before coinfection with VACV pE/L-cro-EGFP (CDV^S) and VACV VDG1.3 (CDV^R) at a 1:1 ratio with a combined MOI of 5. The virus was allowed to bind to the cells for 1 hour before the inoculum was removed, the cells washed with 1x PBS pH 7.4, and warmed complete MEM was added to the wells. The cells were returned to a 37ºC CO_2 incubator, and the infection allowed to progress for 6 hours before fixation in cold 4% PFA. The cells were fixed overnight at 4ºC, then the free aldehydes were quenched with 0.1M glycine in 1x PBS pH 7.4.

For FISH staining, the cells were permeabilized with 0.2% TritonX-100 in 1x PBS pH 7.4 for 2 minutes at room temperature. The detergent was washed away, then the cells were treated with 100µg/mL RNase A (ThermoFisher) in 2x saline sodium citrate (SSC) pH 7 for 1 hour at 37ºC. The enzyme was washed away with 1x PBS-T three times for five minutes each. The cells were then blocked in 3% BSA for 1 hour at room temperature. After blocking, the sample was prehybridized to the anti-cro-EGFP probe (**Table 2.8**). The coverslip was transferred to a $25mm^2$ SecureSeal™ Hybridization Chamber and loaded with 100µL of hybridization buffer. This was accomplished by mounting the coverslip cells up on a microscopy slide, then placing the hybridization chamber over and loading the buffer into the chamber through the ports on the sides of the chamber. The prehybridization step was done at 70ºC and then the sample was snap cooled in an ice water bath. The probe was hybridized to the target at 50ºC overnight. The

samples were then washed with 50% formamide in 2x SSC pH 7 twice for 30 minutes at 37ºC, then washed in 2x SSC pH 7 for 5 minutes. The citrate buffer was washed away with PBS, then viral factories were processed using the same protocol as in **2.4.3** for immunofluorescence targeting the I3 protein.

Table 2.8. Composition of FISH buffer for detecting viral genomes.

Reaction Component	**Volume (µL)**	**Final Concentration**
Formamide, UltraPure	50	50% v/v
50% v/v dextran sulfate	10	5% v/v
20x saline sodium citrate pH 7	10	0.2x
1M sodium phosphate buffer pH 7	5	50mM
0.5M EDTA	2	1mM
1mg/mL salmon sperm DNA	2	0.01mg/mL
50x Denhardt's Reagent	2	1x
Alexa Fluor™ 647-conjugated probe	Varies	2ng/µL
ddH_2O	Up to final volume (100µL)	N/A

2.5.4. Population-level analysis of vaccinia virus coinfections

To assess the relative growth advantage of CDV^R versus CDV^S strains, under different selection pressures and in co-infected cells, BSC-40 cells were seeded in 6-well plates with or without 330µM CDV. The cells were synchronized for 15 minutes before synchronous coinfection with VACV pE/L-cro-EGFP VDG1.3 (CDV^R) and/or VACV pE/L-cro-mKate2 (CDV^S) at a combined MOI of 10 with a CDV^R-to-CDV^S ratio of 1:1 or combined MOI of 11 with a ratio of 1:10 CDV^R-to-CDV^S viruses. Alternatively, the MOI was reduced to 0.02 with a 1:1 CDV^R-to-CDV^S ratio. Additional quantities of each virus mixture were prepared and set aside to later confirm the "Input" sample ratios. The

viruses were allowed to bind to cells for 1 hour at 4ºC before the inoculum was removed, the cells washed with 1× PBS pH 7.4, and 2mL of warmed complete MEM without CDV. The plates were returned to a 37ºC CO_2 incubator for 16-24 hours. The monolayers were harvested, freeze/thawed to release any progeny, and these then titered on new BSC-40 cells in 12-well plates without CDV.

To count fluorescent plaques, BSC-40 cells were seeded in 6-well plates. The "Input" and "Output" samples were diluted in serum-free media to plate ~100 plaques/well. Each "Input" and "Output" sample was plated in experimental triplicate. The cells were inoculated with virus for 1 hour at 37ºC before the inoculum was removed and the cells were overlaid with 1× MEM with 1% CMC without CDV. The plates were returned to a 37ºC CO_2 incubator for 48 hours. Plaques formed from the progeny in the absence of CDV reflected the frequency of CDV^R and CDV^S viruses in the population after the initial coinfection when the selective pressure from CDV was present. Plating the progeny in the presence of CDV would not permit CDV^S plaques to form, and thus the CDV^S virus would not be represented in the final analysis. Each plate was then imaged using a BioTek Cytation 5 (Agilent) microscope using a 1.25× objective and the GFP and TRITC channels to detect the EGFP and mKate2 fluorescence, respectively.

An auto-exposure feature was used to identify optimal exposure settings, and then each well was imaged completely using a montage of tiles. Each tile had a 20% overlap with adjacent tiles to permit computational reconstruction of the full montage. The Gen5 software (Agilent) was used to stitch the tiles together and preprocessing was applied to generate a final image for each well. The images were opened in Fiji (131). The "cell counter" plugin was used to count EGFP-positive and mKate2-positive plaques. EGFP-positive plaques were assumed to be CDV^R while mKate2-positive plaques were assumed to be CDV^S.

2.6. Analysis of confocal microscopy data

2.6.1. Quantification of live-cell imaging data

For live-cell imaging, z-stacks were flattened into a single plane and saved as a tagged image file (TIF) stack. Images were then opened in Fiji (131). The lookup table (LUT) was inverted to set the background as white and signal as black. The maximum

signal intensity was adjusted for optimal display of EGFP or mKate2 fluorescence at early time points when the fluorescence is weakest. The image scale was set to match the scale of the acquisition software, which is based on the objective lens used (512 pixels/76.41μm or 6.70 pixels/μm). A time stamp was added to each image indicating the time post-infection. Lastly, a scale bar was added to each image within the stack. The stack was then saved as an AVI file or an image sequence for stills. Quantification was achieved by using the ROI tool to outline single factories within the cell at each time point. The data were extracted and compiled into GraphPad Prism (see **2.7**). The factory measurements were plotted as a function of time and analyzed using non-linear regression. The data were assumed to be exponential for the purposes of choosing the type of curve. The software generated exponential growth curves, which were then used for further analysis. The doubling time and goodness of fit (R^2) were extracted and analyzed in GraphPad Prism (see **2.7**).

2.6.2. Quantification of factory volume

Volocity v6.3 (Perkin Elmer) was used for analyzing all the immunofluorescence data. To find the volume of individual factories, the "Compartmentalize" protocol was adapted (**Figure 2.1**). First, the software was instructed to identify containers using the Confocal FITC channel (I3 staining). A size limitation was added to this step to discard any containers larger than 200μm^3. This exclusion discarded nuclei to simplify the analysis. After identifying containers, the software was instructed to identify objects using the Confocal DAPI channel (DNA) within the I3-positive containers. This protocol therefore identifies objects that are $I3^+/DAPI^+$, which are viral factories. All identification steps were based on fluorescence intensity with automatic thresholding. This protocol was applied in a batch analysis, then the data were combed to ensure the software accurately identified objects. The most common errors were multiple factories being identified as a single object; these measurements were discarded. The volume measurements were then compiled analyzed in GraphPad Prism (see **2.7**).

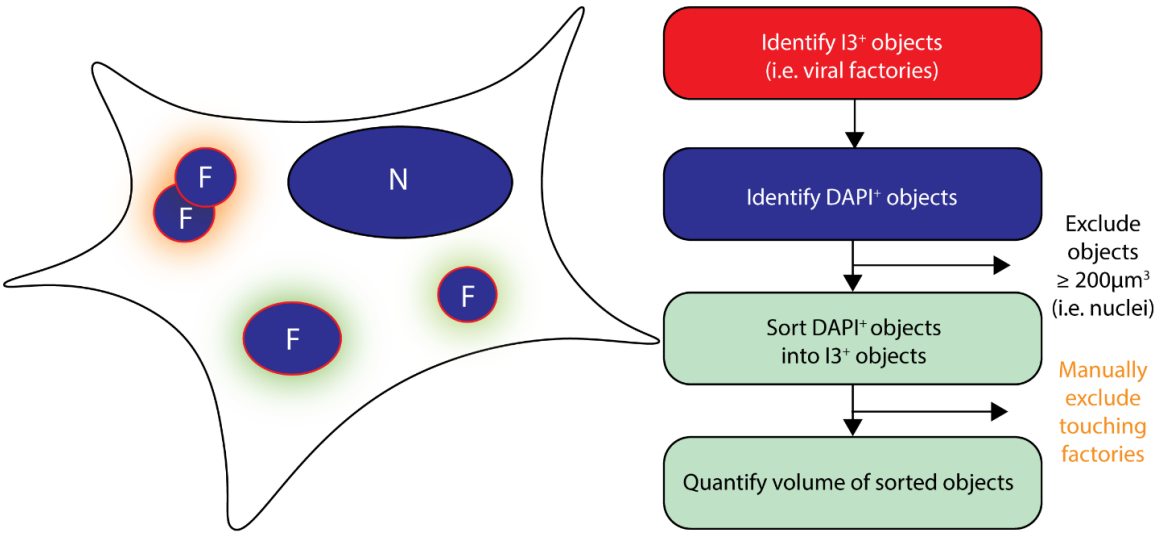

Figure 2.1. Workflow for quantifying viral factory volume in 2.6.2.

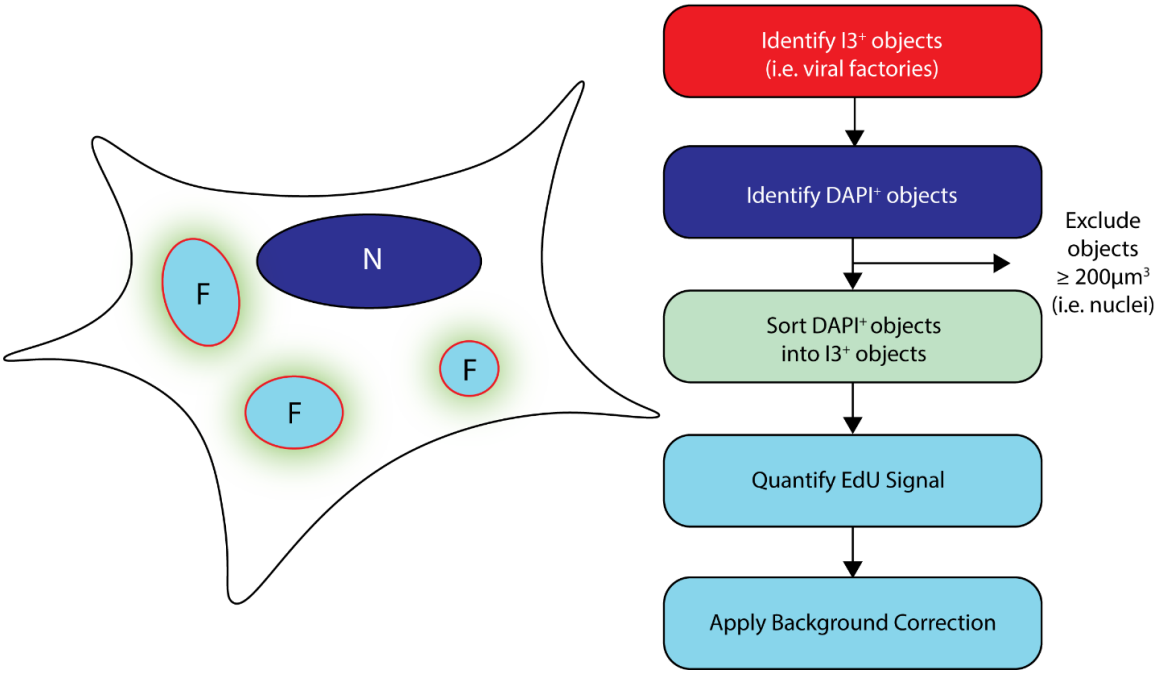

Figure 2.2. Workflow for quantifying EdU fluorescence intensity in 2.6.3.

2.6.3. Quantification of EdU signal intensity

For quantifying mean EdU fluorescence intensity, the volume quantification protocol was adopted to identify objects using the Confocal Cy5 channel (EdU) within $I3^+$ containers (**Figure 2.2**). The protocol was applied in batch analysis, then the data were combed to ensure the software accurately identified objects. Common errors were objects within the nucleus that were sites of cellular DNA synthesis. A background

correction was also applied by subtracting the black limit of each image from the mean fluorescence intensity. The corrected intensity values were then compiled and analyzed in GraphPad Prism (see **2.7**).

2.6.4. Quantification of FISH data

All FISH images were quantified the same as in **2.6.1**. Concentrated probe signal inside an $I3^+/DAPI^+$ factory was used to differentiate the wildtype viruses expressing cro-EGFP from the mutant viruses that lacked any target sequence. The DAPI staining was used to measure the surface area of the 2D projections, and the surface area measurements were compiled and analyzed in GraphPad Prism (see **2.7**).

2.7. Statistical Analysis

All statistical analyses were performed in GraphPad Prism version 9.3.1. To compare two groups of data with a single variable, an unpaired two-way t-test was used. To compare multiple groups of data with a single variable, one-way analysis of variation (ANOVA) was performed with multiple comparisons. To compare multiple groups of data with multiple variables, two-way ANOVA was performed with multiple comparisons. The post-hoc test for multiple comparisons was chosen based on the recommendation from GraphPad Prism, and the specific test is indicated in the figure's caption. The threshold for significance was $p<0.05$. Significance was represented in figures as follows: * $p<0.05$, ** $p<0.01$, **** $p<0.001$. All statistical analyses were done using data collected from three independent biological replicates except for the FISH experiments, which were repeated twice. For imaging experiments, the data were pooled to represent a large population of factories which were collected over multiple experiments. These larger distributions capture the natural variation across a population which would be lost if each factory were treated as a technical replicate within a given experiment. A minimum of 30 factories were included in the analysis for reliable statistics. The only exception to this is in **Figure 4.**. Two factories were removed from the "CDV^S Treated" group because Prism generated growth curves with negative values for the doubling time.

Chapter 3. Generation and phenotypic characterization of recombinant viruses

3.1. Introduction

Light microscopy is a common method for studying viral replication sites in infected cells. Fluorescence imaging can easily detect poxvirus factories in fixed or live samples (119). Live-cell imaging of poxvirus infection is an established method in the Evans laboratory that allows tracking virus factories throughout the lifecycle of the virus. These methods rely on the expression of a fusion protein consisting of a fluorophore tagged with the cro peptide from λ bacteriophage (6, 120, 121). Cro is a sequence-specific repressor that regulates lysogeny (132); however, the peptide also binds DNA non-specifically and can direct a fluorophore to double-stranded DNA (119). This technique previously allowed for studying the kinetics of homologous recombination; however, expressing mCherry-cro had a clear fitness cost to the virus (120). Therefore, I designed new viruses to express a cro-fluorophore (cro-FP) construct to label viral DNA. The data presented in this chapter pertain to the design of these recombinant viruses and phenotypic characterization.

3.2. Results

3.2.1. Design and construction of recombinant vaccinia viruses expressing fluorescent proteins

To study VACV factory formation and growth, I designed two constructs to label viral DNA with enhanced green fluorescent protein (EGFP) or monomeric Kate2 (mKate2). EGFP is a derivative of *Aequorea victoria* GFP, while mKate2 is a derivative of *Entacmaea quadricolor* fluorescent protein (133). The spectral characteristics are listed in **Table 3.1**. The two well-distinguished spectra and similar maturation times make EGFP and mKate2 a good combination for a dual reporter system. To direct the fluorescent proteins to DNA, I added the cro peptide at the N- or C-terminals of the genes with a flexible linker peptide to ensure proper folding of the protein. Controlling gene expression was a synthetic early/late promoter, allowing continuous expression throughout the viral lifecycle. I directionally cloned each construct into the shuttle vector

pTM3 using *XhoI* and *SacI* restriction enzymes (APPEN). pTM3 contains sequences homologous to VACV *J2R*, which encodes a thymidine kinase that is non-essential in tissue culture (134). I transfected linearized plasmids into cells infected with VACV WR or VDG1.3 and then plaque purified the recombinant viruses. This failed for viruses expressing C-terminal-tagged EGFP-cro and mKate2-cro genes, as I could not eliminate non-fluorescent plaques despite multiple rounds of plaque purification. The N-terminal cro fusion proteins were more stable and I could plaque purify clones of recombinant virus which were subsequently expanded in culture to produce working stocks. I also extracted virus genomic DNA from sucrose-purified preparations of virus particles for next-generation sequencing. The genomic maps of the four recombinant viruses are shown in **Figure 3.1**.

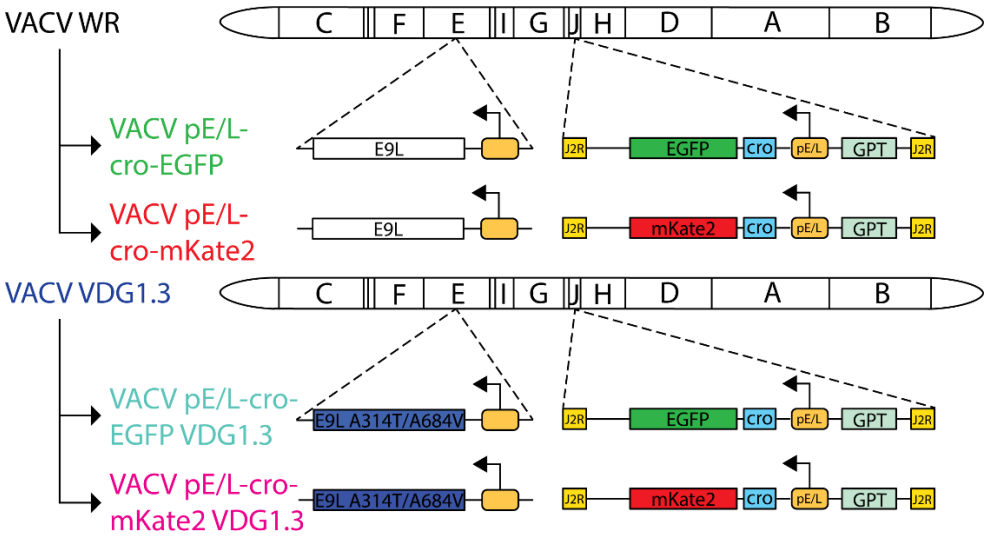

Figure 3.1. Recombinant viruses expressing cro-EGFP and cro-mKate2 reporters.

Table 3.1. Spectral properties of EGFP and mKate2. Adapted from FPbase (135).

Property	**Enhanced green fluorescent protein (EGFP)**	**Monomeric Kate2 (mKate2)**
Excitation Wavelength (nm)	488	588
Emission Wavelength (nm)	507	633
Brightness	33.54	25.0
pKa	6.0	5.4
Maturation (min)	25.0	20.0
Lifetime (ns)	2.6	2.5

3.2.2. cro-EGFP and cro-mKate2 do not affect viral fitness

The studies described in this thesis required that any recombinant viruses exhibited comparable fitness properties. Differences in DNA replication rates would likely affect virus factory growth and make direct comparisons between different mutants challenging. Disrupting *J2R* has no impact on fitness in tissue culture (134), but a toxic transgene could impact replication. This was previously seen with a virus expressing mCherry-cro (120). Therefore, I conducted experiments to determine if expressing cro-EGFP and/or cro-mKate2 affected viral fitness. An initial clue came from examining the plaques produced on BSC-40 cells. I measured plaque size at 48 hours post-infection and found that there was no significant difference in plaque size between viruses expressing cro-EGFP versus cro-mKate2 (**Figure 3.2**). Importantly, there was also no change in plaque size compared to the parental WR and VDG1.3 strains, indicating that expressing cro-EGFP or cro-mKate2 has no impact on fitness. In addition to measuring plaque size, I conducted multi-step growth curves with the recombinant viruses and the parental strains (**Figure 3.3**). The data showed that the titers of all six viruses tested increased after the initial round of replication (24 hours post-infection), and the second round of replication further increased the titer. Analysis using the end titers of all six viruses showed that there was no significant difference between the six tested viruses (**Figure 3.4**). These experiments confirmed that expression of cro-EGFP or cro-mKate2 did not significantly affect the fitness of the recombinant viruses.

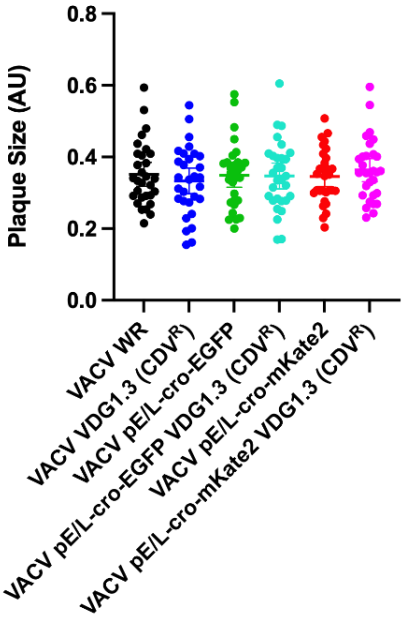

Figure 3.2. The presence of cro-EGFP or cro-mKate2 does not affect plaque size. Plaque sizes were measured from using digital images of fixed and stained virus-infected monolayers. The images were scaled to the size of the well to scale the measurement across multiple infections. AU = Arbitrary Units. Data were compiled in GraphPad Prism and analyzed using a one-way ANOVA with Dunnett's multiple comparisons. Date are plotted as the mean with the 95% confidence interval.

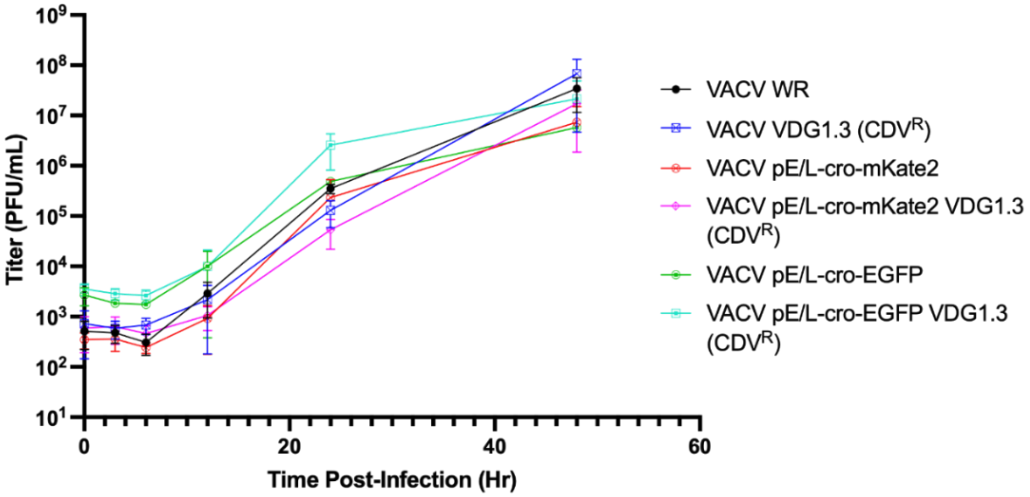

Figure 3.3. Neither cro-EGFP nor cro-mKate2 affect virus replication kinetics. Cells were infected at an MOI of 0.01 and harvested at the indicated timepoints. Infectious viruses were released by repeated freeze/thaw cycles and titrated on BSC-40 cells in experimental triplicate. Data are plotted as mean ± standard deviation from three independent biological experiments.

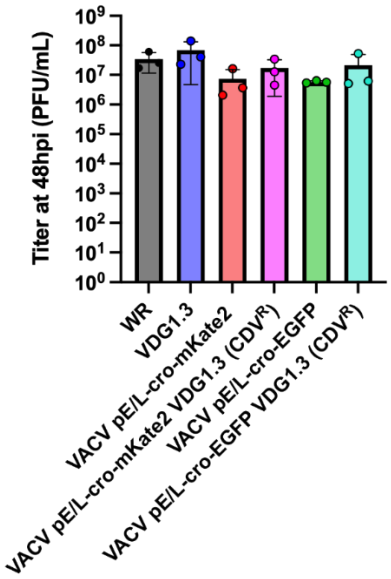

Figure 3.4. Infections with all six viruses tested yield the same amount of progeny. The final titers from the growth curves using the indicated viruses were compiled and analyzed in GraphPad Prism using a one-way ANOVA with Tukey's multiple comparisons. Data are plotted as mean ± standard deviation from three independent biological experiments.

3.2.3. Viruses derived from VDG1.3 are resistant to cidofovir

The studies described in Chapters 4 and 5 required that I determined a range of drug concentrations where the concentration of CDV was high enough to inhibit replication of viruses encoding the wildtype *E9L* gene but did not greatly inhibit viruses encoding the mutant VDG1.3 CDV^R allele. To do this, I determined the half maximal effective concentration (EC_{50}) of CDV for the six viruses described in **3.2.2.** I used a plaque reduction assay where the viruses were plated in media containing increasing concentrations of CDV. **Figure 3.5.** shows the inhibition curves and the nonlinear regressions fitted to three independent biological replicates. The range of concentrations delineated well-defined top, middle, and bottom sections of the curves with R^2 values above 0.9, indicating a good curve fit. The EC_{50} values are compiled in **Table 3.2.** Two-way ANOVA identified a significant increase in EC_{50} values for the VDG1.3 viruses compared to those encoding the wildtype *E9L* allele, indicating that these are truly drug-resistant viruses. The data also suggested that encoding cro-EGFP and cro-mKate2 makes viruses more sensitive to CDV, as there was a nearly 2-fold decrease in EC_{50} between VDG1.3 and the recombinants encoding the same *E9L* mutations.

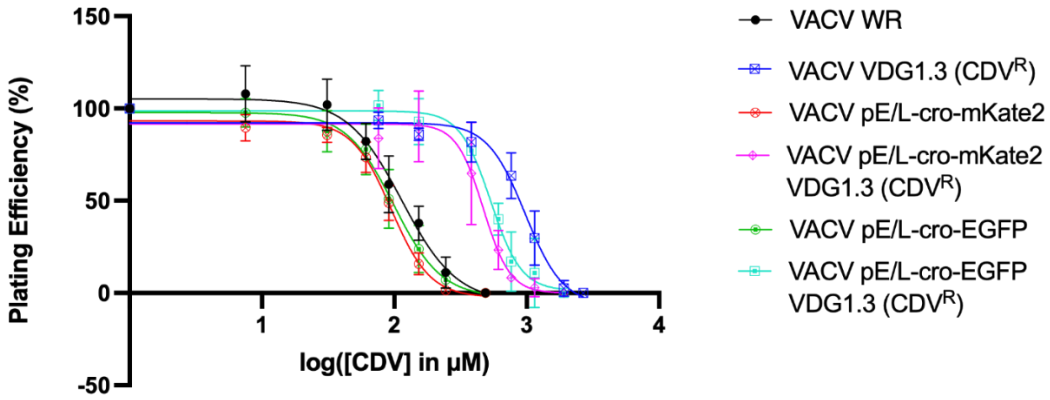

Figure 3.5. VDG1.3 encodes CDV resistance. Viruses were plated in increasing concentrations of CDV and the plaques were later counted at 48 hours post-infection. Each count was normalized to the number of plaques in the untreated wells to calculate plating efficiency. Data were analyzed using non-linear regression in GraphPad Prism to calculate the EC_{50} and to generate best fit curves. Data are plotted as the mean ± standard deviation from three independent biological experiments.

Table 3.2. Drug resistance properties of recombinant viruses.

VACV	EC_{50} (μM); 95% C.I.	Fold change from WR	p-value* (vs. WR)
Western Reserve	114; 90-158	N/A	N/A
pE/L-cro-mKate2	96; 85-106	0.839	0.043
pE/L-cro-EGFP	100; 82-125	0.879	0.32
VDG1.3	973; 837-1476	8.22	<0.001
pE/L-cro-mKate2 VDG1.3	470; 384-561	4.12	0.011
pE/L-cro-EGFP VDG1.3	533; 461-616	4.68	<0.001

* p-values were calculated from a two-way ANOVA with Dunnett's multiple comparisons.

3.2.4. Fluorescent tags label virus factories

Finally, I wanted to determine whether the cro peptide would direct EGFP and/or mKate2 to virus factories. The NGS data showed that cro was present and fused to the same ORF encoding the fluorophore. To confirm the recombinant proteins were expressed and functional, I used live-cell imaging to track the expression of cro-EGFP and cro-mKate2 in infected cells. I initially started imaging the infected cells at 1 hour post-infection (hpi) and followed each infection for 11 hours. This broad window would encompass all stages of virus development and would provide a basis for planning future live-cell imaging with a focus on the DNA replication stage. **Figure 3.6** shows still

images extracted from the experiments. By 4 hours post-infection, well-distinguished EGFP and mKate2 structures formed in the cytoplasm and continued to develop. Rapid expansion of the structures followed until growth stopped around 8 hours post-infection. By this time, these structures became more diffuse and frequently collided with others in the cytoplasm. This led to the formation of large aggregates of protein that appeared late (8-12 hpi).

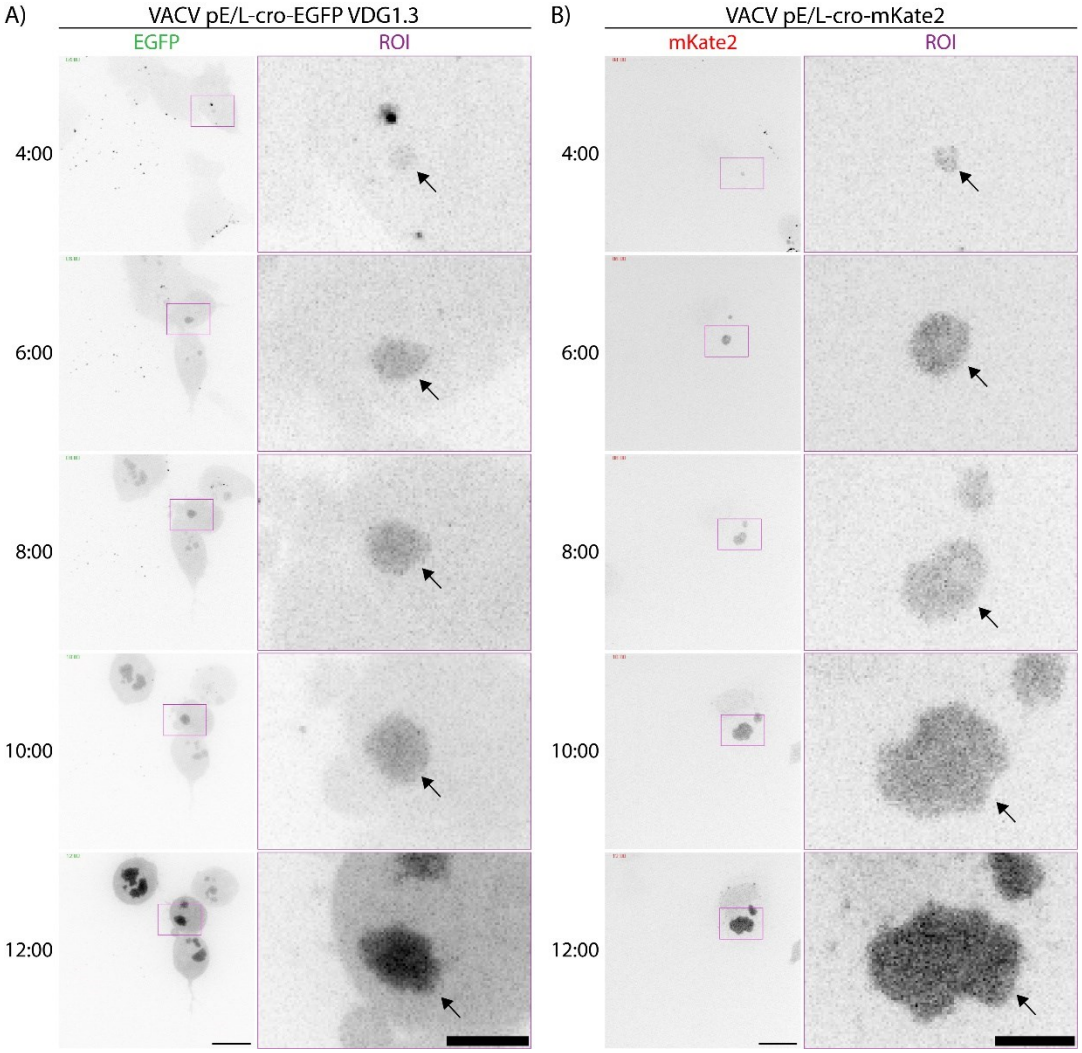

Figure 3.6. cro-EGFP and cro-mKate2 label structures with the same characteristics as virus factories. Cells were seeded on 35mm FluoroDish glass-bottom dishes and synchronously infected with the VACV pE/L-cro-EGFP VDG1.3 (A) or pE/L-cro-mKate2 (B) at an MOI of 5. At 1hpi, the dish was mounted on a spinning disc confocal microscope at 60x magnification. A 37ºC chamber with 5% CO_2 was used to maintain live cells. A z-stack with 1µm sections was captured every 10 minutes for 11 hours. EGFP- and mKate2-positive objects are indicated with arrows. Images were processed for display in Fiji. The scale bar = 15µm. The region of interest (ROI) scale bar = 5µm.

The timing of these events was consistent with what was previously described for virus factories (120). As will be shown in greater detail in Chapter 4, the earliest one can detect virus factories is about 3-4 hours post-infection. However, these experiments lacked a positive control that was needed to confirm that cro-EGFP and cro-mKate2 labeled virus factories. Initially, I tried to use EGFP fluorescence to image cro-EGFP while also immunostaining for the VACV single-stranded binding protein I3 and staining DNA with DAPI in fixed cells. I3 and DAPI are commonly used as markers of virus factories. However, as **Figure 3.7** and **3.8** show, at early timepoints when single virus factories are detected, EGFP and mKate2 fluorescence was not detected.

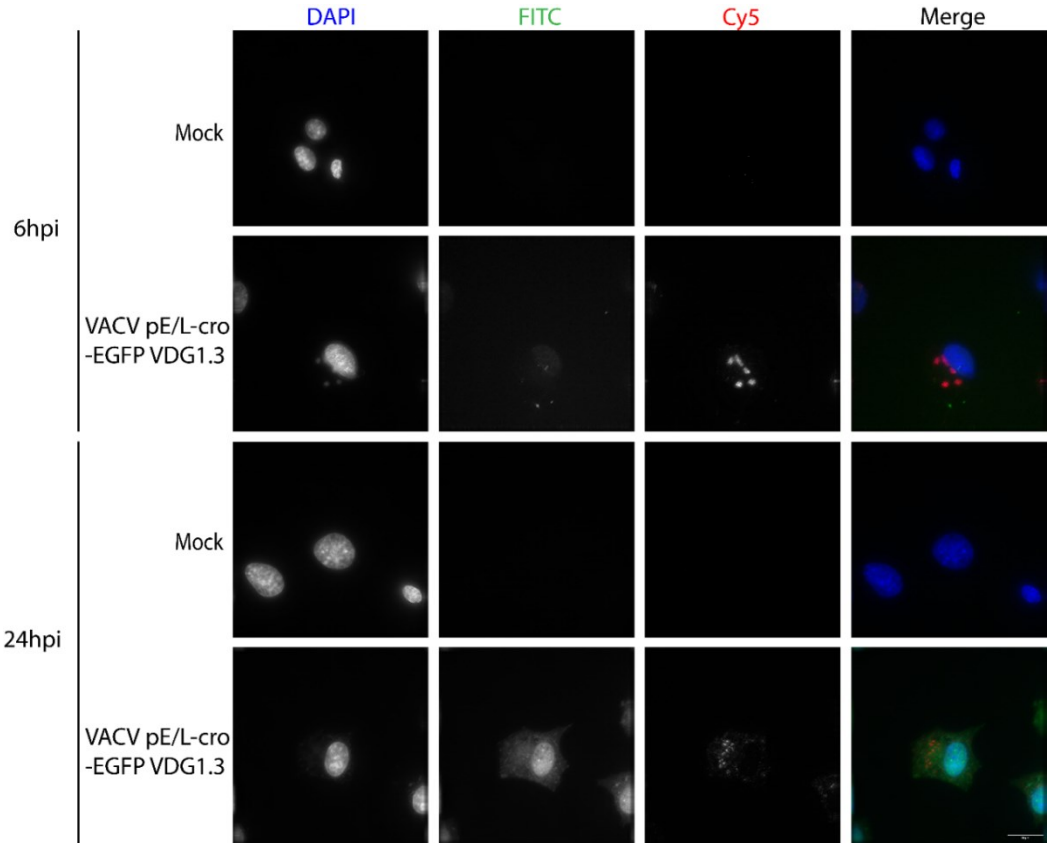

Figure 3.7. EGFP fluorescence is undetectable in fixed samples at early timepoints. Cells were seeded on coverslips and synchronously infected with VACV pE/L-cro-EGFP VDG1.3 at an MOI of 5. The cells were harvested at the indicated times and fixed in 4% PFA for 30 minutes on ice. The cells were then immunostained with an antibody targeting the I3 protein with DAPI counterstaining for DNA. Coverslips were imaged using a DeltaVision deconvolution microscope at 60X magnification. The FITC filter set was used to capture fluorescence from EGFP. The Cy5 filter set was used to capture the fluorescence from the Alexa Fluor 647-conjugated secondary antibody against the I3 antibody. The scale bar in the bottom right panel = 20μm.

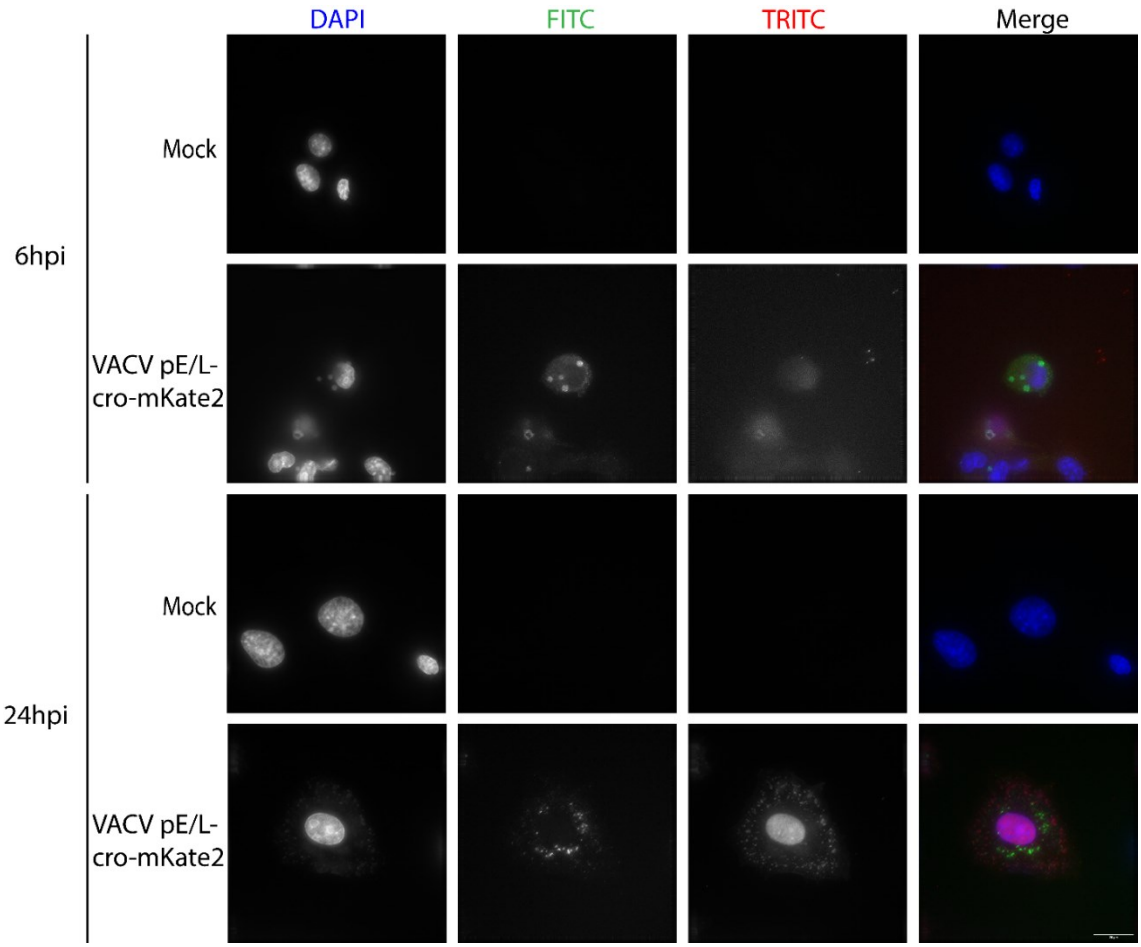

Figure 3.8. mKate2 fluorescence is undetectable in fixed samples at early timepoints. Cells were seeded on coverslips and synchronously infected with VACV pE/L-cro-mKate2 at an MOI of 5. The cells were harvested at the indicated times and fixed in 4% PFA for 30 minutes on ice. The cells were then immunostained with an antibody targeting the I3 protein with DAPI counterstaining for DNA. Coverslips were imaged using a DeltaVision deconvolution microscope at 60X magnification. The TRITC filter set was used to capture fluorescence from mKate2. The FITC filter set was used to capture the fluorescence from the AlexaFluor 488-conjugated secondary antibody against the I3 antibody. The scale bar in the bottom right panel = 20μm.

To overcome this problem, I used a correlative microscopy approach. I used 35mm dishes marked with an alpha-numeric grid. The grid allowed reliable identification of cells pre- and post-fixation (121). I imaged the fluorescent proteins in infected cells at 6hpi, then fixed the cells in 2% PFA and conducted immunostaining for I3 and DNA staining with DAPI (**Figure 3.9**). The cro-EGFP and cro-mKate2 proteins colocalized with I3 and cytoplasmic DNA (DAPI), indicating that the fluorescent proteins labelled virus factories. The simplest explanation for why I could not detect EGFP and mKate2 post-fixation was that at the early timepoint, there was little fluorescent protein present in the cell. Figures **3.7** and **3.8** showed strong EGFP and mKate2 fluorescence at 24hpi, when there was ample fluorescent protein for detection. Conversely, early on there would not be as much protein, so any destruction of the fluorophore by fixation would have a greater effect on detection.

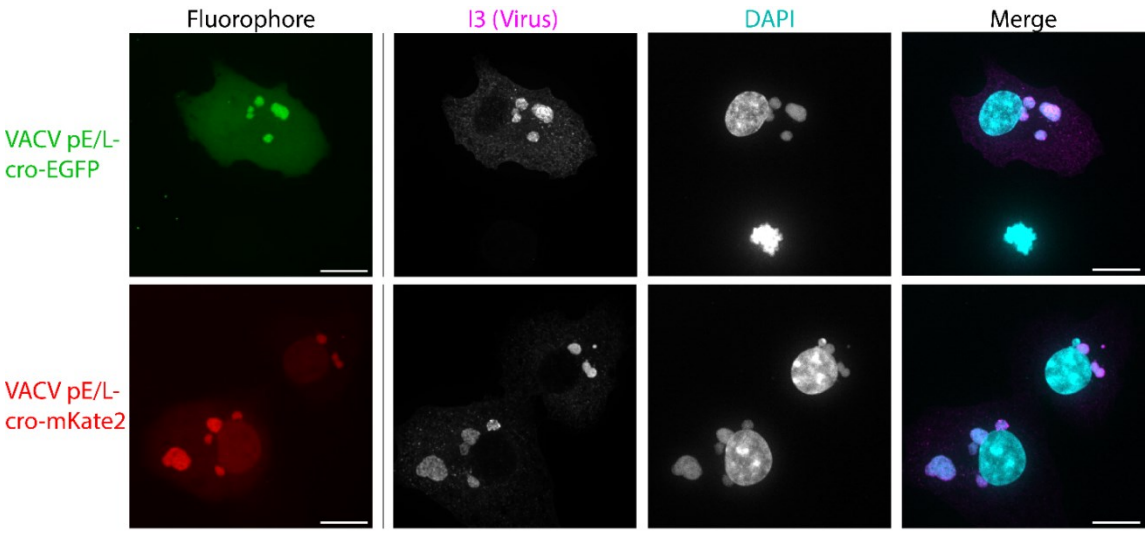

Figure 3.9. cro-EGFP and cro-mKate2 colocalize with the VACV protein I3 and DAPI-stained cytoplasmic DNA. Cells were seeded in 35mm dishes with 500µm^2 grid and synchronously infected with the indicated viruses at an MOI of 5. At 6 hours post-infection, the dishes were mounted on a spinning disc confocal microscope at 60x magnification to capture EGFP and mKate2 fluorescence (Fluorophore panels), then fixed in 2% PFA for 10 minutes at room temperature. Samples were then stained with a monoclonal antibody to detect the I3 protein and with DAPI to detect DNA. Cells were imaged again and pseudocolored in Fiji. The scale bar = 15µm.

3.3. Conclusions

Recombinant viruses expressing cro-EGFP and cro-mKate2 were successfully recovered. The presence of these recombinant proteins had no effect on virus replication, as shown in **Figures 3.2-3.4.** There was no change in plaque size or kinetics of replication in multi-step growth curves. The VDG1.3 allele (E9 A314T/A684V) conferred resistance to CDV relative to the wildtype allele. **Figure 3.5** shows that CDV^R mutations in *E9L* conferred a nearly 10-fold increase in EC_{50} compared to WR, but the concomitant disruption of *J2R* in the fluorescent viruses likely somewhat sensitized these viruses to drug treatment relative to the resistance exhibited by VDG1.3 (which is TK^+). This phenomenon will be further discussed in Chapter **6**. The live-cell imaging in **Figure 3.6** showed factories expanding and increasing in signal intensity over time, eventually stopping growth and becoming very diffuse. Several studies have shown that virus factories form near the rough ER, and these surrounding membranes persist late into infection (6, 40, 120). The membranes surrounding the virus factory gradually break down as late proteins begin forming viral crescents, which are the progenitors of the immature virion membrane (136). The diffuse structures seen at later timepoints (>8hpi) likely form as the ER fragments and immature virions form. This process also involves encapsidation of single viral genomes, which can further contribute to the diffuse staining seen as the DNA starts to spread out within assembled virions.

The images acquired using correlative microscopy, seen in **Figure 3.9**, showed that cro-EGFP and cro-mKate2 colocalized with the single-stranded DNA binding protein I3 and with DAPI-stained cytoplasmic DNA, confirming the recombinant proteins can label virus factories. PFA fixation quenched EGFP and mKate2 fluorescence at early timepoints, but apparently not at very late timepoints (**Figures 3.7** and **3.8**). This likely reflected the fact that EGFP and mKate2 were much more abundant late in infection, which would make the proteins easier to detect despite some decrease in fluorescence from fixation. Interestingly, close examination of VACV pE/L-cro-mKate2 infection at 24hpi showed mKate2 fluorescence in DAPI-positive puncta distributed at the edges of the cell (**Figure 3.8**). Previous observations suggested that cro-FP proteins could package into mature virions (119, 120). That mKate2 and DAPI colocalized in discrete puncta further suggests packaging of fluorescent proteins into the DNA-containing virions. This

cannot be a definitive conclusion because I did not use probes to detect the structural proteins of the virions.

Overall, the data presented in Chapter 3 provided the necessary foundation for a study of the antiviral effects of CDV on factory formation and growth. In particular, the measurements of EC_{50} identified a range of concentrations in which CDV inhibits the wildtype (CDV^S) viruses but minimally affects the replication of CDV^R mutants. Additionally, the capacity to track the expansion of virus factories using live-cell imaging permits further optical investigation of singly and coinfected cells with or without drug treatment.

Chapter 4. The effect of cidofovir on vaccinia virus factory development

4.1. Introduction

There are conflicting data on the mechanism of action for CDV in living cells. A study conducted by Jesus *et al*. involved infecting BSC-40 cells with VACV while simultaneous initiating treatment with CDV. These authors then collected viral DNA later in infection and quantified genome copy number using Southern blots (137). These studies detected no effects on DNA replication until very late timepoints (over 12 hours post-infection). The authors also examined concatemer resolution and found no defects. These data led the authors to suggest that CDV does not have any effect on DNA replication, but instead affects the packaging and maturation of virions. Atomic force microscopy showed substantial fracturing of genomic DNA after CDV treatment, which the authors proposed could prevent proper packaging into immature virions.

The problem inherent with these experiments is that cells slowly absorb and metabolize CDV. **Figure 4.1** shows the steps required for conversion of CDV into CDVpp, the bioactive form. The negatively-charged phosphonate moiety slows membrane transit, greatly reducing CDV uptake into cells (138). Once in the cytoplasm, cellular kinases must perform two phosphorylation reactions. Pyrimidine nucleoside monophosphate kinase converts CDV to CDVp (139). Pyruvate kinase, creatine kinase, or nucleoside diphosphate kinase can convert CDVp to CDVpp. The phosphonate bond of CDV creates an irregular structure compared to dCMP, disrupting metabolite binding to the active sites of the cellular kinases (139). This slows the rate of conversion, particularly the conversion of CDVp to CDVpp. Given the slow kinetics of CDV uptake and conversion to CDVpp, treating cells concomitant with infection would not be expected to show any effect on DNA synthesis because CDVpp would not be present in the cell. Moreover, these authors' conclusions completely contradict the observations that CDV^R maps to *E9L* and that CDV inhibits E9 in primer extension assays (102, 103, 114). These concerns motivated me to undertake mechanistic studies of CDV using my reporter viruses and relying on microscopy to reveal any changes in factory size or growth rate.

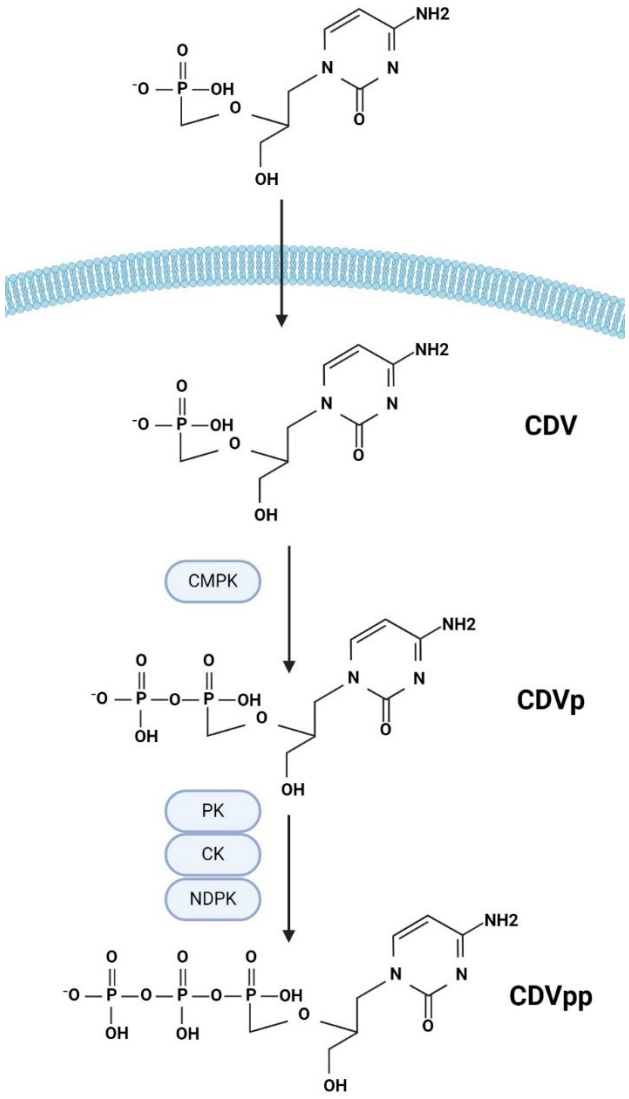

Figure 4.1. Steps required to convert cidofovir to cidofovir diphosphate. CDV crosses the plasma membrane through passive diffusion before being phosphorylated. Pyrimidine nucleoside monophosphate kinase (CMPK) converts CDV to CDVp. Pyruvate kinase (PK), creatine kinase (CK), or nucleoside diphosphate kinase (NDPK) convert CDVp to CDVpp.

4.2. Results

4.2.1. Live-cell imaging shows that CDV inhibits virus factory growth

The approach I chose to study CDV antiviral activity employed live-cell imaging and the recombinant viruses described in Chapter **3**. These experiments were conducted using 330μM CDV which is the EC_{90} concentration for wildtype viruses, or the

concentration that reduced the plating efficiency by 90%. I reasoned that EC_{90} would maximize any antiviral effects from CDV treatment, making it much easier to detect any changes in factory growth. The general approach used for all live-cell imaging is shown in **Figure 4.2A** and detailed protocols are found in chapters **2.4.1** and **2.4.2**. Most importantly, overnight pretreatment of the cells with CDV allowed ample time for drug uptake and CDVpp conversion prior to infection. I chose to image from 3-6hpi because this is the timeframe when E9 is most abundant (140). This timeframe also coincides with the peak DNA replication phase (6). Any antiviral activity against E9 should occur within this timeframe.

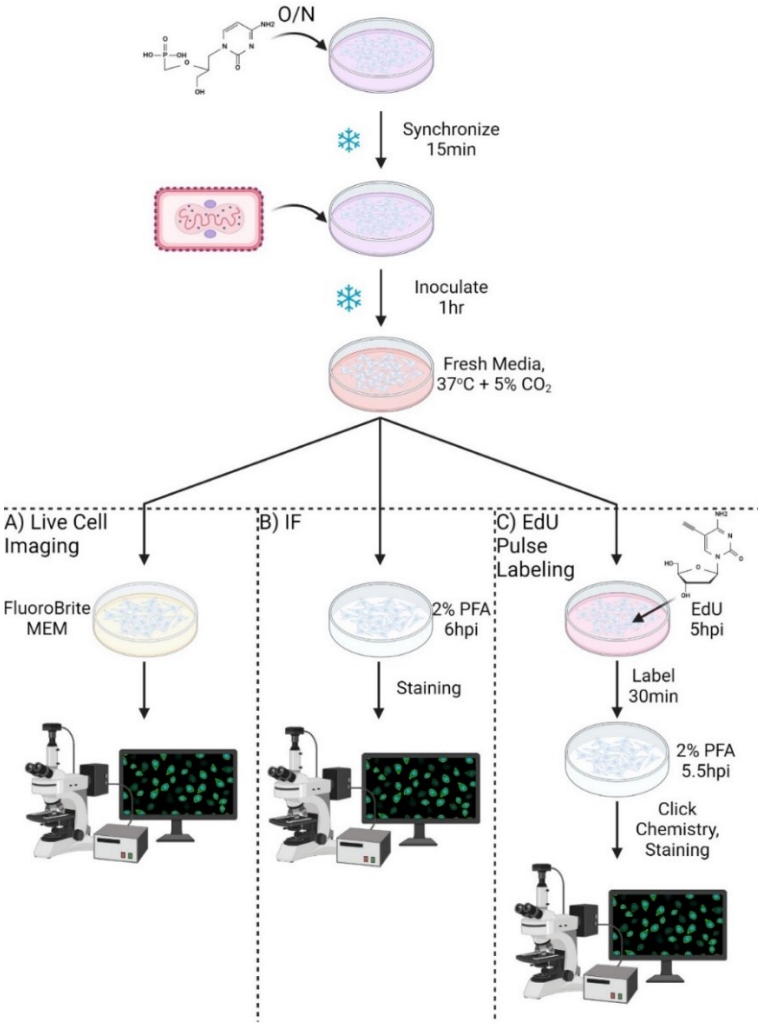

Figure 4.2. General workflow behind microscopy experiments. See sections **2.4.1-3** for detailed methods.

I used VACV pE/L-cro-EGFP (CDV^S EGFP) and VACV pE/L-cro-EGFP VDG1.3 (CDV^R EGFP) for these studies because EGFP is a brighter fluorophore than mKate2. When I infected cells with the CDV^S strain without drug treatment, factories appeared rapidly and expanded continuously up to 6 hours post-infection (**Figure 4.3A**). With CDV pretreatment, the factories appeared but then did not expand appreciably (**Figure 4.3B**).

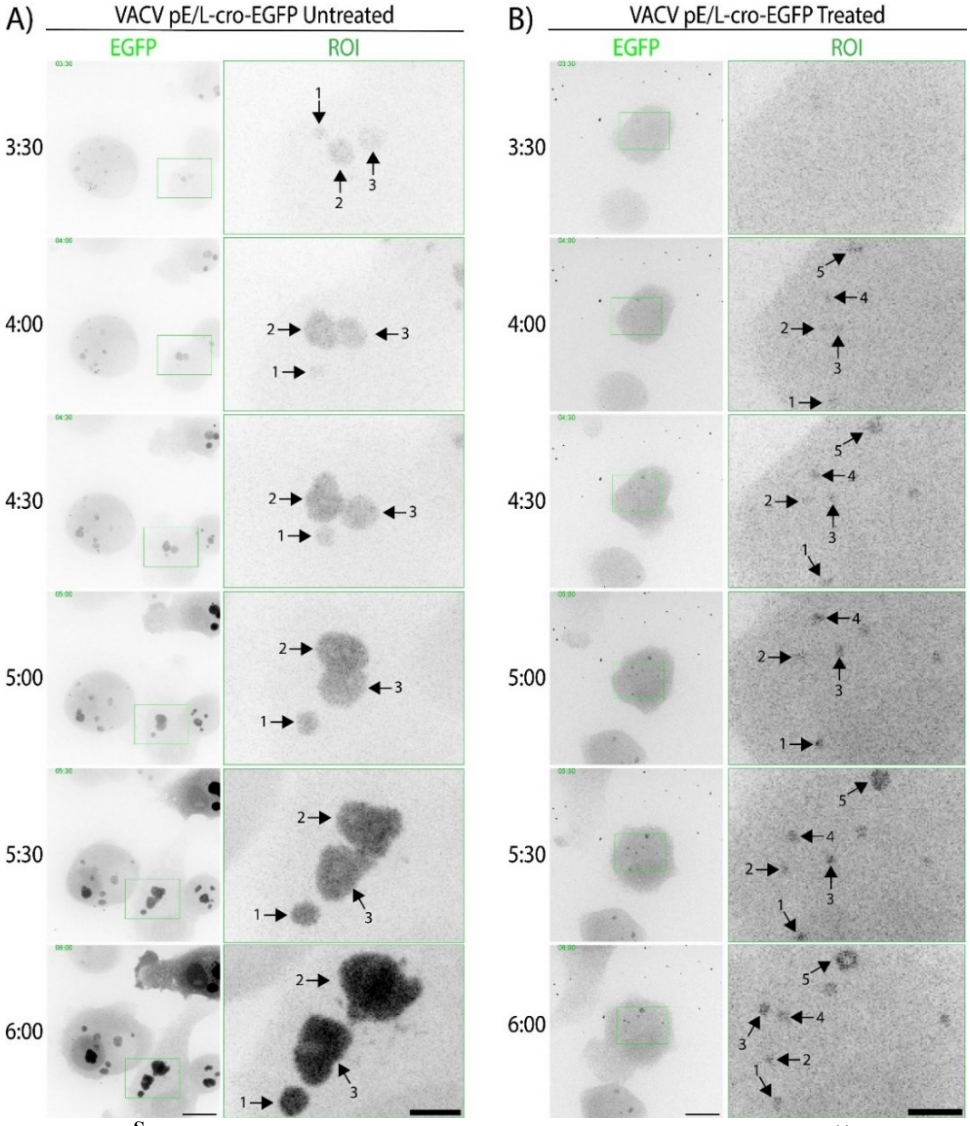

Figure 4.3. CDV^S factories do not expand when exposed to CDV. Cells were synchronously infected with VACV pE/L-cro-EGFP (CDV^S) in the absence (A) or presence (B) of CDV at an MOI of 5. Infected cells were imaged from 3-6 hours post-infection using a WaveFx spinning disc confocal microscope with an Olympus IX-81 camera. Images were processed in Fiji. Numbered arrows indicate single virus factories that do not clearly collide with other factories. Scale bar = 15μm. For ROI, scale bar = 5μm.

I used a 2D brightest point projection to quantify the surface area of each single virus factories (**Figure 4.4A**). First, I used non-linear regression in GraphPad Prism to identify the function that best described the growth of each factory over time. Across three independent biological experiments, the expansion CDV^S factories in the absence of CDV fit exponential growth curves very well. As was expected, factories continued to grow throughout the peak DNA replication phase. Plotting the factory area over time showed that the growth curves for the CDV^S virus flattened after CDV treatment (**Figure 4.4B**). These data showed that at the EC_{90}, 330µm CDV significantly inhibited the factory growth in cells infected with CDV^S VACV. This observation is fully consistent with the drug inhibiting DNA replication.

I next repeated these experiments using the CDV^R VACV strain pE/L-cro-EGFP VDG1.3. In the absence of CDV, the virus factories expanded like the CDV^S strain (**Figure 4.5A**). However, when I pretreated cells with 330µM CDV, unlike what was observed previously, the CDV^R factories continued to expand (**Figure 4.5B**).

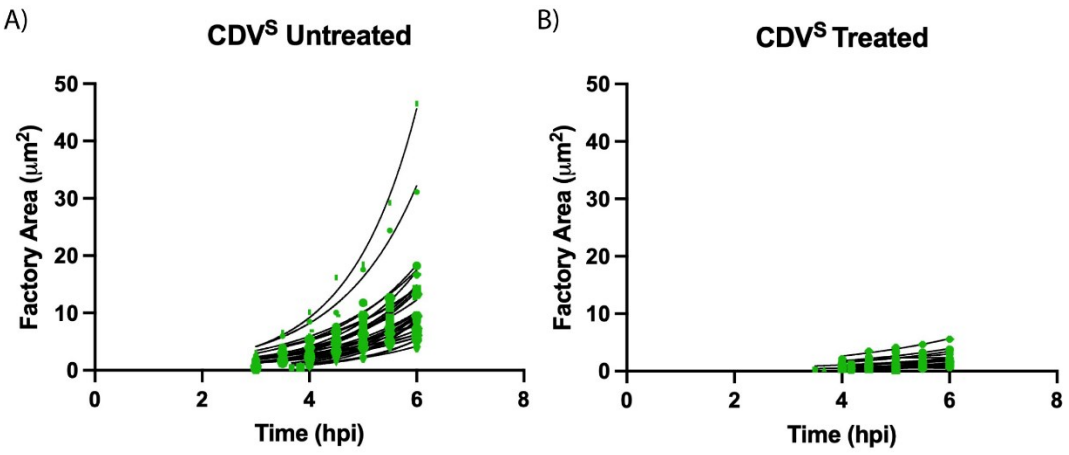

Figure 4.4. Quantification of the 2D brightest point projection of virus factories in Figure 4.3. The ROI tool in FIJI was used to measure the surface area of 2D projected factories. The surface area corresponds to the size of each factory defined by converting pixels to µm. This conversion was based on the scale defined by the WaveFX microscope, which was 6.7007 pixels/µm. The measurements were compiled using >30 factories across > 3 independent biological experiments and plotted in GraphPad Prism. Non-linear regression analyses were performed to generate exponential growth curves to fit the data.

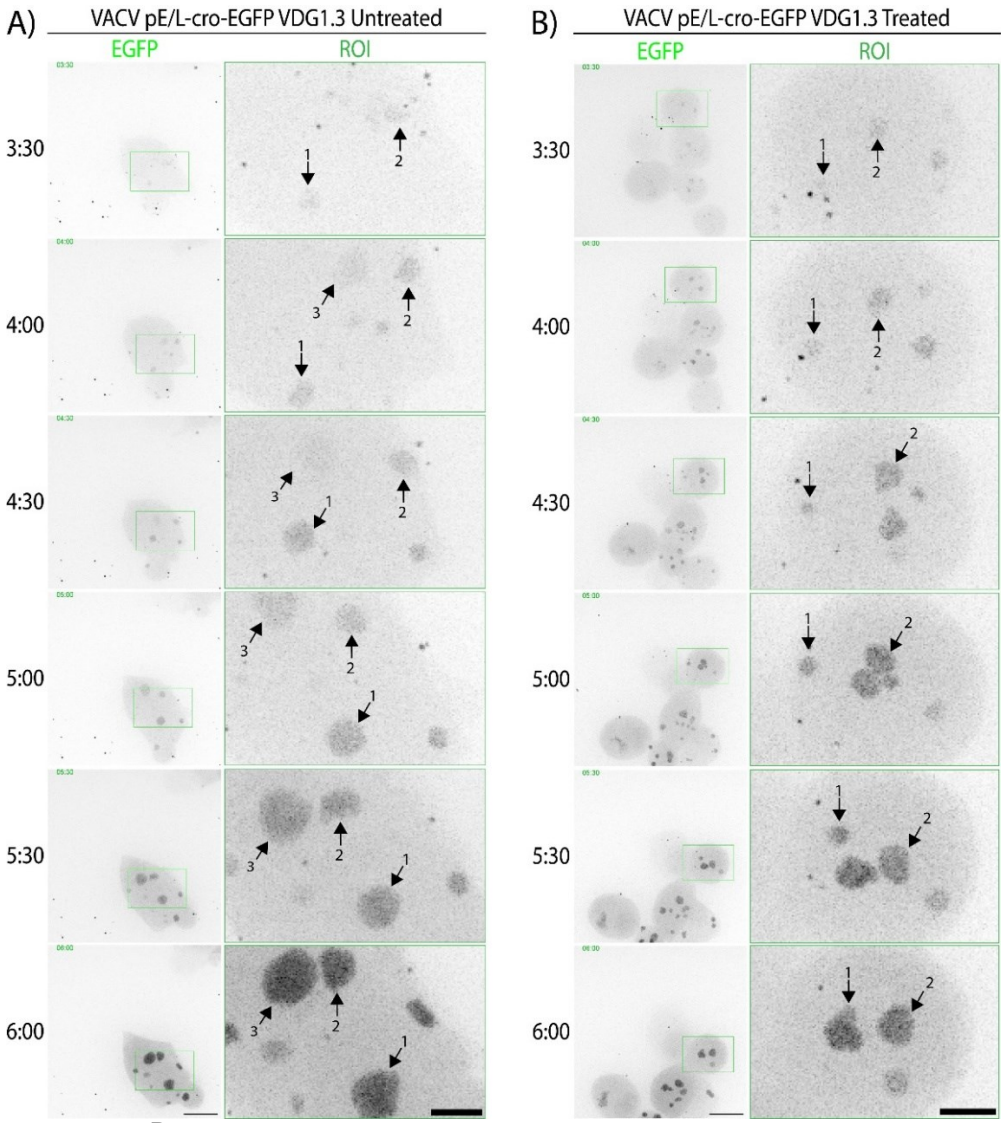

Figure 4.5. CDV^R factories continue to expand despite the presence of CDV. Cells were synchronously infected with VACV pE/L-cro-EGFP VDG1.3 in the absence (A) or presence (B) of CDV at an MOI of 5. Infected cells were imaged and analyzed according to Methods **2.4.1** and **2.6.1**, respectively. Numbered arrows indicate single virus factories that do not clearly collide with other factories. Scale bar = 15μm. For ROI, scale bar = 5μm.

Quantification showed that in the absence of CDV, the CDV^R factories displayed exponential growth like the CDV^S factories (**Figure 4.6A**). When the cells were pre-treated with CDV, the factories maintained exponential growth, showing that the VDG1.3 CDV^R allele permitted normal factory growth in the presence of CDV (**Figure 4.6B**). **Figure 4.7** summarizes all these data. To compare all four groups of data, I extracted the doubling time from each exponential function identified through non-linear regression.

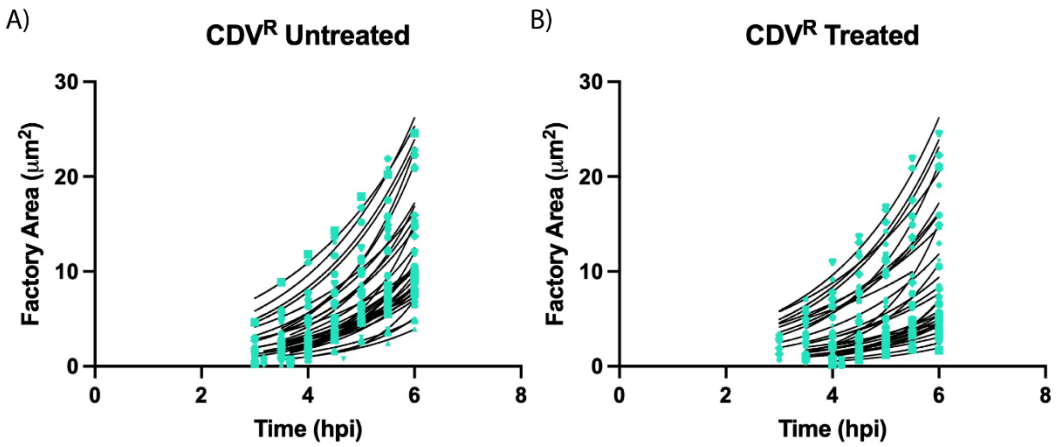

Figure 4.6. Quantification of live-cell images from Figure 4.5. The ROI tool in FIJI was used to measure the surface area of 2D projected factories (See Method **2.6.1** for further detail). The measurements were compiled >30 factories across >3 independent biological experiments and plotted in GraphPad Prism. Non-linear regression analyses were performed to generate exponential growth curves to fit the data.

I then conducted a one-way ANOVA to determine if there were any statistically-significant differences between the groups. The CDV^S strain showed a significantly higher doubling time in the presence of 330μM CDV relative to the CDV^R strain, which indicates that the CDV^S strain grew slower than the CDV^R strain under selective pressure (**Figure 4.7A**). When the data were plotted as a box-and-whisker plot, the distribution of doubling times showed that all virus factories displayed uniform growth rates (**Figure 4.7B**). No factories grew significantly faster or slower than the mean. Lastly, I compiled the R^2 values describing the fit of the exponential growth curves to the data. This showed that on average, exponential expansion poorly represented the growth kinetics of the CDV^S virus replicating in the presence of CDV (**Figure 4.7C**). This observation further showed that – consistent with an antiviral effect on DNA synthesis – the CDV^R strain replicates significantly faster than the CDV^S in cells treated with CDV.

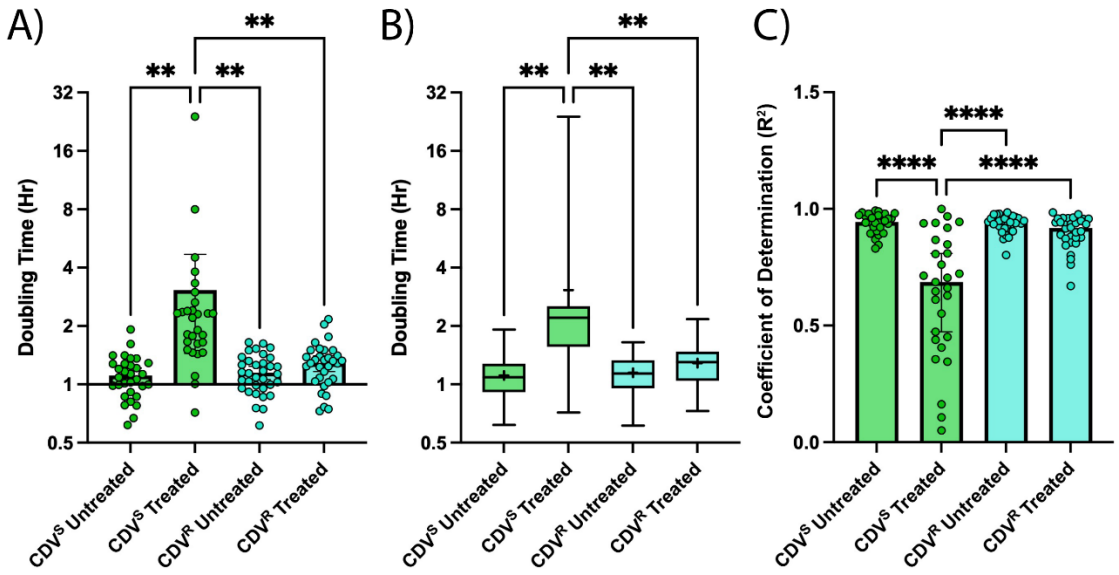

Figure 4.7. CDV reduces the rate of wildtype, CDV^S factory growth. A) Scatter plots of the doubling time as determined by non-linear regression analysis in GraphPad Prism. Each value describes the growth rate of an exponential growth curve fit to measurements of factory area over time. Mean and 95% confidence interval are plotted. B) Box-and-whisker plot of the data from A. + = mean, line = median, box = first and third quartile, whisker = minimum and maximum. C) The R^2 values from the non-linear regression analysis were compiled in GraphPad Prism. Mean and 95% confidence interval are plotted. Statistical analyses were done using a one-way ANOVA with Tukey's multiple comparisons.

4.2.2. High-throughput analysis of factory size in fixed samples

The advantage to live-cell imaging is that it can be used to track a single factory over a time course, providing insights into the behavior and development of the structure. However, live-cell imaging has limitations. With 10-minute intervals and the optimal exposure settings, only about 10 cells can be imaged per experiment. Given the tendency for samples to move out of focus, a 40µm z-stack with 1µm z-slices is also needed to ensure the cells will stay within the field of view. Fixed samples visualized using immunofluorescence microscopy can provide complementary information which, although lacking the dynamic temporal detail of live-cell imaging, can increase the throughput and provide better 3D resolution as one can take smaller z-stacks with finer slices. Therefore, I sought to use immunofluorescence with a monoclonal primary antibody targeting the I3 protein and DAPI counterstaining for cytoplasmic DNA to quantify factory volume and generate a larger distribution of factories for analysis.

I chose to look at VACV factories at 6 hours post-infection in cells cultured with or without 330μM CDV. The live-cell experiments could not detect a substantial difference in factory size at very early time points, but by 6 hours post-infection, a difference in factory size between CDV^S and CDV^R infections was clearly observed (**Figures 4.3** and **4.5**). To quantify factory volume, I used the CDV^S and CDV^R EGFP viruses and included the corresponding mKate2-expressing viruses to ensure that the expression of a different fluorophore did not affect the expansion of the virus factories. I also lowered the MOI to 3 to reduce the likelihood of multiple factories colliding early during infection. In cells that are untreated, imaging showed a very similar phenotype across the four genotypes used (Figure **4.8**). The factories were normally large, perinuclear, and stained strongly with DAPI. After CDV treatment, the CDV^R viruses showed similar-sized factories as in untreated cells; conversely, the CDV^S factories were tiny puncta of DAPI-stained DNA (Figure **4.9**). Notably, the I3 staining was much more concentrated within the factory. One explanation for this observation is that CDV prevented chain extension, which would expose more ssDNA for I3 binding.

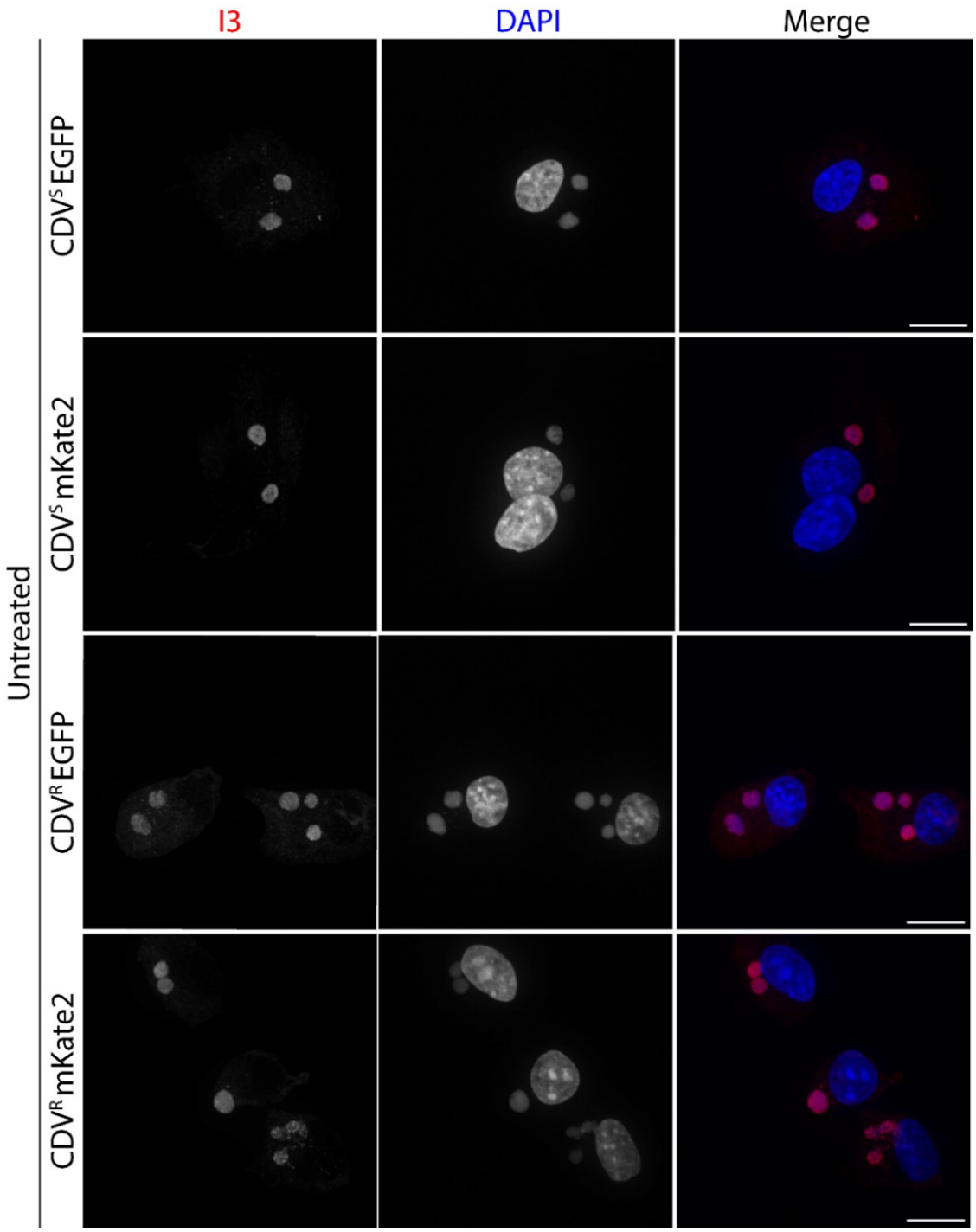

Figure 4.8. All four recombinant viruses make similar sized virus factories in the absence of CDV. BSC-40 cells were synchronously infected with the indicated viruses at an MOI of 3 and fixed at 6 hours post-infection. Cells were processed for immunofluorescence using I3 and DAPI as markers for virus factories. Representative images from >3 independent biological experiments are shown. Scale bar = 15μm.

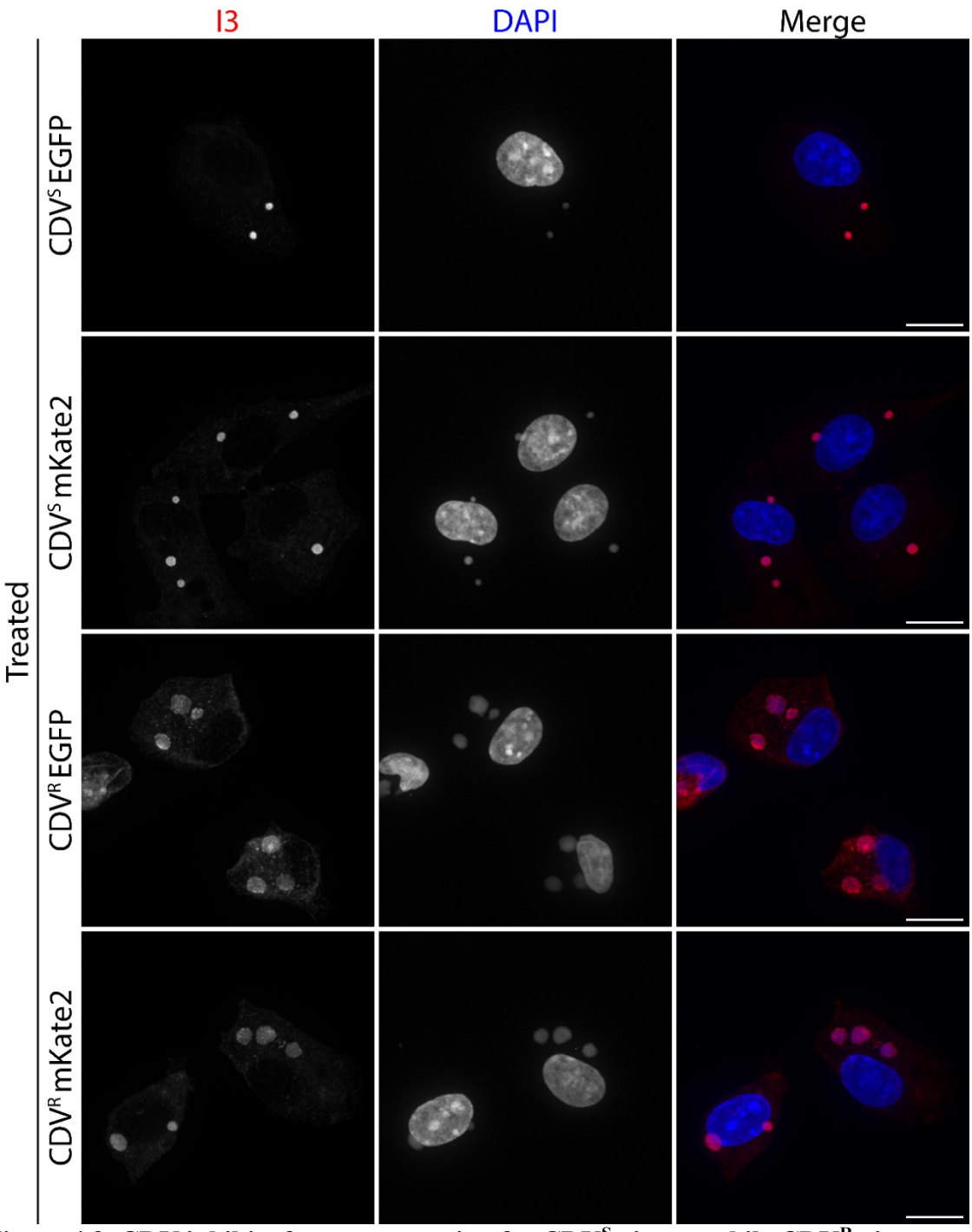

Figure 4.9. CDV inhibits factory expansion for CDV^S viruses while CDV^R viruses still assemble relatively larger factories. BSC-40 cells were pretreated with CDV and synchronously infected with the indicated viruses at an MOI of 3. The cells were fixed at 6 hours post-infection and processed for immunofluorescence microscopy using I3 and DAPI as markers for virus factories. Representative images from >3 independent biological experiments are shown. Scale bar = 15μm.

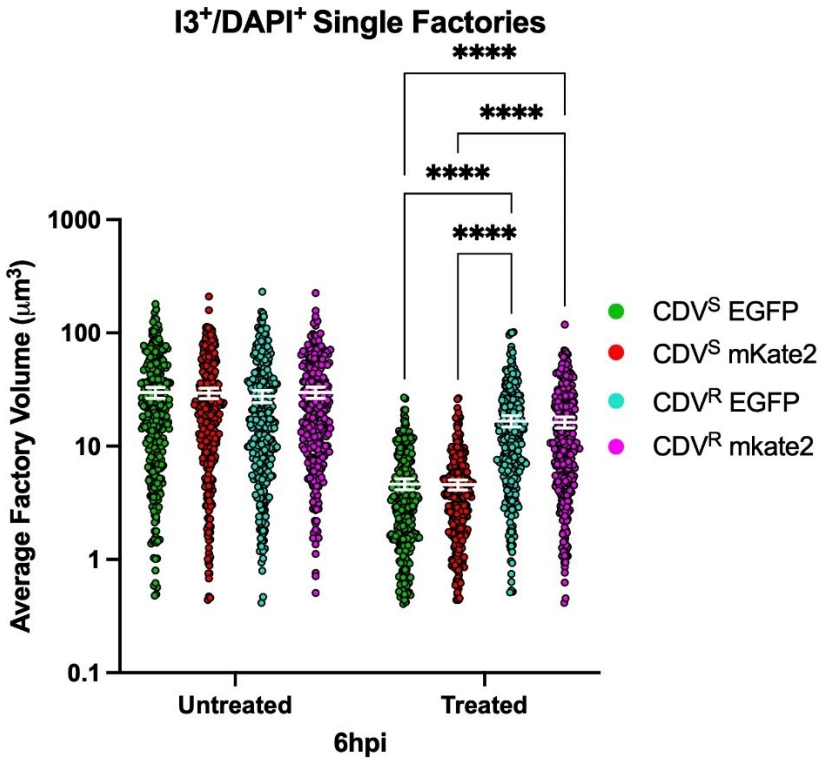

Figure 4.10. CDV can significantly reduce factory size. Volumes were quantified at 6 hours post-infection for all four recombinant viruses using the protocol in Chapter **2.6.2** (Quantification of factory volume). The data were pooled from >3 independent biological experiments and represent a very broad distribution. The data were compiled and analyzed in GraphPad Prism using a two-way ANOVA with Tukey's multiple comparisons. The mean and 95% confidence intervals are also plotted.

Across three independent biological replicates, I measured over 300 factories for all four viruses cultured with or without 330μM CDV. I compiled the volume measurements and performed two-way ANOVA, showing a significant difference between CDV^R and CDV^S factories after CDV treatment (Figure **4.10**). Drug treatment significantly reduced factory volumes, but the CDV^R VDG1.3 polymerase partially rescued viruses. These data confirmed the conclusions from live-cell imaging. Virus factory growth in the presence of CDV will reflect the genotype of the virus. CDV^S strains will display significantly slower factory growth relative to CDV^R strains. After the DNA replication phase, the slow replication of the CDV^S strains in the presence of CDV will result in very small factories. Conversely, the CDV^R strains continuously expand and assemble large virus factories. The high-throughput approach also revealed large variations in factory size across cells despite synchronizing entry (Figure **4.10**). Notably,

the cell cycle was not synchronized during these experiments, so it is possible that some cells have much higher pools of dNTPs available for replication. Synchronizing the cells using serum starvation for an extended period may reduce the variation across many cells.

4.2.3. CDV inhibits DNA replication in a manner consistent with its antiviral activity against E9

The data from live- and fixed-cell imaging showed that CDV significantly reduced factory size. Measuring the DNA content using DAPI proved that there was a reduction in DNA content for CDV^S factories relative to CDV^R factories. These experiments suggested that the drug inhibited DNA replication, but to confirm that enzymatic activity was reduced, I chose to continue with microscopy studies using 5-ethynyl-2'-deoxyuridine (EdU) pulse labelling. EdU is a dTTP analog with a unique ethyne in place of the methyl group on the nitrogenous base. EdU is membrane permeable, and E9 readily incorporates EdU into nascent DNA (119). The ethyne moiety reacts rapidly with azide-containing compounds, allowing fluorescent labelling of sites of active DNA replication after PFA fixation, a process colloquially called click chemistry (141). I hypothesized that if CDV was inhibiting E9, then wildtype factories would display minimal EdU incorporation in the co-presence of CDV, whereas the CDV^R allele would permit robust incorporation of EdU despite the co-presence of CDV.

For this experiment, I infected cells with VACV pE/L-cro-EGFP (CDV^S) or VACV pE/L-cro-mKate2 VDG1.3 (CDV^R) at an MOI of 5, pulsed the cells with 10μM EdU at 5 hours-post infection. I fixed the cells at 5.5 hours post-infection and processed the samples using click chemistry to label the incorporated EdU and immunofluorescence staining using the I3 antibody and DAPI counterstain (**Figure 4.2C**). I chose 5 hours post-infection for the EdU pulse as this was previously identified as the peak time for EdU incorporation (6). In untreated cells, there was robust EdU incorporation after the pulse, indicating active DNA synthesis occurred prior to fixation (Figure **4.11**). However, after CDV treatment, only minimal levels of EdU were detected in CDV^S factories, while CDV^R factories still had incorporated EdU (Figure **4.11**).

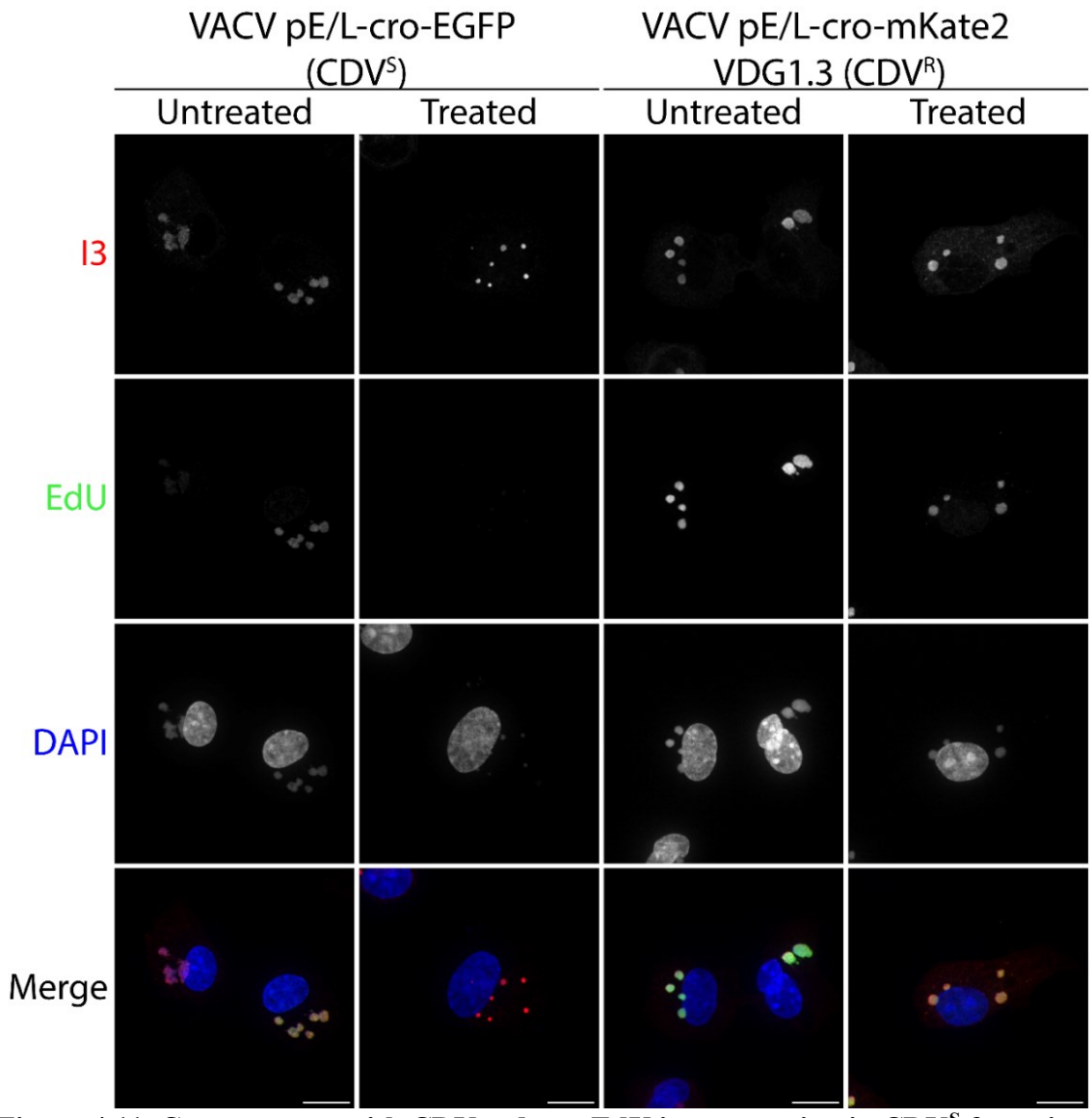

Figure 4.11. Co-treatment with CDV reduces EdU incorporation in CDV^S factories compared to CDV^R factories. BSC-40 cells were infected with VACV pE/L-cro-EGFP (CDV^S) or VACV pE/L-cro-mKate2 VDG1.3 (CDV^R) at an MOI of 5. At 5 hours post-infection, the cells were pulsed with 10μM EdU before fixation at 5.5 hours post-infection. A copper-catalyzed cycloaddition reaction was used to label EdU with a fluorophore before processing the samples for immunofluorescence. Images are representatives from three independent biological experiments. Scale bar = 15μm.

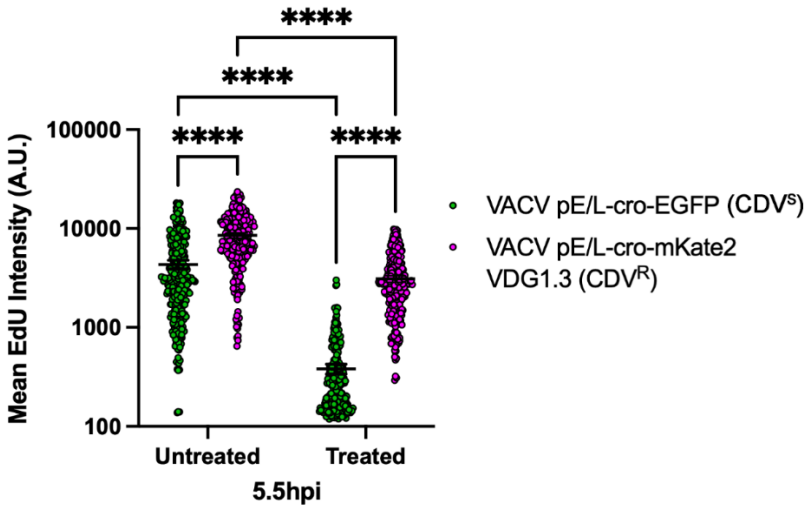

Figure 4.12. CDV significantly reduces EdU incorporation into viral DNA. Images from the EdU pulse labeling experiments were quantified using the protocol in **Figure 2.2**. The distribution shows pooled data from three independent biological experiments with a total of 300 factories analyzed per sample. The data were analyzed in GraphPad Prism using a two-way ANOVA with Šídák's multiple comparisons. Data are the mean and 95% confidence interval.

Two-way ANOVA revealed that a significant reduction in EdU signal was associated with CDV co-treatment for both CDV^S and CDV^R viruses (Figure **4.12**). Interestingly, the CDV^R virus encoding cro-mKate2 incorporated more EdU than the CDV^S virus encoding cro-EGFP in the absence or presence of CDV. To determine if expressing cro-mKate2 or cro-EGFP was responsible for the increased EdU uptake in the CDV^R factories, I swapped the fluorophores so that the CDV^R virus expressed cro-EGFP and CDV^S virus expressed cro-mKate2. These experiments again showed more EdU uptake in the CDV^R factories than in the CDV^S factories (**Figure 4.13**). Quantification revealed that there was significantly more EdU signal detectable in the CDV^R factories compared to CDV^S factories (**Figure 4.14**). This trend replicated the observation that CDV^R polymerase intrinsically incorporated more EdU than the CDV^S polymerase although this difference seemed less pronounced than what I observed in the first set of experiments with the fluorescent proteins switched (**Figure 4.12**). However, the data suggested that there may be a difference in the capacity of mutant and wildtype VACV polymerases to accept EdU as a substrate. This phenomenon will be further discussed in Chapter **6**.

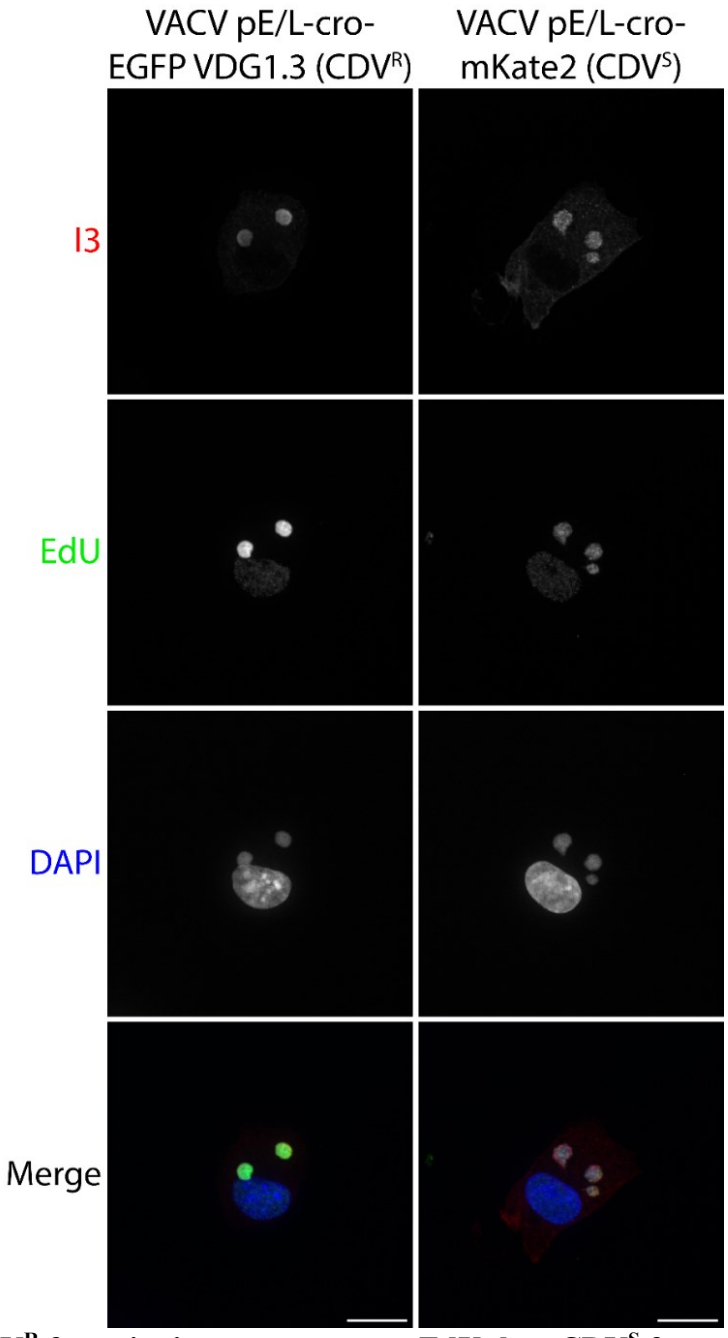

Figure 4.13. CDV^R factories incorporate more EdU than CDV^S factories. BSC-40 cells were synchronously infected with VACV pE/L-cro-EGFP VDG1.3 (CDV^R) or VACV pE/L-cro-mKate2 (CDV^S) at an MOI of 5. At 5 hours post-infection, the cells were pulsed with 10μM EdU before fixation at 5.5 hours post-infection. Copper-catalyzed cycloaddition was used to label EdU with a fluorophore before processing the samples for immunofluorescence. Images are representatives from three independent biological experiments. Scale bar = 15μm.

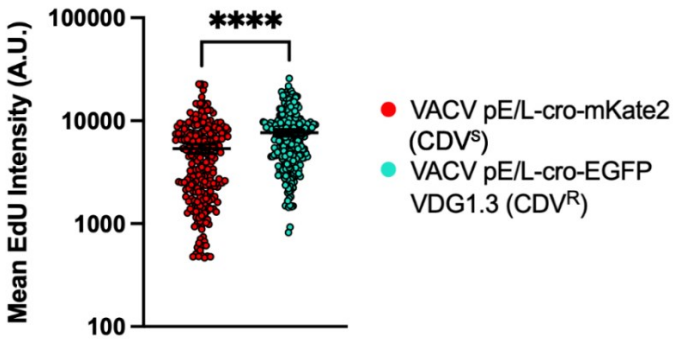

Figure 4.14. The fluorescent signal from EdU is significantly higher in CDV^R factories than CDV^S factories. Images from EdU pulse labeling experiments were quantified using the protocol in **Figure 2.2**. The distribution is the pooled data from three independent biological experiments with 300 factories analyzed per sample. The data were analyzed using an unpaired, two-way t-test. Data are the mean and 95% confidence interval.

4.3. Conclusions

The data presented in Chapter 4 showed that CDV inhibits DNA replication. Previous data was interpreted to suggest that CDV did not inhibit DNA replication; instead, the authors argued that CDV prevents proper genome encapsidation (137). I used a combination of imaging techniques to re-evaluate the previous proposal, taking care to provide sufficient time for CDV adsorption into the cells and bioactivation into CDVpp. Live-cell imaging showed that CDV^S viruses make factories but there is almost no factory growth in the presence of CDV (**Figure 4.4B**). Conversely the CDV^R allele promoted rapid factory growth in the presence of CDV (**Figure 4.6B**). A more high-throughput analysis using fixed samples confirmed that CDV^S virus factories are significantly smaller than CDV^R virus factories when there is CDVpp present in the cell (**Figure 4.10**). EdU pulse-labelling further showed that CDV inhibits DNA synthesis as judged by a concomitant decrease in EdU incorporation. These data showed that the biochemical studies from Magee *et al.* are consistent with what is happening in infected cells. CDVpp competes for dCTP binding at the E9 active site and inhibits further synthesis after being incorporated into the growing daughter strand (102, 103). This process will arrest viral growth at an early stage, decreasing the number of resolved genomes available for encapsidation. Ultimately, this will reduce the yield of mature virus from an infected cell. The antiviral mechanisms of CDV will be further discussed in Chapter **6**.

Chapter 5. Coinfection studies using wildtype and cidofovir-resistant vaccinia viruses to investigate inter-virus growth competition

5.1. Introduction

Having established how CDV would affect factory growth, I proceeded to experiments examining how viruses interact during coinfection. Previous observations showed that β-galactosidase could be retained in virus factories despite the enzyme lacking a function relevant to the viral lifecycle (43). The authors also showed that cells coinfected with viruses expressing the VACV structural protein A5 fused to yellow or cyan fluorescent proteins (YFP or CFP) generated exclusively YFP-positive or CFP-positive factories. Work from the Evans laboratory also showed that virally-encoded EGFP-cro and mCherry-cro selectively labelled viral factories (120). These observations suggested that virus factories might sequester newly-synthesized proteins and were the basis for the hypothesis that CDV^R and CDV^S viruses may compete in coinfected cells. The studies in Chapter **4** showed that CDV inhibits VACV factory growth, but CDV^R viruses maintained continuous growth in the presence of CDV. I hypothesized that if there was competition between coinfecting CDV^R and CDV^S viruses, there would be a significant difference in factory growth between the two strains as the CDV^R VDG1.3 polymerase would be retained in the factories of genetic origin. To test this hypothesis, I conducted live-cell imaging using coinfected cells. I also conducted experiments to examine how mixed populations of viruses responded to CDV treatment at a larger scale. Because drug selection acts on populations, any potential competition observed between single factories should translate to changes in the population.

5.2. Results

5.2.1. cro-EGFP and cro-mKate2 colocalize in coinfected cells

Previous experiments suggested that cro-tagged fluorophores would selectively label the virus factories, and the clearly distinguishable EGFP-cro and mCherry-cro fluorescence was used to mark the genotype of the factories (120). I expected that my reporter viruses would exhibit the same selectivity as EGFP-cro and mCherry-cro proteins. However, instead of each fluorescent protein uniquely labelling a particular factory in a coinfected cell, these coinfected cells always showed cro-EGFP and cro-mKate2 colocalized (**Figure 5.1A, Panels iii and v**). This was not an imaging artifact as the EGFP and mKate2 spectra are well-separated, and the emission lasers and excitation filters should not permit bleed-through (see chapter **2.4.1** and **Table 3.1**). For example, I also observed infected cells with virus factories showing mKate2 fluorescence without EGFP fluorescence (**Figure 5.1B, Panels iv& vi**) Likewise, I also observed virus factories that were EGFP-positive and lacked mKate2 fluorescence (**Figure 5.1A, Panels iv & vi)**. These data implied that DNA binding proteins can diffuse out of the factory from which they originated and potential mechanisms are discussed in Chapter **6**. The redistribution of cro-EGFP and cro-mKate2 between coinfecting viruses prevented using the fluorophore to identify the associated *E9L* allele. Unfortunately, this then complicated experiments optically tracking the rate of growth of individual CDV^R and CDV^S viruses in coinfected cells. However, I still proceeded with some live-cell imaging experiments to determine if there are differences in growth kinetics between coinfecting CDV^R and CDV^S factories in the presence of CDV.

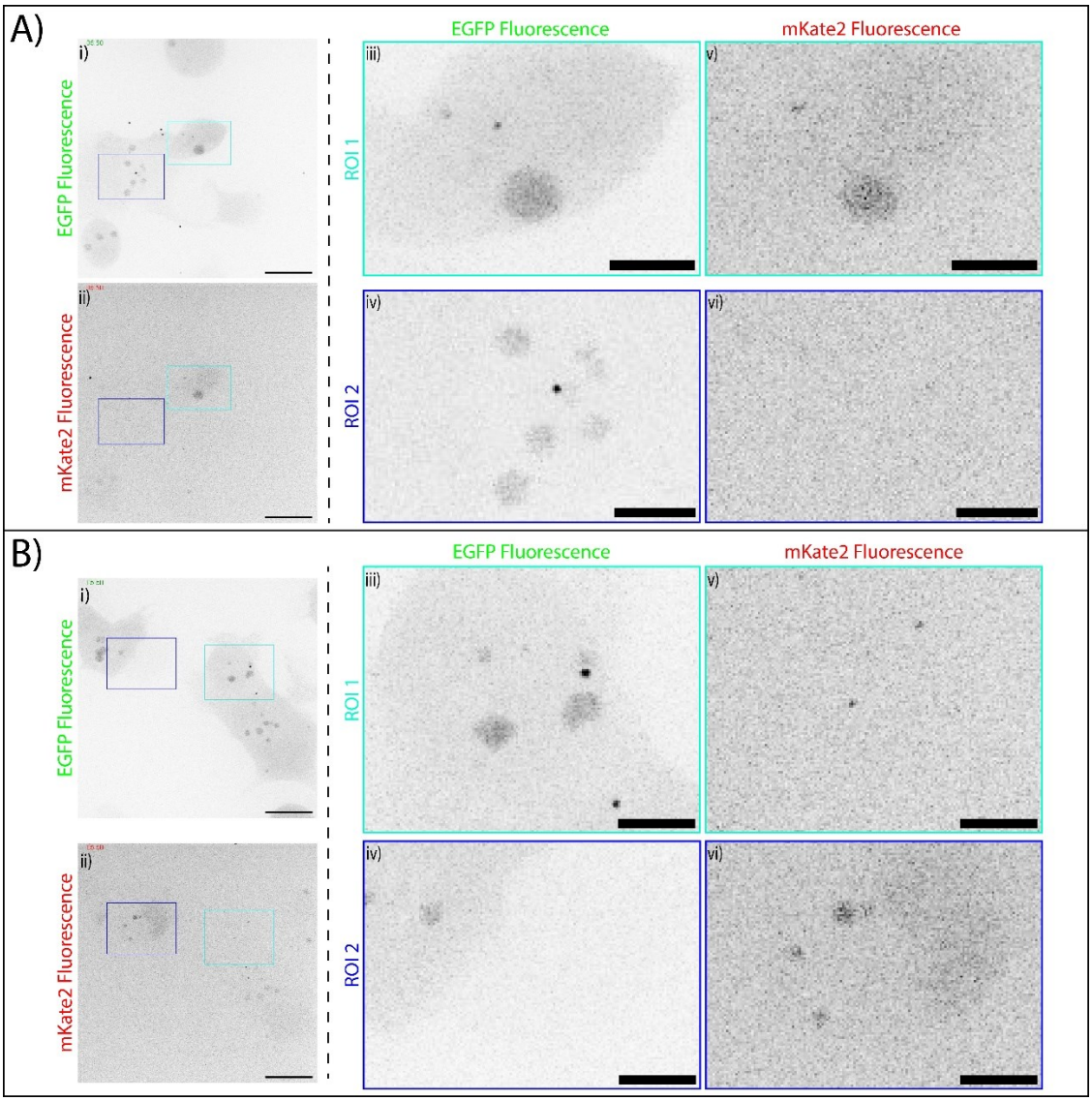

Figure 5.1. cro-EGFP and cro-mKate2 colocalize in coinfected cells but do not bleed through into other channels. A) BSC-40 cells were synchronously infected with VACV pE/L-cro-EGFP (CDV^S) and VACV pE/L-cro-mKate2 VDG1.3 (CDV^R) at a combined MOI of 5. The images were processed in Fiji to add two ROIs highlighting one coinfected cell (ROI 1 cyan, panels iii and v) and one cell infected only with VACV pE/L-cro-EGFP cell (ROI 2 blue, panels iv and vi). B) The cyan ROI highlights a cell infected with VACV pE/L-cro-EGFP (CDV^S) that shows cro-EGFP in virus factories without any fluorescent signal from mKate2 (ROI 1, panels iii and v). The blue ROI highlights a cell infected with VACV pE/L-cro-mKate2 VDG1.3 (CDV^R) that shows cro-mKate2 in virus factories without any fluorescent signal from EGFP (ROI 2 panels iv and vi).. Scale bars = 15µm. ROI scale bars = 5µm.

5.2.2. Coinfecting virus factories display uniform growth kinetics

Based on the single-infection experiments I conducted in Chapter **4**, if coinfecting viruses were in competition for growth, then you might expect to see a replicating population of factories and an inhibited population of factories, presumably corresponding to CDV^R and CDV^S viruses. These populations should be clearly separated in a distribution of data recording factory sizes, unlike what was observed using single infections (**Figure 4.7B**). Conversely, if the encoded E9 proteins in the factories were shared, then you might expect all the factories to grow at some average rate that is dependent on MOI. If the ratio favoured wildtype virus, you would expect the growth rate to approach something closer to how wildtype viruses grow in the presence of CDV because there would be proportionally more wildtype polymerase in the cell. To investigate this, I conducted live-cell imaging experiments essentially as in Chapter **4.2.1** except that I coinfected the cells with a 1:1 ratio of CDV^R-to-CDV^S viruses at a combined MOI of 5. In untreated cells, the factories appeared and expanded from the earliest timepoint (**Figure 5.2A**). The imaging showed some cells with higher levels of mKate2, which was likely because some cells got more mKate2-encoding virus. The amount of virus present in the cell influences the level of protein synthesis (130). In CDV-treated cells, the factories appeared to grow at uniform rates albeit at a slower rate than in the absence of CDV (**Figure 5.2B**). In a subsequent experiment, I changed the mutant-to-wildtype ratio to 1:5 to see if this altered the average growth kinetics. When I imaged these cells, the EGFP signal intensity was quite weak, showing that – as expected – there was less of the CDV^R VACV pE/L-cro-EGFP VDG1.3 (**Figure 5.3**). Again, I observed that all the factories seemed to be growing at the same rate. I proceeded to analyze the data using the same method as in Chapter **4.2.1**.

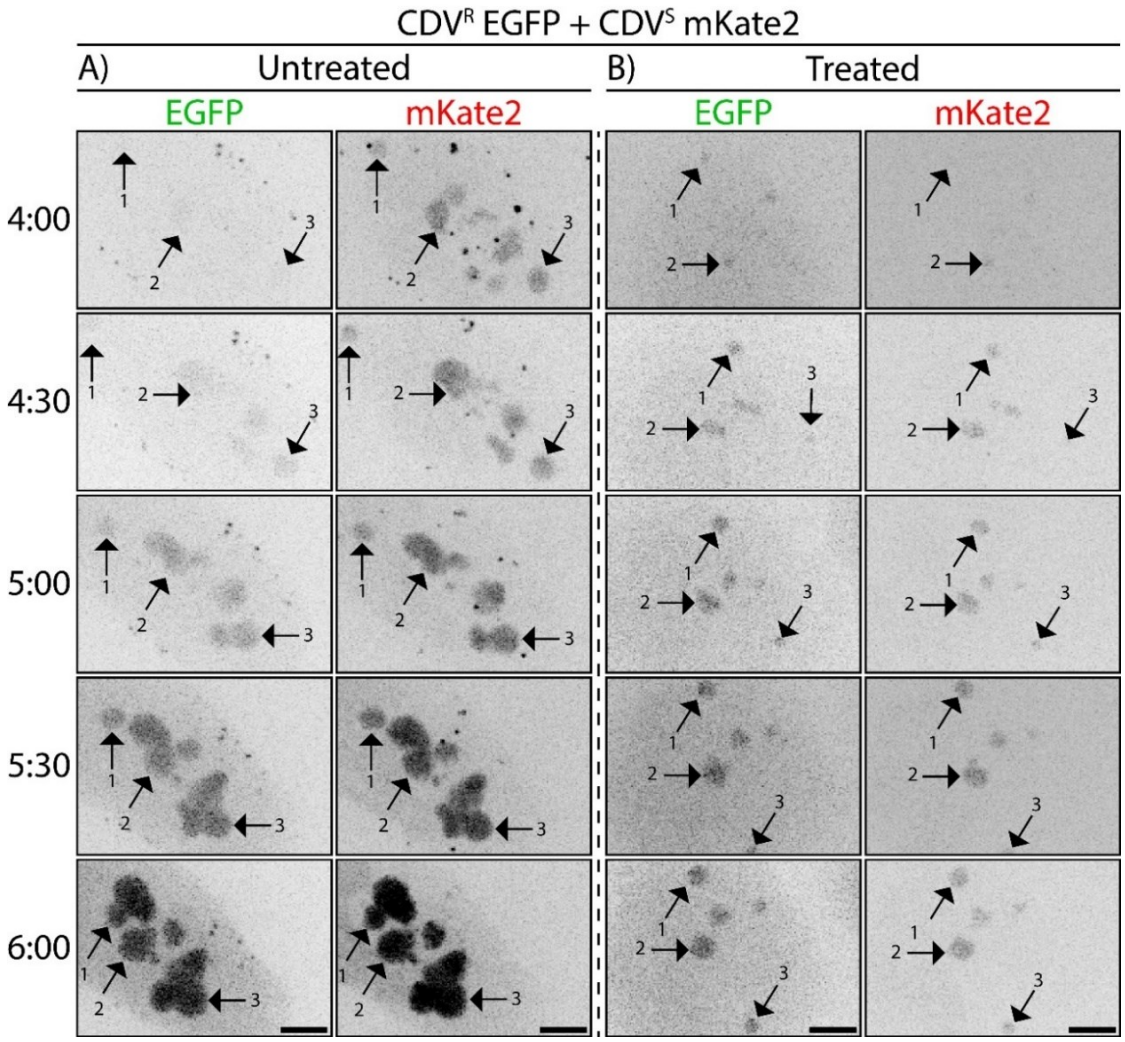

Figure 5.2. Live-cell imaging of coinfected cells in the presence or absence of cidofovir. Cells were synchronously coinfected with VACV pE/L-cro-EGFP VDG1.3 (CDV^R) and VACV pE/L-cro-mKate2 (CDV^S) at a 1:1 ratio with a combined MOI of 5 in the absence (A) or presence (B) of 330μM CDV. Infected cells were imaged and analyzed according to Methods **2.4.1** and **2.6.1**, respectively. Numbered arrows indicate single virus factories that did not clearly collide with other factories. These images were extracted from larger images using the ROI tool for simplicity in presenting the data. Scale bar = 5μm. Images are a representative set from >3 independent biological experiments.

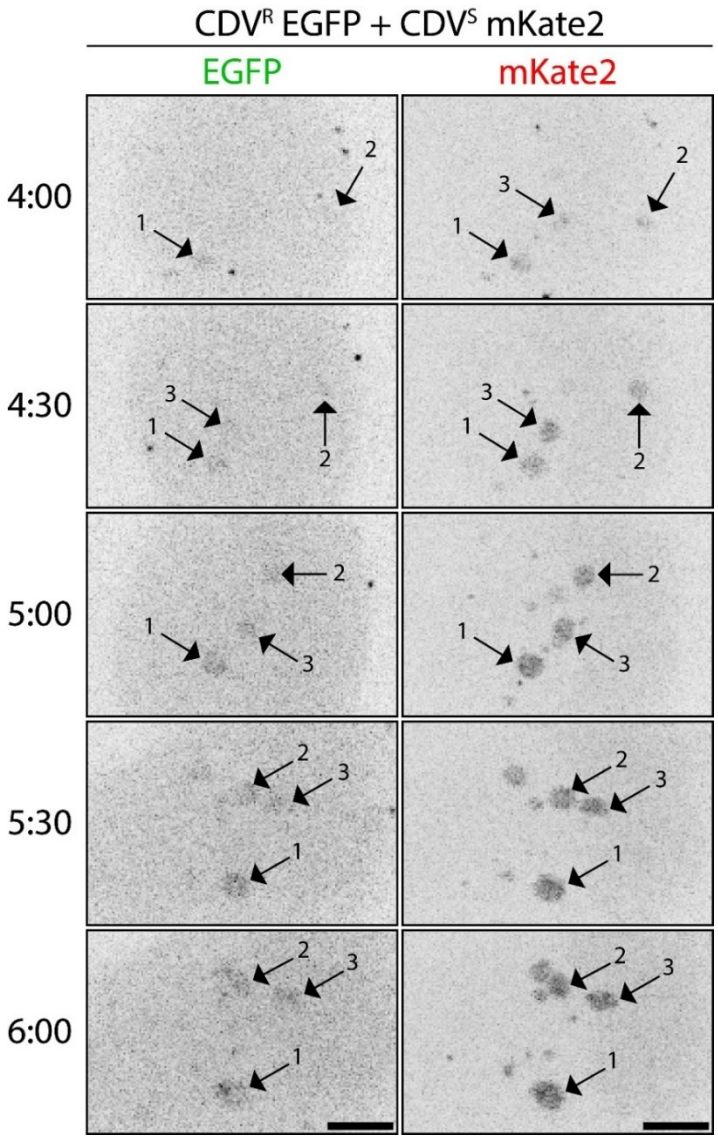

Figure 5.3. Live-cell imaging of coinfected cells after changing the ratio of CDV^S-CDV^R viruses. Cells were synchronously coinfected with VACV pE/L-cro-EGFP VDG1.3 (CDV^R) and VACV pE/L-cro-mKate2 (CDV^S) at a 1:5 ratio of CDV^R-CDV^S viruses with a combined MOI of 6 in the presence of CDV. Infected cells were imaged and analyzed according to Methods **2.4.1** and **2.6.1**, respectively. Numbered arrows indicate single virus factories that do not clearly collide with other factories. These images were extracted from larger images using the ROI tool for simplicity in presenting the data. Scale bar = 5μm. Images are a representative set from >3 independent biological experiments.

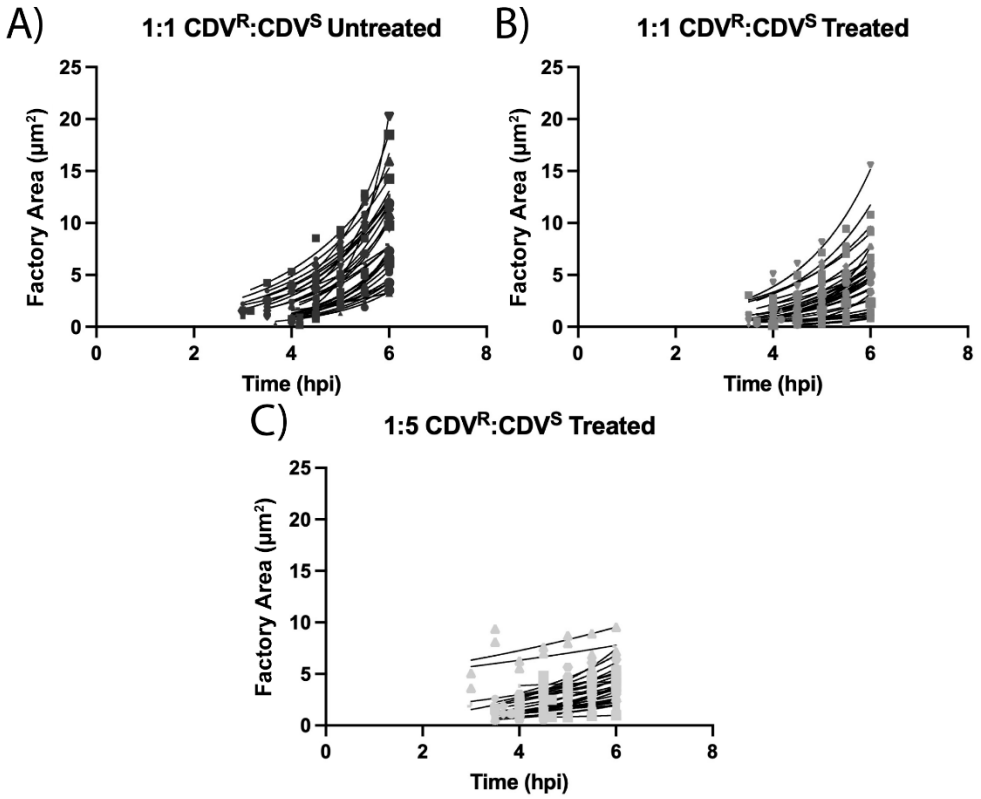

Figure 5.4. Quantification of data from Figures 5.3 and 5.4. The ROI tool in FIJI was used to measure the surface area of 2D projected factories (See Method **2.6.1** for further detail). The measurements were compiled >30 factories across >3 independent biological experiments and plotted in GraphPad Prism. Non-linear regression analyses were performed to generate exponential growth curves to fit the data.

Quantification of the live-cell imaging data confirmed these observations. In untreated cells, one observes that the factories exhibit exponential growth (**Figure 5.4A**). In the presence of drug, the factories still showed fairly strong growth that was best fit with exponential growth curves (**Figure 5.4B**). There did not seem to be distinguishable populations of fully resistant and highly sensitive (i.e. non-expanding) virus factories. Interestingly, when I reduced the proportion of mutant virus present, the factories displayed flatter growth curves although factory expansion was still detected (**Figure 5.4C**). With a 1:1 ratio of CDV^{R}-to-CDV^{S} viruses there was no significant difference in the average doubling time of the exponential growth curves between the untreated and CDV-treated cells (**Figure 5.5A**). However, the average doubling time significantly increased when the ratio of CDV^{R}-to-CDV^{S} viruses was changed from 1:1 to 1:5 (**Figure 5.5A**).

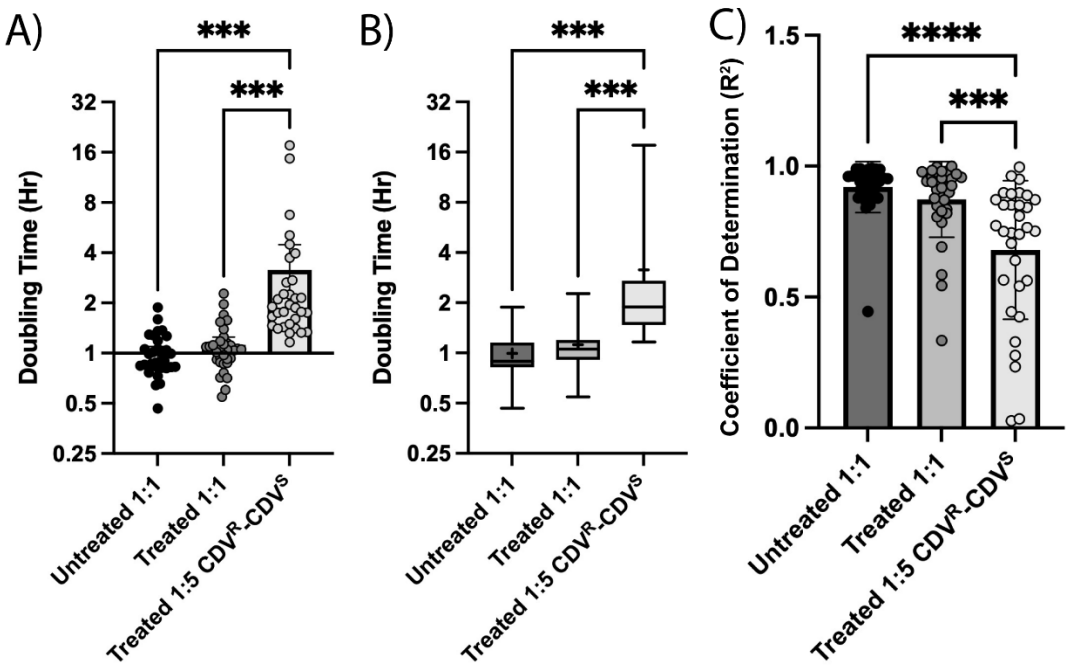

Figure 5.5. Factory growth is uniform and dependent on the amount of wildtype virus present. A) Scatter plot of doubling time as determined by non-linear regression analysis in GraphPad Prism. Each value describes the growth rate of an exponential growth curve fit to measurements of factory area over time. Mean and 95% confidence interval are plotted. B) Box-and-whisker plot of the data from A. + = mean, line = median, box = first and third quartile, whisker = minimum and maximum. C) The R^2 values from the non-linear regression analysis were compiled in GraphPad Prism. Mean and 95% confidence interval are plotted. Statistical analyses were done using a one-way ANOVA with Tukey's multiple comparisons.

I also plotted the data as box-and-whisker plots to see whether there were outliers falling outside the normal distribution (**Figure 5.5B**). Interestingly, none of the data could be found in the 2.5% on either end of the normal distribution, indicating that there were no outliers that grew at a mathematically higher or lower rate than the mean. The same uniformity of growth occurred in experiments with single infections (**Figure 4.7B**). These data suggested that the presence of the excess CDV^S virus interfered with the growth of the mutant. Given that the fluorophores colocalized, it is reasonable to hypothesize that the polymerases can also mix and allow the CDV^R mutant to rescue the replication of the CDV^S wildtype.

To directly test this model, I used fluorescence *in situ* hybridization (FISH) to differentiate between the DNAs of these coinfecting viruses. A combination of FISH and immunofluorescence previously allowed the differentiation of coinfecting genomes (121).

Because the genes encoding cro-EGFP and cro-mKate2 are so similar at the DNA level, for these studies I chose to use VACV pE/L-cro-EGFP (CDV^S) plus the CDV^R parent strain. This strategy avoids cross-hybridization between cro-EGFP and cro-mKate2 that might cause problems with a probe targeting EGFP. Using this approach, I could differentiate between CDV^S and CDV^R viruses in coinfected cells (**Figure 5.6**). Although the probe did show some background signal, I could still easily find areas with a concentration of FISH probe, and these regions were also $I3^+/DAPI^+$ virus factories. The FISH probe displayed a speckled pattern in virus factories, which may indicate areas where replication was active and the DNA more accessible. This pattern was also described previously and perhaps warrants further investigation (121). I could also detect factories lacking a strong signal from the probe (**Figure 5.6,** see Merge ROI). I designated FISH-labeled factories as CDV^S viruses (i.e. encoding cro-EGFP and a linked CDV^S E9L allele) and factories without probe as the CDV^R VDG1.3 strain. I used this method to quantify virus factory size at 6 hours post-infection. This analysis showed that there was no difference between mutant and wildtype factories (**Figure 5.7**).

Collectively, these data showed that when cells are coinfected with CDV^R and CDV^S viruses, the CDV^S virus interferes with the growth of the CDV^R virus. In the presence of CDV, CDV^R and CDV^S viruses will grow at a rate that is the average of the growth from the mixture of drug-resistant and drug-sensitive polymerases (**Figure 5.5**). When the proportion of CDV^S viruses increases, the growth rate for all coinfecting viruses decreases, which indicates that the CDV^R virus loses the growth advantage displayed in single infections. These observations suggest that in a mixed population of viruses, the CDV^R viruses may not outgrow the CDV^S viruses when the viruses coinfect cells.

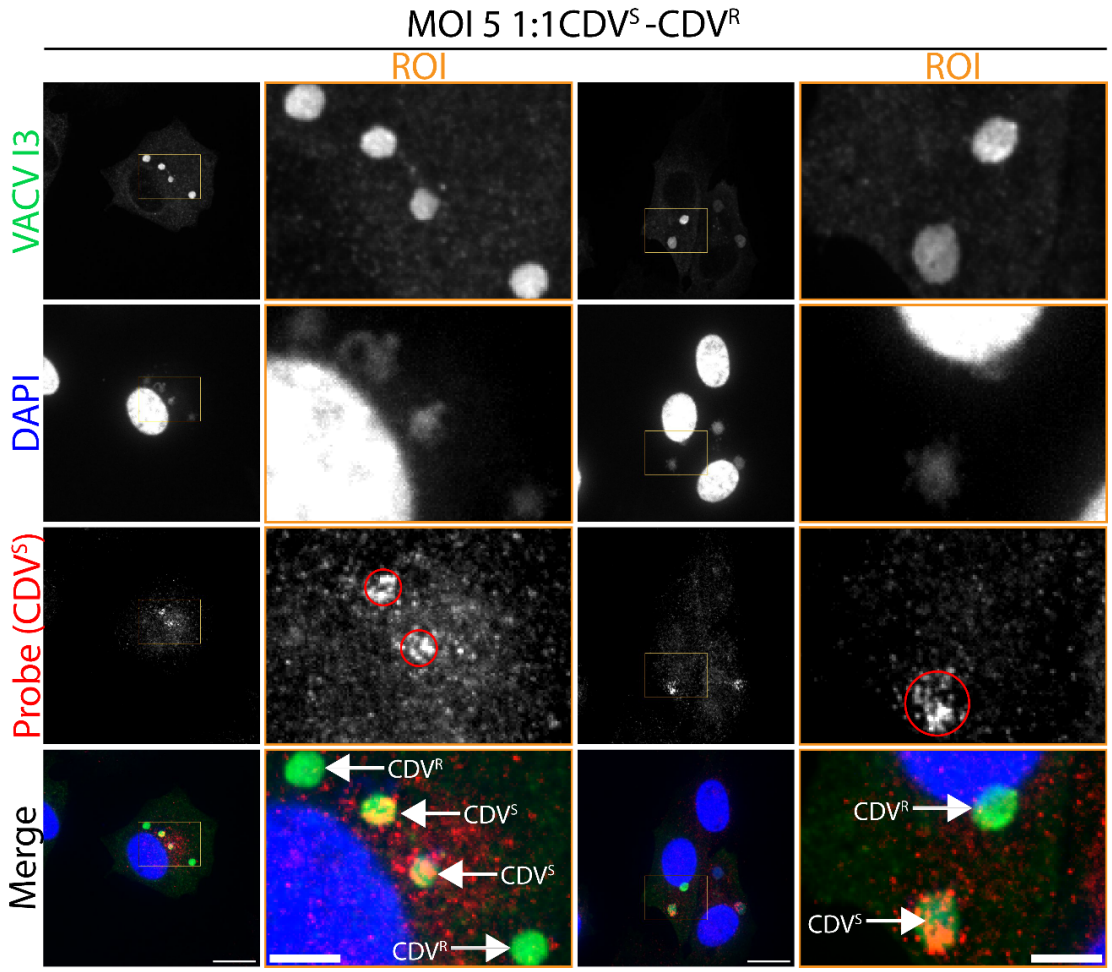

Figure 5.6. FISH targeting viral genomic DNA. Cells were pretreated with CDV and synchronously infected with VACV pE/L-cro-EGFP and VACV VDG1.3 at a combined MOI of 5. The infection was fixed at 6 hours post-infection and processed for FISH and immunofluorescence. Two representative cells are shown with an ROI (magenta) beside the full-size image. Red circles in the ROI indicate areas where the FISH probe was concentrated. Arrows are used to show wildtype and mutant viruses. Scale bar = 15μm. ROI scale bar = 5μm.

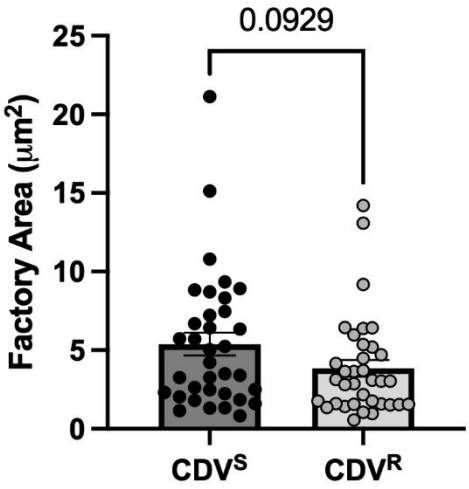

Figure 5.7. Wildtype and mutant factories are the same size despite CDV treatment. A) The ROI tool in FIJI was used to measure the surface area of 2D projected factories (See Method **2.6.1** for further detail). The measurements were compiled >30 factories across two independent experiments and plotted in GraphPad Prism. The data were analyzed using an unpaired, two-way t-test.

5.2.3. Cidofovir-resistant mutants cannot outgrow wildtype viruses in coinfected cells

The intracellular analysis of factory growth rates suggested that the VDG1.3 strain encoding the CDV^R allele gained no advantage over wildtype viruses in coinfected cells. To supplement the microscopy, I wanted to study how a mixed population of viruses changed in composition under selection in the presence of CDV. I performed high MOI coinfections using VACV pE/L-cro- EGFP VDG1.3 (CDV^R) and VACV pE/L-cro-mKate2 (CDV^S) in the presence or absence of CDV (**Figure 5.8**). In the proceeding figures, the progeny mixtures from coinfections are labelled based on the coinfection condition, either CDV^- or CDV^+. CDV^- are progeny from coinfections without selection from CDV, whereas CDV^+ are progeny from coinfections with 330μM CDV. An MOI of 10 ensured that all cells were coinfected. I also examined how the composition of the resulting virus stocks would change depending upon whether the starting ratio was set at a 1:1 or 1:10 ratio of CDV^R-to-CDV^S viruses. In the case that the starting ratio was 1:10, the MOI was 11, reflecting 1 CDV^R virus and 10 CDV^S viruses entering the cells. After recovering the virus from coinfected cells 16-20 hours post-infection, the progeny

were plated at low dilution on BSC-40 cells in the absence of CDV and the resulting green and red plaques counted using an Agilent Cytation fluorescence plate scanner.

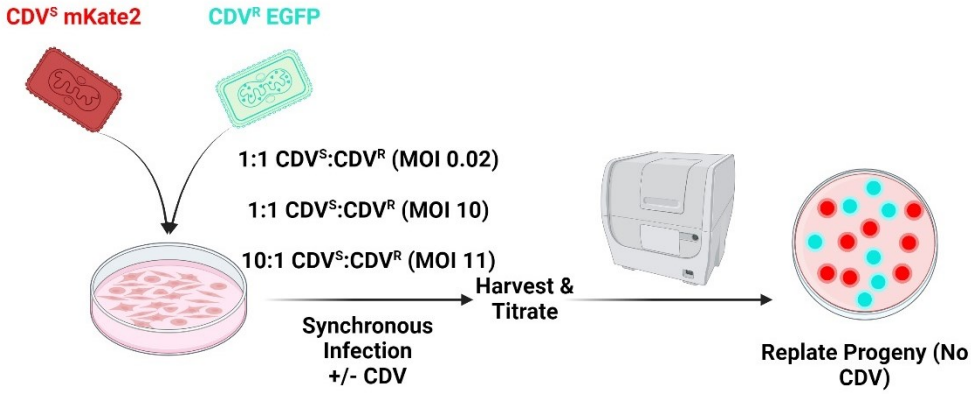

Figure 5.8. Visual representation of coinfection studies. The detailed method is in chapter **2.5.4.**

Plating the progeny in the absence of CDV generated a mixture of plaques that reflected the frequency of the two strains in the population after coinfection. Plating the progeny on cells treated with CDV would eliminate any CDV^S viruses, so the frequency of the CDV^S strain would not be accurate (**Figure 3.5**). By comparing the frequency of CDV^R and CDV^S viruses before and after coinfection, I sought to determine if the CDV^R virus had a selective growth advantage compared to the CDV^S virus. I hypothesized that – based on the observations from Chapter **5.2.2** – selection from CDV would not favour the replication of the CDV^R virus, meaning there would be no significant change in the frequency of the CDV^R virus after coinfection. One caveat to these experiments was that recombination between *E9L* and the *J2R* loci could alter the relationship between the fluorescent marker genes and the *E9L* locus. However, I reasoned that this would have a minimal impact on the results of the experiment as previous studies showed that the recombination rate between viruses at high MOI is only 1-3% (120). Recombination is therefore unlikely to substantially alter linkage between the CDV marker in *E9L* and the colour of the plaques. A fluorescent green plaque is assumed to encode the CDV^R *E9L* allele (VACV pE/L-cro-EGFP VDG1.3), a red plaque a CDV^S wildtype E9L allele (VACV pE/L-cro-mKate2).

To ensure that infections occurred at high MOI, I titrated the input samples and found that the mean titer across three experiments was above 10^7 PFU/mL, which corresponded well to an MOI of 10 for each well. After replication, the mean titer decreased independent of drug treatment (**Figure 5.9**). Representative images of each sample and condition are shown in **Figure 5.10**.

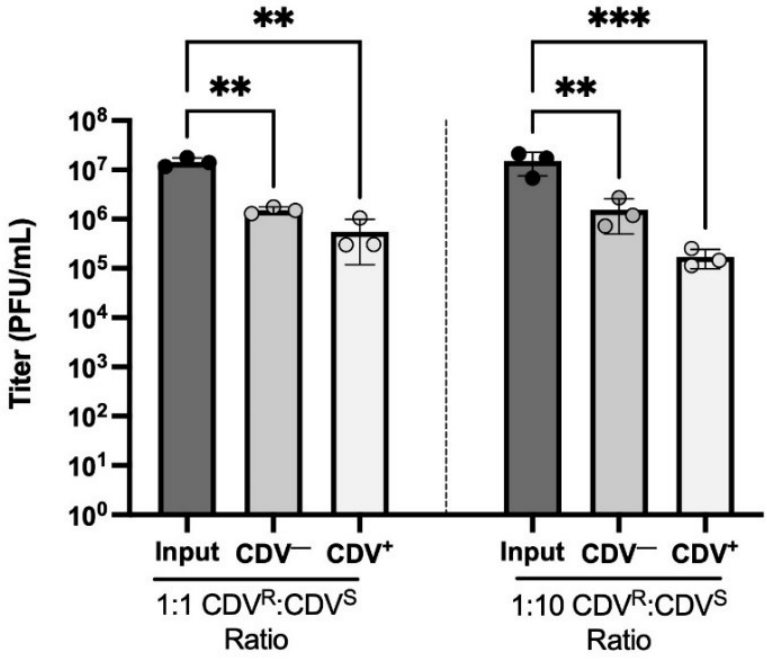

Figure 5.9. The concentrations of the input samples guaranteed a high MOI and high likelihood of coinfection. The input and progeny samples (CDV^- or CDV^+) were titrated on BSC-40s in the absence of CDV. The data are plotted as the mean of three biological replicates ± standard deviation. The data were analyzed in GraphPad Prism with one-way ANOVA with Tukey's multiple comparisons. The 1:1 group and 1:10 group were analyzed separately.

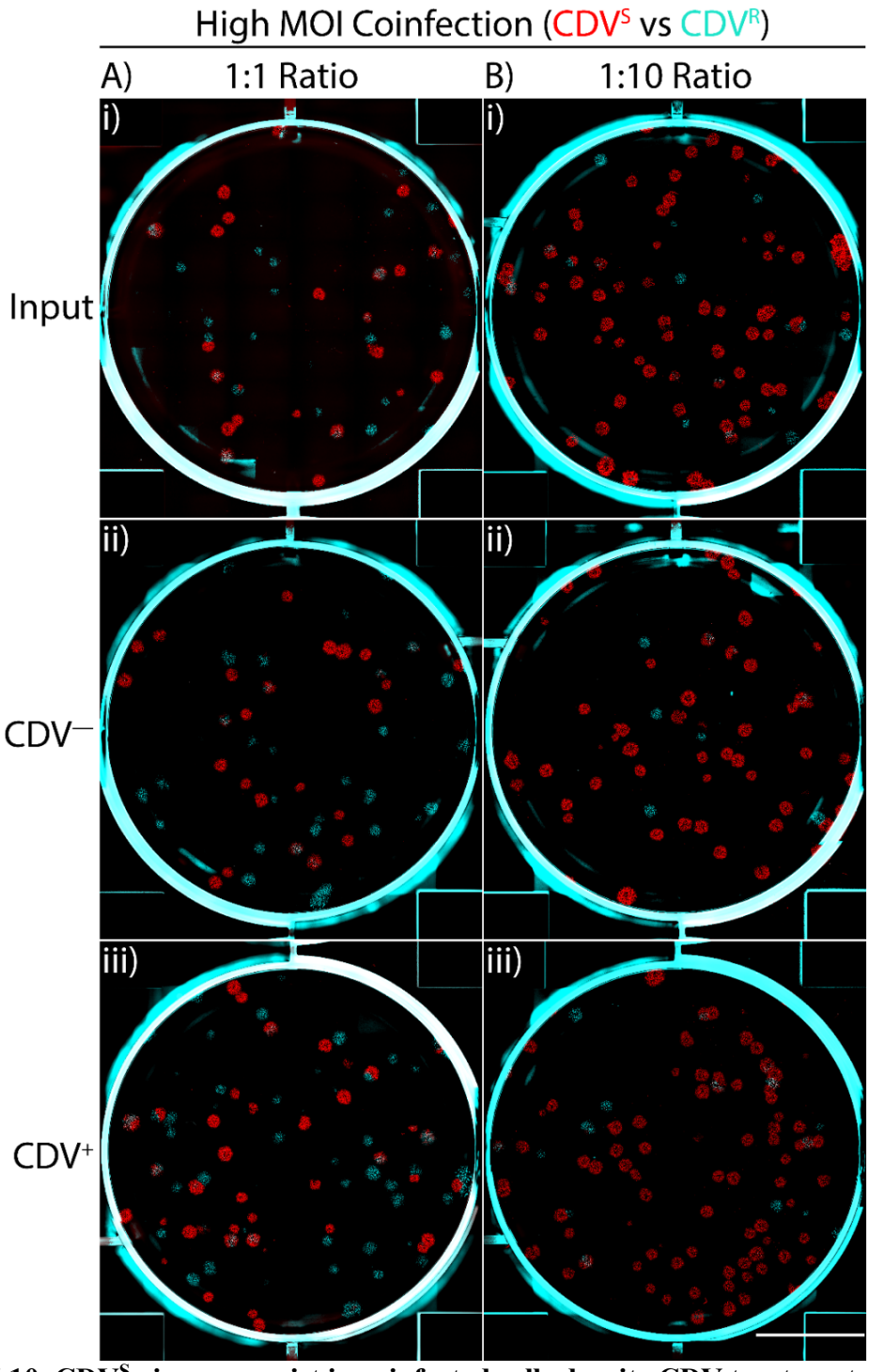

Figure 5.10. CDV^S viruses persist in coinfected cells despite CDV treatment. The input and progeny from a coinfection in the absence (CDV^{-}) or presence (CDV^{+}) of selective pressure were analyzed. Each sample was plated on BSC-40 cells without CDV to capture the frequency of CDV^R (cyan) and CDV^S (red) viruses in the population. Plaque formation proceeded for 48 hours before wells were imaged using a Biotek Cytation at 1.25X magnification. Representative wells from three independent biological experiments are shown. Scale bar = 1cm.

Measuring the numbers of different plaque types showed that before the coinfection, the frequency of CDV^R and CDV^S viruses were 55% and 45 % respectively, which was very close to the desired 1:1 ratio (**Figure 5.11A**). When the viruses were coinfected in the absence of CDV at a 1:1 ratio and the progeny phenotyped on untreated BSC-40 monolayers, the frequency of CDV^R viruses increased from 55% to 61%. This could also be represented as a 1.16-fold increase in the frequency of CDV^R viruses, reflecting random drift as there was no selective pressure from the drug (**Figure 5.11B**). When there was CDV present during the coinfection, the frequency of CDV^R viruses increased from 55% to 66% (**Figure 5.11A**). The frequency of CDV^R viruses increased 1.22-fold, which was not significantly different than the random drift observed after replicating in the absence of selection from CDV (**Figure 5.11B)**. Analyzing the frequency of the CDV^R virus in the progeny showed that in the absence or presence of CDV, there was a significant increase in the proportion of progeny that were CDV^R (**Figure 5.11A**). These observations suggested that whatever the reason for the small change in the composition of the population was not linked to drug treatment. Rather surprisingly, CDV^R mutants seemed to lose any competitive advantage over CDV^S wildtype viruses under conditions where drug selection pressure might favour CDV^R growth. The effect seen at a 1:1 ratio was somewhat enhanced when the CDV^R-to-CDV^S ratio was 1:10. At input, the frequencies of CDV^R and CDV^S viruses were 14.0% and 86.0%, respectively (**Figure 5.11C**). The frequency of CDV^R viruses among the progeny from untreated cells barely increased to 14.8% and up to 19.1% in treated cells, or a 1.07-fold and 1.38-fold increase. However, these numbers were not statistically different from each other (**Figure 5.11D**). This result illustrates the challenge a new virus – with a potential selective advantage – faces attempting to outgrow an overwhelming number of wildtype competitors.

5.2.4. Selection for CDV^R mutants requires that CDV^R and CDV^S viruses replicate in different cells

As an additional control, I reduced the MOI to 0.02, which corresponds to a 0.04% probability of cells receiving two infectious particles. This experiment modeled a situation in which wildtype and mutant viruses were replicating in complete isolation.

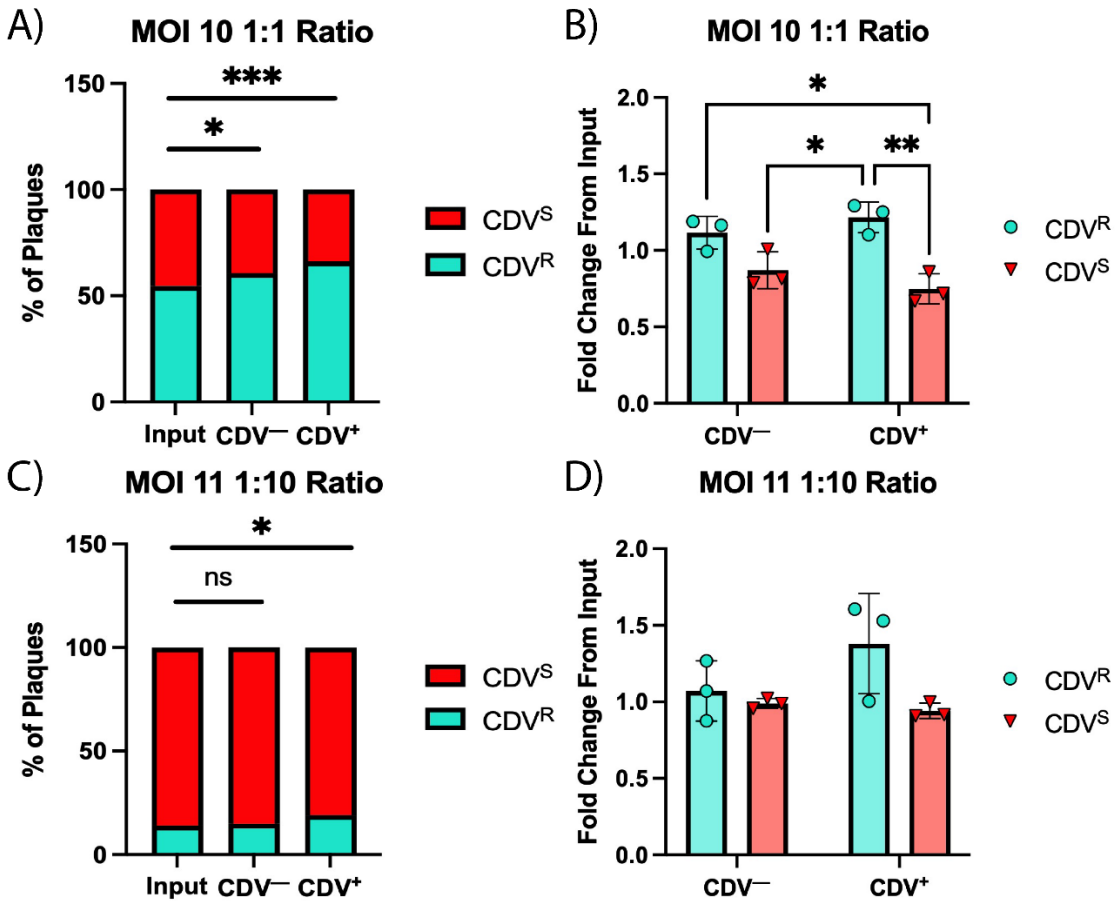

Figure 5.11. CDV^S viruses prevent the outgrowth of CDV^R mutants from coinfected cells. A & C) The mean percentage of CDV^S and CDV^R plaques was quantified by plating samples on BSC-40 cells in the absence of CDV and imaging fluorescent plaques with a BioTek Cytation (Agilent). Data were analyzed using a two-way ANOVA with Dunnett's multiple comparisons between the progeny from untreated or treated cells and the Input. Values are the mean of three independent biological experiments. B & D) The fold change from input was calculated for mutant and wildtype viruses, plotted in GraphPad Prism, and analyzed using a two-way ANOVA with Tukey's multiple comparisons. Values are the mean of three independent biological experiments ± standard deviation.

Again, "CDV$^-$" are progeny from coinfections without selection from CDV, whereas "CDV$^+$" are progeny from coinfections with 330μM CDV. The mean titer of the input was below 10^4 PFU/mL, indicating a sufficiently low MOI to reduce the probability of coinfections to a practically negligible amount (**Figure 5.12**). When I replated the progeny, there was a striking loss of red (CDV^S) plaques if the virus replicated in cells treated with CDV (**Figure 5.13**).

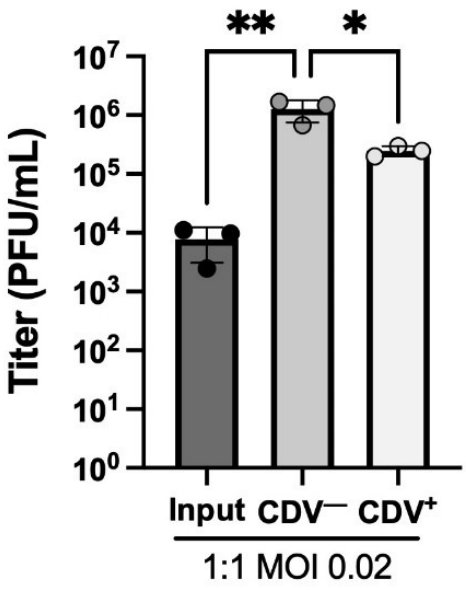

Figure 5.12. Titration data for a low-MOI competition experiment. The input samples from the coinfection and output samples were titrated on BSC-40s. The data are plotted as the mean of three biological replicates ± standard deviation. The data were analyzed in GraphPad Prism with one-way ANOVA with Tukey's multiple comparisons.

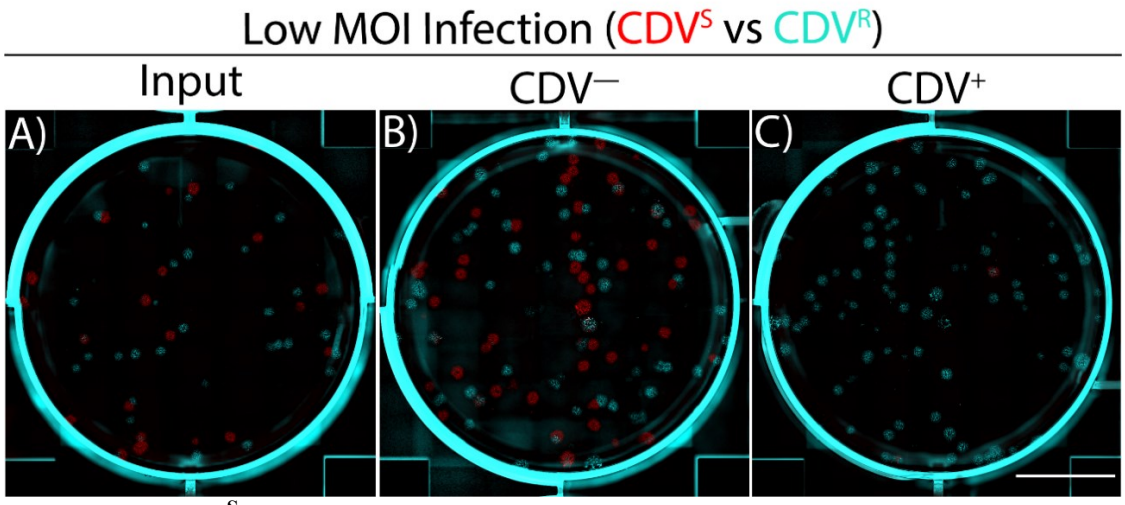

Figure 5.13. CDV^S viruses do not survive selection from CDV when coinfection is rare. The input and progeny from a coinfection in the absence (CDV$^-$) or presence (CDV$^+$) of selective pressure were analyzed. Each sample was plated on BSC-40 cells without CDV to capture the frequency of CDV^R (cyan) and CDV^S (red) viruses in the population. Plaque formation proceeded for 48 hours before wells were imaged using a Biotek Cytation at 1.25X magnification. Representative wells from three independent biological experiments are shown. Red plaques = wildtypes; Cyan plaques = mutants. Scale bar = 1cm

Plaque counts showed that the frequency of CDV^S viruses in the population started at 31% and significantly decreased to just 3.3% after culturing the mix of viruses with CDV (**Figure 5.14**). The frequency of CDV^R viruses in the "Input" was 69% and after being cultured in cells without CDV treatment, the frequency drifted to 54% after (**Figure 5.14A**). Conversely, the CDV^R viruses represented >96% of the viruses in the progeny recovered from cells treated with CDV. The 1.4-fold increase in the proportion of CDV^R mutants from CDV-treated cells was significantly higher than the 0.8-fold decrease observed in the progeny from untreated cells (**Figure 5.14B**).

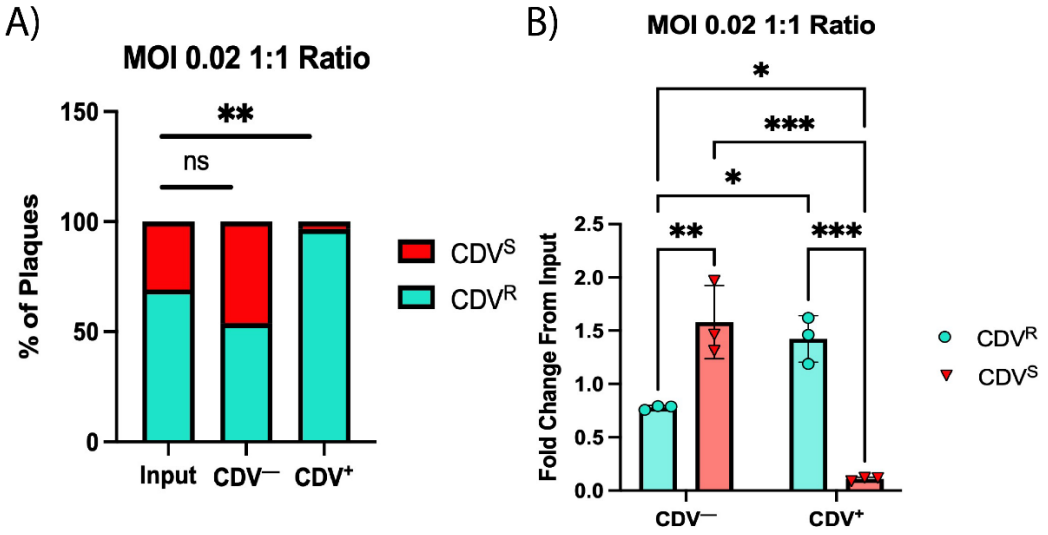

Figure 5.14. Mutant viruses expand in a low MOI infection model. A) The mean percentage of wildtype and mutant plaques was quantified using a Biotek Cytation. The data were analyzed using a two-way ANOVA with Dunnett's multiple comparisons between the progeny from untreated or treated cells and the Input. Values are the mean of three independent biological experiments ± standard deviation. B) The fold change from input was calculated for mutant and wildtype viruses, plotted in GraphPad Prism, and analyzed using a two-way ANOVA with Tukey's multiple comparisons. Values are the mean of three independent biological experiments ± standard deviation.

5.3. Conclusions

These experiments showed that the segregation of coinfecting VACV particles into separate virus factories does not create an environment where viruses encoding advantageous mutations can always "selfishly" benefit from such mutations. In other words, it disproved the hypothesis that factories might help create an environment that would permit intracellular competition between coinfecting viruses bearing different *E9L*

alleles. The clearest illustration of this was shown using live-cell imaging, where we observed that in CDV-treated cells, coinfecting CDV^R and CDV^S viruses displayed uniform growth of factories in a manner dependent on the proportion of CDV^S virus present (**Figure 5.5**). This suggested that CDV^S polymerases were interfering with the outgrowth of the CDV^R mutant from coinfected cells. Conversely, the CDV^R polymerase rescued the CDV^S virus and allowed the wildtype virus to survive the selective pressure from CDV. FISH experiments confirmed that, despite CDV treatment, there is no difference between the factories formed by VACV strains VDG1.3 and WR in coinfected cells (**Figures 5.6 & 5.7**). To further investigate how these intracellular interactions influenced the mixture of viruses found in the resulting population, I performed coinfection experiments to examine how the proportion of viruses changed with or without drug treatment. Coinfection prevented the selection for CDV^R viruses, as the frequency of mutant viruses did not change when a mix of CDV^S and CDV^R viruses were cultured in the presence of CDV (**Figure 5.11**). However, when the infection was conducted at a low MOI, significantly more CDV^R virus was recovered from cells relative to CDV^S viruses (**Figure 5.14**).

Collectively, the experiments presented in this chapter suggest a model for the evolution of mutant poxviruses that is highly dependent on maintaining single infections (**Figure 5.15**). In coinfected cells, the CDV^R and CDV^S polymerases will presumably mix throughout the cytoplasm, which in the experimental setup used here would support replication of both wildtype and mutant viruses in the presence of CDV (**Figure 5.15A**). Thus, what goes into the cell is what will come out of the cell, meaning the less fit virus survives the selection because of coinfecting CDV^R viruses providing the functional polymerase. However, when transmission proceeds through single particle infections, the CDV^S viruses cannot parasitize the fitness advantage of drug resistance (**Figure 5.15B**). This would create the purifying selection necessary that will eliminate CDV^S viruses while allowing CDV^R viruses to begin expanding. This model will be discussed in detail in the next chapter.

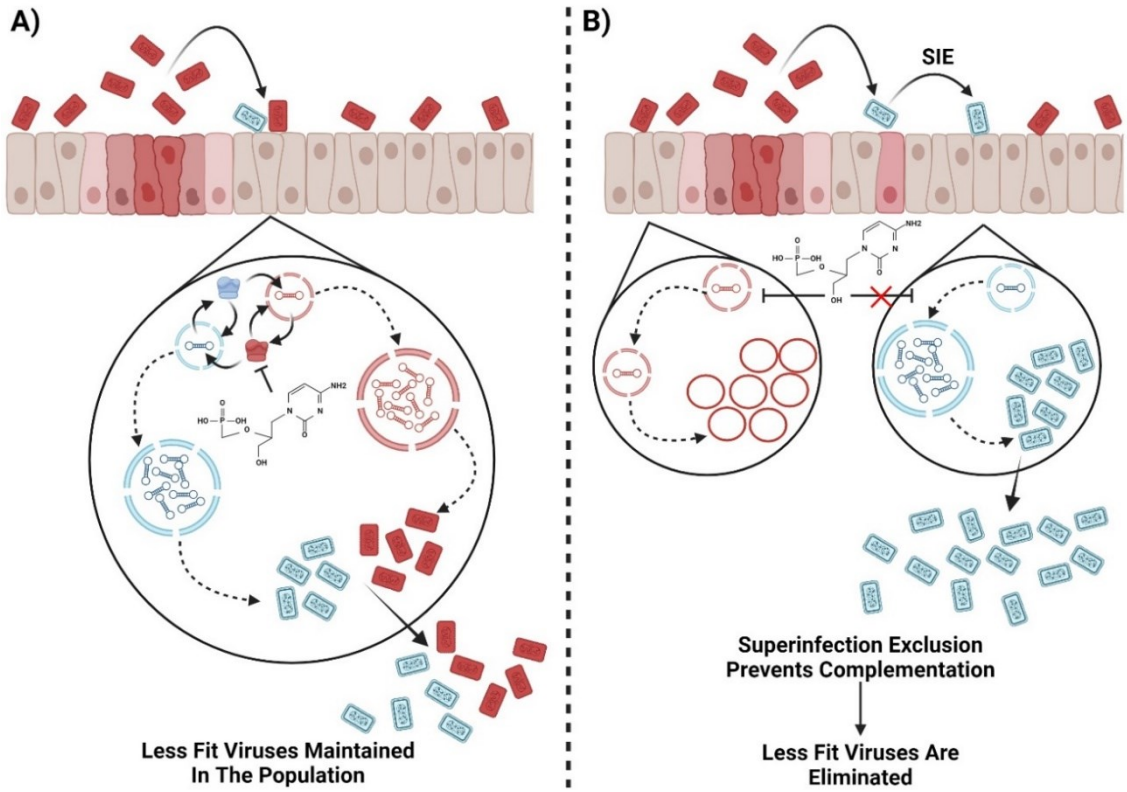

Figure 5.15. Selection for drug-resistant mutants requires single infections. A) Coinfection allows wildtype viruses (red) to receive the mutant polymerase (blue), allowing both factories to expand and an equivalent number of progeny to assemble. Polymerases complementing allows the less fit virus to survive and decreases fitness in the population given the selective pressure in the environment. B) A mechanism to maintain single infections such as superinfection exclusion ensures that wildtypes and mutants replicate in isolation. Mutant viruses cannot support the replication of wildtype viruses. This creates purifying selection that eliminates wildtype viruses. This model provides a mechanism that explains how drug resistance can rapidly expand in a population while also advancing the general fitness of the population.

Chapter 6: Discussion and Future Directions

6.1. Inserting cro-EGFP or cro-mKate2 into *J2R* does not impact fitness but may sensitize the virus to CDV

I successfully generated viruses expressing cro-EGFP or cro-mKate2 from a synthetic early/late promoter and showed that expression of the recombinant protein did not reduce fitness (**Figures 3.3 & 3.4**). Previous experiments using a VACV expressing mCherry-cro showed that mCherry-cro reduced plaque size and reduced the yield of viruses in a single-step growth curve (120). A possible explanation for this difference is that EGFP and mKate2 do not form higher order structures, whereas mCherry can form dimers (142). If the cro-FP recombinant proteins form dimers, the proteins may form more stable aggregates on the DNA, which could impede DNA replication and encapsidation (54, 56, 143, 144). Such aggregates of fluorescent protein would also coat incoming genomes during early stages of infection, possibly impeding entry, early gene expression, and DNA replication. The inability of EGFP and mKate2 to form dimers could allow easier dissociation of the proteins from the DNA during crucial viral processes.

The viruses expressing cro-EGFP or cro-mKate2 seemed to be more sensitive to CDV than the parental strains as viruses expressing cro-EGFP or cro-mKate2 showed decreased EC_{50} values for CDV compared to the parental strains (**Figure 3.5**). One explanation for this is that by choosing *J2R* as the insertion site, the recombinant viruses no longer express full-length J2. Loss of J2 renders the virus partially dependent on cellular pools of dNTPs for DNA replication (145). A previous study showed that relative to cells infected with wildtype viruses, cells infected with J2-deficient viruses have lower concentrations of dTTP and dCTP (146). J2 is involved in dTMP salvage from thymidine, so losing J2 decreases the amount of dTMP and subsequently dTTP in the cell (145). To compensate, the virus must rely on host thymidylate synthetase for conversion of dUMP into dTMP (145). The dUMP needed for this activity could come from dCMP deaminase, which would deplete the cell of dCMP and subsequently dCTP (145). Because CDVpp is a dCTP analog and competes for binding in the active site of E9, it is possible that lower levels of dCTP would allow greater incorporation of CDV into replicating DNA. This

would sensitize the virus to drug treatment, therefore decreasing the EC_{50}. A virus expressing full-length J2 may avoid incorporation of CDV and overcome incorporated CDV by having higher levels of dCTP than recombinant viruses that do not express functional J2.

6.2. Cidofovir has a direct antiviral effect on DNA replication

The data presented in Chapter **4** showed that CDV inhibits DNA replication. CDV treatment significantly slowed the growth of wildtype, CDV-sensitive (CDV^S) virus factories (**Figures 4.3 & 4.4**). Conversely, there was no significant difference between the growth rate for the CDV-resistant (CDV^R) virus factories in the presence or absence of CDV (**Figures 4.5 & 4.6**). Experiments with fixed samples confirmed that CDV^S viruses make significantly smaller factories with less viral DNA than CDV^R viruses in cells treated with CDV (**Figures 4.8-4.10**). Lastly, EdU pulse labelling experiments provided further evidence that CDV directly inhibits DNA synthesis (**Figures 4.12 & 4.13**). These data contrast those published on the mechanism of action for CDV (137). A previous study concluded that CDV did not affect DNA replication; instead, the authors showed a failure to package genomes by electron microscopy (EM) and distortion of the DNA ultrastructure by atomic force microscopy. These experiments did not consider the slow conversion of CDV to CDVpp (138, 139), which could explain why the authors never found an antiviral effect on DNA replication.

Previous biochemical analysis found that CDV is a potent competitive inhibitor of E9 in primer extension experiments (102). The rate of synthesis significantly decreased after the n+1 position. Additionally, CDV also has a template-dependent effect on DNA replication (103). The biochemical findings agree with the findings from Chapter **4**, but my data do not rule out additional mechanisms of action for CDV. Structural analysis using nuclear magnetic resonance showed that CDV destabilized the DNA duplex around the CDV lesion (147). The authors suggested that – especially after the strands separate – the acyclic structure of CDV could prevent proper positioning of the 3′OH of the n+1 base. This could explain the direct effect on chain extension. Additionally, the overall instability of the duplex may cause perturbations in the structure of the genome, which could cause the previously described problems to encapsidation of the viral genome into

the immature virion (137). CDV may therefore have multiple mechanisms of action beyond merely competing at the active site. The added instability of duplex DNA suggests that even if a polymerase successfully incorporates CDV and continues synthesis, the resulting molecules may have a disrupted structure that disfavors transcription or encapsidation. The template-dependent effect of CDV further suggests that the structural perturbations to the duplex could have far-reaching effects in the viral lifecycle.

It would be interesting to look at what happens late in replication after CDV pretreatment. A particularly intriguing experiment would be to look at the ability of the RNA polymerase to synthesize mRNA across a CDV lesion. It is conceivable that transcription may stop at a CDV lesion, preventing late gene expression. Reverse transcription coupled with quantitative PCR using primers that amplify late genes can address this hypothesis. Additionally, quantitative Western blotting using primary antibodies targeting candidate late proteins would provide complimentary information about protein synthesis. It is possible that if CDV completely stopped the replication cycle at genome replication, then late genes would not be expressed and new virions would not assemble. Repeating the EM experiments from Jesus *et al.*, but using CDV pretreatment, may therefore show no viral membranes assembling around the factory, which would show that CDV targets the virus at an early stage before assembly and genome encapsidation.

6.3. The A314T/A684V substitutions in E9 increase the uptake of EdU

Surprisingly, viruses encoding the CDV^R VDG1.3 allele showed significantly higher uptake of EdU than CDV^S viruses, showing that drug resistance mutations impacted nucleotide selectivity (**Figures 4.12-4.14**). The A314T substitution is thought to enhance the transition from synthesis to excision, as a wildtype polymerase cannot perform recombination using substrates with CDV embedded at the 3′ end because the wildtype 3′-5′ exonuclease domain cannot remove the drug (102, 148). The A684V substitution occurs adjacent to the dNTP binding pocket and is thought to disfavour binding of CDV into the active site of the polymerase (147). This substitution causes a mutator phenotype in VACV, which further suggests the A684 residue is crucial to

selecting incoming nucleotides (111). Recently-published X-ray crystallography and cryo-EM studies provided high-resolution structures of the VACV and MPXV DNA polymerases (29, 67, 68). In the MPXV DNA polymerase F8, the analogous residue to E9 A684 is adjacent to multiple residues that contact the incoming dNTP. The A684V substitution may displace critical residues, in particular the π-electrons of Y554 that normally interact with the ribose of the incoming dNTP, and the many residues that bind the triphosphate moiety (68). Additional cryo-EM using the VDG1.3 polymerase could provide greater detail than speculating how A684V disrupts the nucleotide binding site.

Drug resistance mutations in *E9L* are known to induce changes in nucleotide selectivity and subsequently altered sensitivity to other antiviral compounds. A recent study using VACV found that CDV^R mutations in *E9L* induced hypersensitivity to multiple compounds (114). This is not unique to VACV, as studies with the human cytomegalovirus DNA polymerase found that CDV^R mutations sensitized the virus to acyclovir (149). CDV^R mutations in murine γ-herpesvirus 68 – a γ-herpesvirus related to the human herpesvirus 8 – also altered nucleotide selectivity (150). Given that CDV is an important drug for treating human cytomegalovirus and poxviruses, it will be interesting to further characterize the sensitivity profile of mutants to additional antivirals. Furthermore, aphidicolin resistance in VACV *E9L* also induces a mutator phenotype (151). Studies using herpes simplex virus 1 (152–154), herpes simplex virus 2 (155), and murine γ-herpesvirus 68 (150) also reported that aphidicolin resistance reduced the fidelity of the polymerase, likely by changing nucleotide selectivity. A yeast DNA polymerase isolated from cells after culturing in aphidicolin also demonstrated a mutator phenotype (156). Any disruption to the structure of the polymerase could alter nucleotide selectivity, so it is reasonable that this could be a common phenomenon among drug resistance mutations that map to a DNA polymerase gene.

These observations suggest a logical series of experiments to identify more antivirals targeting E9 and the mutant polymerase. Primer extension assays could identify changes in nucleotide selectivity with the CDV^R polymerase. This could then inform rational design of compounds with better uptake than CDV. Renal and hepatic toxicity limit the use of CDV or brincidofovir in patients (110). This limitation shows that there is a need for additional antiviral therapies for re-emerging poxviruses. As will be discussed,

the only other antiviral drug for treating *Orthopoxvirus* infections is tecovirimat, and drug resistance rapidly emerges after treatment (157, 158). Given how CDV has antiviral activity against multiple DNA viruses, broad-spectrum drugs that exploit nucleotide selectivity will be beneficial. Further identification of compounds will support pandemic preparedness.

6.4. Co-localization of cro-EGFP and cro-mKate2 during coinfections

I expected that cro-EGFP and cro-mKate2 would stay with the factory of genetic origin as previous reporter viruses expressing EGFP-cro and mCherry-cro showed that these constructs stayed inside the factory after synthesis (120). Other work from Katsafanas and Moss found that a virus encoded β-galactosidase localized to the virus factory despite the enzyme lacking a function relevant to factory biology (43). Additionally, cells coinfected with VACV expressing the core A5 tagged with YFP or CFP displayed exclusively YFP- or CFP-positive factories in the same cytoplasm. Conversely, my coinfection experiments using viruses expressing cro-EGFP and cro-mKate2 showed the two fluorophores colocalizing in virus factories (**Figures 5.1 & 5.2**). The differences between early and late replication can explain this discrepancy (**Figure 6.1**). Early in replication, the virion core extrudes transcripts into the cytoplasm (20, 21). Translation of the early transcripts occurs in polysome-rich aggregates that are distinct from the cores and subsequent virus factories (129, 130). Because an early/late promoter controlled expression of cro-EGFP and cro-mKate2, the transcripts likely followed this behavior and initiated translation in the cytoplasm. Electrostatic interactions would cause the cro-FP proteins to bind whichever genome was closest, meaning that the labeling was sequence-independent. Late gene expression seems to exclusively occur in the virus factory, so perhaps a late protein might get retained inside the factory after synthesis, consistent with the work from the Moss laboratory (43). By this stage in the viral lifecycle, the factory is well-established, translation initiation factors are re-localized into the factory, and membranes are wrapping the genomic DNA (41, 42). Thus, transcripts will stay close to the genome, and likely the encoded proteins will stay within the factory.

The cell biology of early replication may explain why cro-EGFP and cro-mKate2 colocalized, but it is still unclear why previous data showed uniformly EGFP- and

mCherry-positive factories. It is particularly unclear why an N-terminal cro fusion would cause such a different localization. I also included a flexible linker peptide when designing my constructs. Perhaps the affinity for DNA is reduced with this modification at the C-terminus of cro (see plasmid maps in Appendix). Steric hindrance near the DNA binding pocket of cro could weaken binding and allow more of the protein to diffuse away from DNA. Additionally, if mCherry-cro formed dimers as hypothesized, then it is possible that one mCherry-cro protein on a genome could enable cooperativity and enhance binding of additional mCherry-cro proteins. Another explanation is that the membranes surrounding the virus factory are much more permeable than we think. The membranes must be loose enough to allow the virosome to expand as DNA replication progresses. The factory membrane also deteriorates as infection progresses and assembling viruses cannibalize the membrane to form progeny virions (46–52). These factors point to a model in which the factory membrane is constantly distorting and becoming more permeable as infection progresses.

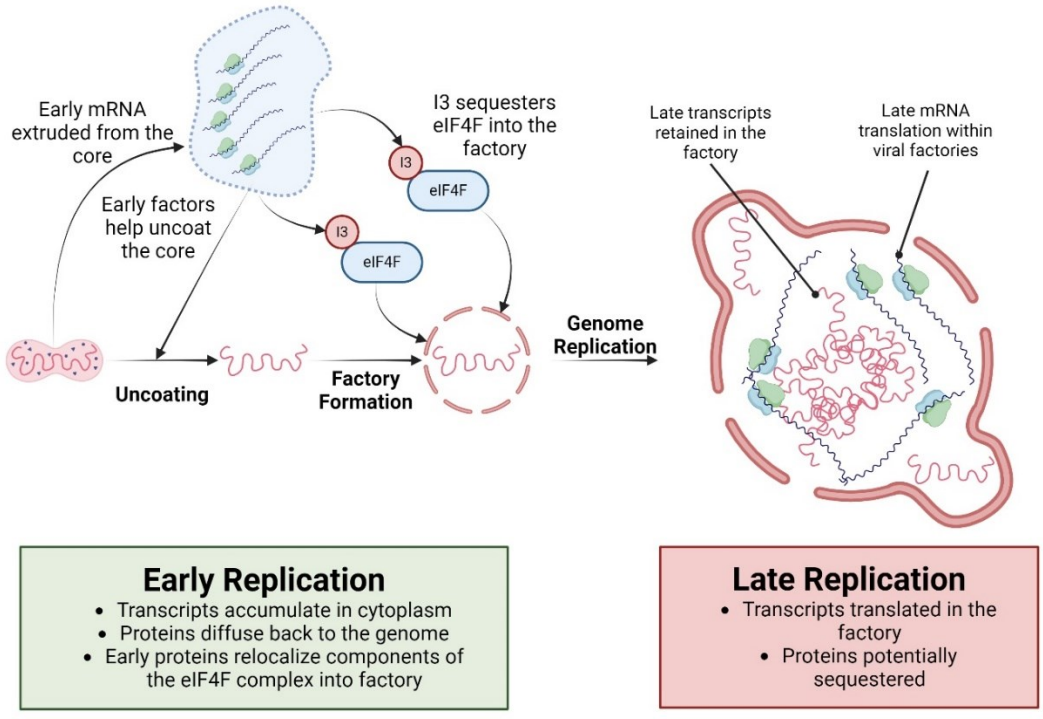

Figure 6.1. Localization of translation in the poxvirus lifecycle. The model is based on observations from microscopy studies tracking the translation initiation factors and viral mRNA (41–43, 129, 130).

6.5. Codominance between the DNA polymerases interferes with the outgrowth of CDV^R viruses at early stages of replication

Coinfection experiments showed that all the factories in coinfected cells grew at a uniform rate, suggesting that the polymerases were mixing between the factories (**Figures 5.4-5.7**). This phenomenon is not classical protein-protein complementation as used to map genes based on the results of high-MOI crosses (125). For VACV, complementation describes proteins encoded by different genes on different viruses acting *in trans* and allowing both mutants to replicate under nonpermissive conditions (**Figure 1.6**) (124, 125, 128). The results of the coinfection experiments suggest that the CDV^R virus provided a functional polymerase that could aid the replication of a coinfecting CDV^S virus (**Figures 5.10 & 5.11**). Because both alleles are in the *E9L* gene, this is not classical intergenic complementation, yet the result is that both viruses replicate. Codominance between the *E9L* alleles best describes this phenomenon as increasing the copy number of the CDV^S polymerase caused all the coinfecting viruses to replicate at a significantly slower rate than when CDV^S and CDV^R viruses infected a cell at a 1:1 ratio (**Figure 5.5**). Therefore, the relative proportion of each virus will affect the collective fitness of the coinfecting viruses when CDV is present.

Because E9 is an early DNA binding protein, it would likely behave the same as the cro-FP constructs discussed in Chapter **6.4**. Diffusion and electrostatic interactions will pull E9 back to whichever genome is closest. Additionally, the interaction between E9 and the D4+A20 processivity factor would further strengthen the binding to that genome and prevent E9 from leaving a factory once it starts synthesis (29, 67, 68). Thus, a CDV^S virus can parasitize the CDV^R E9 during a coinfection. My data do not directly show that the polymerases are randomly distributed between CDV^R and CDV^S factories, and this represents an interesting future direction. With sophisticated reactivation techniques, it is possible to rescue viruses without the use of selectable markers (28, 159). Unique epitope tags at the N-terminus of the CDV^R and CDV^S polymerases combined with FISH could test the hypothesis that E9 proteins randomly distribute themselves between coinfecting viruses. This reactivation method could also be used to generate viruses for live imaging of proteins as they are being translated, an experiment that

requires unique N-terminal epitope tags (160). These experiments would fully elucidate the underlying mechanism causing codominance between CDV^S and CDV^R viruses.

6.6. Distinctions between early and late replication suggest the possibility of competition late in an infection

As discussed in Chapter **6.4**, factory formation sequesters components of the eIF4F complex and RNA binding proteins. Katsafanas & Moss showed that eIF4G and eIF4E localize to the virus factory at late stages of replication, and close examination of 3D reconstructions of their images showed these proteins fully enclosed in the factory (43). Work from the Walsh laboratory showed that I3 binds to eIF4G, helping to recruit the eIF4F complex to the virus factory (41, 42) (**Figure 6.1**). The differences between early and late transcripts suggest that there is the possibility for competition late during infection, as late proteins are more likely to stay inside the factory. However, it is unclear whether the disruption of the factory membrane during assembly (46–48, 50–52, 57) would increase the permeability of the factory and allow proteins to diffuse into the cytoplasm. Additionally, factory collisions can permit mixing of proteins at a late stage of infection, which would prevent competition (6, 120, 121). It is worth revisiting the work from Katsafanas & Moss using viruses expressing A5-YFP and A5-CFP in coinfection to see if the proteins ever colocalize (43). These experiments used fixed samples, so repeating the experiments using live-cell imaging may provide greater insight. An additional way to examine this would be to repeat the competition studies using a mutation in a late gene instead of an early gene. The candidate gene would need to be localized to the viral factory. The telomere binding proteins I1 and I6 are interesting candidates for this study as they play an essential role in genome encapsidation (54, 56, 143). Viruses lacking I1 or I6 expression do not assemble mature particles; if proteins are truly sequestered when synthesized late, then one would expect a strong elimination of I1- or I6-deficient mutants from a coinfection. Additionally, one could use a tecovirimat resistance allele in the *F13L* gene as a marker (161). As will be discussed, selection for tecovirimat resistance occurs rapidly. Perhaps competition at a late stage in replication favours this rapid outgrowth of tecovirimat-resistant viruses.

6.7. Selection for CDV-resistant mutants requires infection by a single virus

The data from chapter **5** showed that in high-MOI coinfections (MOI 10 or 11), the CDV^R mutant lacked a competitive growth advantage over CDV^S wildtypes (**Figures 5.10 & 5.11**). Conversely, at a low MOI (MOI 0.02), there was a precipitous loss of CDV^S virus (**Figures 5.13 & 5.14**). This showed that selection for CDV^R required that CDV^R and CDV^S viruses enter separate cells. The observations that cro-EGFP and cro-mKate2 colocalized during coinfections and factories grew at uniform rates suggested that CDV^R and CDV^S are codominant traits. Thus, CDV^S viruses prevented the CDV^R mutants from gaining a selective advantage, which in turn prevented the outgrowth of the CDV^R mutants in high-MOI coinfections. This may explain why previous attempts to isolate CDV^R VACV required extensive passage of the virus (>40 passages) to obtain a clone, as the overwhelming presence of CDV^S viruses essentially made CDV^S the dominant allele in the population (111).

While it is possible to artificially manipulate the conditions *in vitro* to promote coinfection, it is unclear how often viruses coinfect cells *in vivo*. However, there are some hints from previous studies. Early studies showed that poxvirus-infected cells became refractory to secondary infections, a phenomenon called superinfection exclusion (SIE) (162). Later, Doceul *et al.* identified two early proteins A33 and A36 that mediate SIE in poxvirus-infected cells (163). A33 and A36 catalyze actin tail formation, working together to "catch" incoming particles and assemble actin tails that "push" the surface-bound particles away from the cell. Initially, the authors proposed SIE as a mechanism that facilitates rapid spread of virions throughout a 2D cell culture (163). This is not an accurate representation of the complexity that exists in a tissue, and thus any data from SIE experiments require careful interpretation. However, my data would also suggest that – at least in cell culture conditions – SIE may be an important mechanism to maintain viral fitness. Laliberte & Moss also suggested this idea in their paper, using the analogy of the most fit spermatozoa winning the race to fertilize an ovum (164). Studies with RNA viruses also described an evolutionary impact to SIE. The neuraminidase protein of influenza virus can prevent secondary infection, which affects the generation of reassortant viruses that drive genetic diversity (165). Boussier *et al.* suggested that SIE

during chikungunya virus infection prevents the accumulation of defective particles (166). Beyond eukaryotic viruses, Biggs *et al.* described a similar evolutionary interpretation to SIE from bacteriophage coinfections (167). Thus, there is a growing body of literature suggesting that SIE may affect population fitness by preventing defective particles from accumulating.

One limitation to this model is that it is unclear what SIE accomplishes *in vivo*. As mentioned, studies with SIE in poxviruses have only examined 2D cell cultures. Exactly how and why SIE evolved during the natural circulation of poxviruses is unclear, though it is important to note that populations cannot anticipate selective pressures, only respond to them. Thus, it would be inappropriate to assert that SIE evolved with the explicit purpose of preventing complementation between coinfecting viruses. However, a logical advantage to SIE is that it ensures the second virus entering the cell and trying to initiate its own replication does not interfere with the primary infection. One consequence of this would be that defective particles could not enter cells already infected with replication-competent virus. However, it is unclear how effective SIE is in maintaining single infections. Experiments with SIE described a time-dependent effect as cells become less susceptible to secondary infection the longer the primary infection lasts (162, 164). Thus, it is conceivable that a virus could enter a cell shortly after another and still replicate. For VACV, this would presumably depend on how fast the virus enters the cell and begins gene expression *in vivo*, something that is harder to quantify than in an *in vitro* experiment. However, one could use viruses deficient of A33 and A36 in serial passage experiments and measure the particle-to-PFU ratio using flow virometry, which uses small particle flow cytometry to measure the number of infectious particles relative to an experimentally-determined number of PFU (28). One could also use samples from different passages in animal challenge experiments. This could reveal if SIE maintains fitness and if this phenomenon affects virulence *in vivo*. These experiments would further our understanding of the molecular mechanisms driving poxvirus evolution.

6.8. Rapid selection for advantageous traits is common in poxvirus evolution

DNA virus evolution is generally thought to be a slow process compared to RNA viruses. However, this paradigm does not fit the data obtained from poxvirus evolution studies. At the molecular level, poxviruses can rapidly adapt to selection from antiviral drugs. Experiments with rifampicin resistance in the *D13L* gene reported rapid isolation of drug-resistant plaques at low MOI (MOI 1) after a single passage (168). An alternative mutation that duplicated part of the *A17L* gene also confers resistance to rifampicin (44). Like the *D13L* mutation, the authors rapidly isolated viruses with the *A17L* duplication after one passage at an MOI of 1. This duplication was also stable under rifampicin selection but could contract in the absence of selection. These experiments agree with the data from coinfection studies at low MOI for CDV^R (**Figure 5.15**). Previous attempts to isolate CDV^R viruses required >40 passages to isolate clones, a striking contrast from what is observed in other studies (111). Andrei *et al.* did not report the MOI used, though given what I observed in high-MOI coinfections (**Figures 5.10 & 5.11**), the extensive passaging suggests the authors used a high MOI. Interestingly, selection for *F13L* mutations with tecovirimat can occur at high MOI, as Yang *et al.* plated 10^7 PFU and isolated mutants after a single passage (169). As mentioned in Chapter **6.6**, this might reflect differences in late gene expression compared to early gene expression. However, a later study required >14 passages to isolate tecovirimat-resistant viruses (161). It is unfortunately very difficult to compare between various studies without consistent methodology. Data from clinical administration of tecovirimat showed that tecovirimat treatment rapidly generates drug-resistant viruses with mutations in the *F13L* gene, further suggesting that tecovirimat-resistant viruses may also rapidly outcompete wildtypes as in other drug resistance studies (157, 158, 170). Unfortunately, there is limited clinical use of CDV or BDV, so it is unclear how fast the selection takes place *in vivo*. The original studies with the CDV^R strain VDG1.3 showed that the virus is attenuated in mice, making it difficult to select for the trait *in vivo* (111). Nevertheless, my data agree with studies using other antiviral compounds showing rapid adaptation to the selection. Intriguingly, all these resistance mutations map to late genes except for CDV^R. It would be very interesting to perform systematic experiments to determine if the

selection for late gene mutations differs from early gene mutations. This could further highlight the differences between the early and late stages of virus replication discussed in **6.4** and **6.6**.

Additional evidence for rapid adaptation comes from experiments studying PKR antagonists. Brennan *et al.* wrote an extensive review of these strategies; I will highlight some of the data pertinent to the experiments I conducted (122). One of the most striking observations from experimental evolution studies is gene duplication in the protein kinase R antagonist K3 (171). K3 sequesters the PKR target eIF2α, and K3 proteins from different poxviruses reflect co-evolution within a narrow host range (172). A virus with a mismatched K3 isoform can rapidly adapt to a new host through duplication of the *K3L* gene, which arose after six passages at low MOI (MOI 0.1) (171). The duplication is stable under selective pressure but recombination can eliminate the second copy of the gene if the virus returns to its normal host species. Studies using a virus lacking E3 and K3 but expressing a rhesus cytomegalovirus PKR inhibitor RhTRS1 showed the same phenomenon, with rapid duplication of the PKR antagonist acting as a foothold in a new host (173, 174). Four passages at low MOI (MOI 0.1) were sufficient to isolate this duplication. The presence of two copies of K3 or RhTRS1 could generate viruses with wildtype and mutated alleles in these genes that generate PKR antagonists with distinct amino acid sequences. This is a much more complicated scenario than the selection for a drug-resistant virus, and a coinfection between the adapted VACV and wildtype VACV would not reflect the same scenario as in my studies. Despite this difference, these experiments show that rapid adaptation in poxvirus populations is an important evolutionary mechanism, though the precise mode of selection may differ depending on the nature of the adaptation.

The value of these molecular evolution studies is that they contribute to our understanding of how poxvirus populations adapt to selection. My data contribute to a broader narrative in poxvirus biology suggesting that adaptation is a fast process relying on multiple molecular mechanisms. Generally, large DNA viruses are thought to evolve slowly (122). The substitution rates for herpesviruses are often multiple orders of magnitude lower than those of RNA viruses. Conversely, poxviruses display relatively high substitution rates. The extensive circulation of myxoma virus (MYXV) in the wild

after its introduction in 1950 has allowed reliable measurements of the substitution rates in different populations. These studies consistently report MYXV substitution rates close to $1x10^{-5}$ substitutions/site/year, which is multiple orders of magnitude higher than the substitution rate from herpesviruses (175–179). This calculation was consistent in MYXV populations in Australia, Europe, and North America. Strikingly, the measurements from MYXV agree with observations from variola virus isolates dating from 1946-1977 (180). High mutation rates and the plethora of molecular strategies for adaptation allow poxviruses to rapidly evolve at rates that approach those of RNA viruses. My model of SIE maintaining fitness (**Figure 5.15**) would ensure that any defective particles resulting from high mutation rates would not replicate. An additional consequence would be that SIE could facilitate rapid adaptation to selective pressure and the outgrowth of rare, advantageous traits like drug resistance.

6.9. Concluding Remarks

In conclusion, my data showed that with the right conditions, poxviruses can rapidly adapt to selective pressure, and that this can enhance the selection for advantageous traits like drug resistance. In coinfection studies, the interference from CDV^S viruses prevented the outgrowth of CDV^R mutants. The cell biology of poxvirus replication allows the exchange of proteins between coinfecting viruses, especially at early stages preceding factory formation. This results in codominance between CDV^S and CDV^R viruses, which in the population, will allow the less fit, CDV^S virus, to survive CDV selection. With a low MOI, there was rapid expansion of the CDV^R viruses and elimination of CDV^S wildtypes. These data showed that CDV^R adaptation can occur rapidly when only a single particle enters a given cell. This observation suggested that SIE could provide an evolutionary benefit by ensuring that replication-competent viruses cannot rescue the replication of defective particles (164). These studies agreed with other molecular evolution studies that showed rapid adaptation of the virus to new selective pressures. Given the high rate of mutation in poxviruses, the broader body of literature suggests that poxvirus evolution is far more dynamic than previously described. Multiple molecular mechanisms for adaptation allow poxvirus populations to maintain high fitness despite strong selective pressures like antiviral drug treatment or host innate immunity.

Bibliography

1. 2003. Update: Multistate Outbreak of Monkeypox --- Illinois, Indiana, Kansas, Missouri, Ohio, and Wisconsin, 2003. Morbidity and Mortality Weekly Report 52:561–564.
2. Thornhill JP, Barkati S, Walmsley S, Rockstroh J, Antinori A, Harrison LB, Palich R, Nori A, Reeves I, Habibi MS, Apea V, Boesecke C, Vandekerckhove L, Yakubovsky M, Sendagorta E, Blanco JL, Florence E, Moschese D, Maltez FM, Goorhuis A, Pourcher V, Migaud P, Noe S, Pintado C, Maggi F, Hansen A-BE, Hoffmann C, Lezama JI, Mussini C, Cattelan A, Makofane K, Tan D, Nozza S, Nemeth J, Klein MB, Orkin CM. 2022. Monkeypox Virus Infection in Humans across 16 Countries — April–June 2022. New England Journal of Medicine 387:679–691.
3. Gigante CM, Korber B, Seabolt MH, Wilkins K, Davidson W, Rao AK, Zhao H, Smith TG, Hughes CM, Minhaj F, Waltenburg MA, Theiler J, Smole S, Gallagher GR, Blythe D, Myers R, Schulte J, Stringer J, Lee P, Mendoza RM, Griffin-Thomas LTA, Crain J, Murray J, Atkinson A, Gonzalez AH, Nash J, Batra D, Damon I, McQuiston J, Hutson CL, McCollum AM, Li Y. 2022. Multiple lineages of monkeypox virus detected in the United States, 2021–2022. Science (1979) 378:560–565.
4. Vaughan AM, Cenciarelli O, Colombe S, de Sousa LA, Fischer N, Gossner CM, Pires J, Scardina G, Aspelund G, Avercenko M, Bengtsson S, Blomquist P, Caraglia A, Chazelle E, Cohen O, Diaz A, Dillon C, Dontsenko I, Kotkavaara K, Fafangel M, Ferraro F, Firth R, Fonager J, Frank C, Carrasco MG, Gkolfinopoulou K, Grenersen MP, Guzmán Herrador BR, Henczkó J, Hoornenborg E, Igoe D, Ilić M, Jansen K, Janță DG, Johansen TB, Kasradze A, Koch A, Kyncl J, Martins JV, McAuley A, Mellou K, Molnár Z, Mor Z, Mossong J, Novacek A, Orlikova H, Novosel IP, Rossi MK, Sadkowska-Todys M, Sawyer C, Schmid D, Sîrbu A, Sondén K, Tarantola A, Tavares M, Thordardottir M, Učakar V, Van Ewijk C, Varjas J, Vergison A, Vivancos R, Zakrzewska K, Pebody R, Haussig JM. 2022. A large multi-country outbreak of monkeypox across 41 countries in the WHO European Region, 7 March to 23 August 2022. Eurosurveillance 27.
5. Mauldin MR, McCollum AM, Nakazawa YJ, Mandra A, Whitehouse ER, Davidson W, Zhao H, Gao J, Li Y, Doty J, Yinka-Ogunleye A, Akinpelu A, Aruna O, Naidoo D, Lewandowski K, Afrough B, Graham V, Aarons E, Hewson R, Vipond R, Dunning J, Chand M, Brown C, Cohen-Gihon I, Erez N, Shifman O, Israeli O, Sharon M, Schwartz E, Beth-Din A, Zvi A, Mak TM, Ng YK, Cui L, Lin RTP, Olson VA, Brooks T, Paran N, Ihekweazu C, Reynolds MG. 2022. Exportation of Monkeypox Virus From the African Continent. Journal of Infectious Diseases 225:1367–1376.
6. Kieser Q, Noyce RS, Shenouda M, James Lin YC, Evans DH. 2020. Cytoplasmic factories, virus assembly, and DNA replication kinetics collectively constrain the formation of poxvirus recombinants. PLoS One 15:e0228028.

7. Chiu W-L, Lin C-L, Yang M-H, Tzou D-LM, Chang W. 2007. Vaccinia Virus 4c (A26L) Protein on Intracellular Mature Virus Binds to the Extracellular Cellular Matrix Laminin. J Virol 81:2149–2157.
8. Chung C-S, Hsiao J-C, Chang Y-S, Chang W. 1998. A27L Protein Mediates Vaccinia Virus Interaction with Cell Surface Heparan Sulfate. J Virol 72:1577–1585.
9. Lin C-L, Chung C-S, Heine HG, Chang W. 2000. Vaccinia Virus Envelope H3L Protein Binds to Cell Surface Heparan Sulfate and Is Important for Intracellular Mature Virion Morphogenesis and Virus Infection In Vitro and In Vivo. J Virol 74:3353–3365.
10. Hsiao J-C, Chung C-S, Chang W. 1999. Vaccinia Virus Envelope D8L Protein Binds to Cell Surface Chondroitin Sulfate and Mediates the Adsorption of Intracellular Mature Virions to Cells. J Virol 73:8750–8761.
11. Izmailyan R, Hsao J-C, Chung C-S, Chen C-H, Hsu PW-C, Liao C-L, Chang W. 2012. Integrin β1 Mediates Vaccinia Virus Entry through Activation of PI3K/Akt Signaling. J Virol 86:6677–6687.
12. Gray RDM, Albrecht D, Beerli C, Huttunen M, Cohen GH, White IJ, Burden JJ, Henriques R, Mercer J. 2019. Nanoscale polarization of the entry fusion complex of vaccinia virus drives efficient fusion. Nat Microbiol 4:1636–1644.
13. De Magalhães JC, Andrade AA, Silva PNG, Sousa LP, Ropert C, Ferreira PCP, Kroon EG, Gazzinelli RT, Bonjardim CA. 2001. A mitogenic signal triggered at an early stage of vaccinia virus infection. Implication of MEK/ERK and protein kinase A in virus multiplication. J Biol Chem 276:38353–38360.
14. Locker JK, Kuehn A, Schleich S, Rutter G, Hohenberg H, Wepf R, Griffiths G. 2000. Entry of the Two Infectious Forms of Vaccinia Virus at the Plasma Membane Is Signaling-Dependent for the IMV but Not the EEV. Mol Biol Cell 11:2497–2511.
15. Mercer J, Helenius A. 2008. Vaccinia virus uses macropinocytosis and apoptotic mimicry to enter host cells. Science (1979) 320:531–535.
16. Schmidt FI, Bleck CKE, Helenius A, Mercer J. 2011. Vaccinia extracellular virions enter cells by macropinocytosis and acid-activated membrane rupture. EMBO Journal 30:3647–3661.
17. Mercer J, Knébel S, Schmidt FI, Crouse J, Burkard C, Helenius A. 2010. Vaccinia virus strains use distinct forms of macropinocytosis for host-cell entry. Proc Natl Acad Sci U S A 107:9346–9351.
18. Senkevich TG, Ojeda S, Townsley A, Nelson GE, Moss B. 2005. Poxvirus multiprotein entry-fusion complex. Proceedings of the National Academy of Science of the United States of America 102:18572–18577.
19. Schin AM, Diesterbeck US, Moss B. 2021. Insights into the Organization of the Poxvirus Multicomponent Entry-Fusion Complex from Proximity Analyses in Living Infected Cells. J Virol 95:e0085221.
20. Kates J, McAuslan B. 1967. Messenger RNA synthesis by a “coated” viral genome. Proc Natl Acad Sci U S A 57:314–320.
21. Kates J, Beeson J. 1970. Ribonucleic Acid Synthesis in Vaccinia Virus I. The Mechanism of Synthesis and Release of RNA in Vaccinia Cores. J Mol Biol 50:1–18.

22. Kilcher S, Schmidt FI, Schneider C, Kopf M, Helenius A, Mercer J. 2014. SiRNA screen of early poxvirus genes identifies the AAA+ ATPase D5 as the virus genome-uncoating factor. Cell Host Microbe 15:103–112.
23. Mercer J, Snijder B, Sacher R, Burkard C, Bleck CKE, Stahlberg H, Pelkmans L, Helenius A. 2012. RNAi Screening Reveals Proteasome- and Cullin3-Dependent Stages in Vaccinia Virus Infection. Cell Rep 2:1036–1047.
24. Schmidt FI, Bleck CKE, Reh L, Novy K, Wollscheid B, Helenius A, Stahlberg H, Mercer J. 2013. Vaccinia virus entry is followed by core activation and proteasome-mediated release of the immunomodulatory effector VH1 from lateral bodies. Cell Rep 4:464–476.
25. Bidgood SR, Samolej J, Novy K, Collopy A, Albrecht D, Krause M, Burden JJ, Wollscheid B, Mercer J. 2022. Poxviruses package viral redox proteins in lateral bodies and modulate the host oxidative response. PLoS Pathog 18:e1010614.
26. Baroudy BM, Venkatesan S, Moss B. 1982. Incompletely Base-Paired Flip-Flop Terminal Loops Link the Two DNA Strands of the Vaccinia Virus Genome into One Uninterrupted Polynucleotide Chain. Cell 28:315–324.
27. Delange AM, Reddy M, Scraba D, Upton C, Mcfadden G. 1986. Replication and Resolution of Cloned Poxvirus Telomeres In Vivo Generates Linear Minichromosomes with Intact Viral Hairpin Termini. J Virol 59:249–259.
28. Shenouda MM, Noyce RS, Lee SZ, Wang JL, Lin YC, Favis NA, Desaulniers MA, Evans DH. 2022. The mismatched nucleotides encoded in vaccinia virus flip-And-flop hairpin telomeres serve an essential role in virion maturation. PLoS Pathog 18:e1010392.
29. Tarbouriech N, Ducournau C, Hutin S, Mas PJ, Man P, Forest E, Hart DJ, Peyrefitte CN, Burmeister WP, Iseni F. 2017. The vaccinia virus DNA polymerase structure provides insights into the mode of processivity factor binding. Nat Commun 8:1455.
30. Contesto-Richefeu C, Tarbouriech N, Brazzolotto X, Betzi S, Morelli X, Burmeister WP, Iseni F. 2014. Crystal Structure of the Vaccinia Virus DNA Polymerase Holoenzyme Subunit D4 in Complex with the A20 N-Terminal Domain. PLoS Pathog 10:e1003978.
31. Bersch B, Tarbouriech N, Burmeister WP, Iseni F. 2021. Solution Structure of the C-terminal Domain of A20, the Missing Brick for the Characterization of the Interface between Vaccinia Virus DNA Polymerase and its Processivity Factor. J Mol Biol 433:167009.
32. Senkevich TG, Katsafanas GC, Weisberg A, Olano LR, Moss B. 2017. Identification of Vaccinia Virus Replisome and Transcriptome Proteins by Isolation of Proteins on Nascent DNA Coupled with Mass Spectrometry. J Virol 91:e01015-17.
33. Greseth MD, Traktman P. 2022. The Life Cycle of the Vaccinia Virus Genome. Annu Rev Virol 9:239–259.
34. Beaud G, Beaud R. 1997. Preferential virosomal location of underphosphorylated H5R protein synthesized in vaccinia virus-infected cells. Journal of General Virology 78:3297–3302.

35. Welsch S, Doglio L, Schleich S, Krijnse Locker J. 2003. The Vaccinia Virus I3L Gene Product Is Localized to a Complex Endoplasmic Reticulum-Associated Structure That Contains the Viral Parental DNA. J Virol 77:6014–6028.
36. Domi A, Beaud G. 2000. The punctate sites of accumulation of vaccinia virus early proteins are precursors of sites of viral DNA synthesis. Journal of General Virology 81:1231–1235.
37. Rochester SC, Traktman P. 1998. Characterization of the Single-Stranded DNA Binding Protein Encoded by the Vaccinia Virus I3 Gene. J Virol 72:2917–2926.
38. Kay NE, Bainbridge TW, Condit RC, Bubb MR, Judd RE, Venkatakrishnan B, McKenna R, D'Costa SM. 2013. Biochemical and biophysical properties of a putative hub protein expressed by vaccinia virus. J Biol Chem 288:11470–11481.
39. Boyle KA, Greseth MD, Traktman P. 2015. Genetic Confirmation that the H5 Protein Is Required for Vaccinia Virus DNA Replication. J Virol 89:6312–6327.
40. Tolonen N, Doglio L, Schleich S, Locker JK. 2001. Vaccinia Virus DNA Replication Occurs in Endoplasmic Reticulum-enclosed Cytoplasmic Mini-Nuclei. Mol Biol Cell 12:2031–2046.
41. Zaborowska I, Kellner K, Henry M, Meleady P, Walsh D. 2012. Recruitment of host translation initiation factor eIF4G by the Vaccinia Virus ssDNA-binding protein I3. Virology 425:11–22.
42. Walsh D, Arias C, Perez C, Halladin D, Escandon M, Ueda T, Watanabe-Fukunaga R, Fukunaga R, Mohr I. 2008. Eukaryotic Translation Initiation Factor 4F Architectural Alterations Accompany Translation Initiation Factor Redistribution in Poxvirus-Infected Cells. Mol Cell Biol 28:2648–2658.
43. Katsafanas GC, Moss B. 2007. Colocalization of transcription and translation within cytoplasmic poxvirus factories coordinates viral expression and subjugates host functions. Cell Host Microbe 2:221–228.
44. Erlandson KJ, Cotter CA, Charity JC, Martens C, Fischer ER, Ricklefs SM, Porcella SF, Moss B. 2014. Duplication of the A17L Locus of Vaccinia Virus Provides an Alternate Route to Rifampin Resistance. J Virol 88:11576–11585.
45. Unger B, Mercer J, Boyle KA, Traktman P. 2013. Biogenesis of the Vaccinia Virus Membrane: Genetic and Ultrastructural Analysis of the Contributions of the A14 and A17 Proteins. J Virol 87:1083–1097.
46. Maruri-Avidal L, Domi A, Weisberg AS, Moss B. 2011. Participation of Vaccinia Virus L2 Protein in the Formation of Crescent Membranes and Immature Virions. J Virol 85:2504–2511.
47. Maruri-Avidal L, Weisberg AS, Bisht H, Moss B. 2013. Analysis of Viral Membranes Formed in Cells Infected by a Vaccinia Virus L2-Deletion Mutant Suggests Their Origin from the Endoplasmic Reticulum. J Virol 87:1861–1871.
48. Maruri-Avidal L, Weisberg AS, Moss B. 2013. Direct Formation of Vaccinia Virus Membranes from the Endoplasmic Reticulum in the Absence of the Newly Characterized L2-Interacting Protein A30.5. J Virol 87:12313–12326.
49. Resch W, Weisberg AS, Moss B. 2005. Vaccinia Virus Nonstructural Protein Encoded by the A11R Gene Is Required for Formation of the Virion Membrane. J Virol 79:6598–6609.
50. Wu X, Meng X, Yan B, Rose L, Deng J, Xiang Y. 2012. Vaccinia Virus Virion Membrane Biogenesis Protein A11 Associates with Viral Membranes in a Manner

That Requires the Expression of Another Membrane Biogenesis Protein, A6. J Virol 86:11276–11286.
51. Meng X, Rose L, Han Y, Deng J, Xiang Y. 2017. Vaccinia Virus A6 Is a Two-Domain Protein Requiring a Cognate N-Terminal Domain for Full Viral Membrane Assembly Activity. J Virol 91:2405–2421.
52. Meng X, Wu X, Yan B, Deng J, Xiang Y. 2013. Analysis of the Role of Vaccinia Virus H7 in Virion Membrane Biogenesis with an H7-Deletion Mutant. J Virol 87:8247–8253.
53. Szajner P, Weisberg AS, Lebowitz J, Heuser J, Moss B. 2005. External scaffold of spherical immature poxvirus particles is made of protein trimers, forming a honeycomb lattice. Journal of Cell Biology 170:971–981.
54. Grubisha O, Traktman P. 2003. Genetic Analysis of the Vaccinia Virus I6 Telomere-Binding Protein Uncovers a Key Role in Genome Encapsidation. J Virol 77:10929–10942.
55. Cassetti MC, Merchlinsky M, Wolffe EJ, Weisberg AS, Moss B. 1998. DNA Packaging Mutant: Repression of the Vaccinia Virus A32 Gene Results in Noninfectious, DNA-Deficient, Spherical, Enveloped Particles. J Virol 72:5769–5780.
56. Klemperer N, Ward J, Evans E, Traktman P. 1997. The Vaccinia Virus I1 Protein Is Essential for the Assembly of Mature Virions. J Virol 71:9285–9294.
57. Liu L, Cooper T, Howley PM, Hayball JD. 2014. From crescent to mature virion: Vaccinia virus assembly and maturation. Viruses 6:3787–3808.
58. Schmelz M, Beate S, Ericsson M, Wolffe EJ, Shida H, Hiller G, Griffiths G. 1994. Assembly of Vaccinia Virus: the Second Wrapping Cisterna Is Derived from the Trans Golgi Network. J Virol 68:130–147.
59. Jungwirth C, Joklik WK. 1965. Studies on “early” enzymes in HeLa cells infected with vaccinia virus. Virology 27:80–93.
60. Challberg MD, Englund PT. 1979. Purification and Properties of the Deoxyribonucleic Acid Polymerase Induced by Vaccinia Virus. J Biol Chem 254:7812–7819.
61. Challberg MD, Englund PT. 1979. The Effect of Template Secondary Structure on Vaccinia DNA Polymerase. J Biol Chem 254:7820–7826.
62. McDonald WF, Traktman P. 1994. Vaccinia Virus DNA Polymerase. In vitro analysis of parameters affecting processivity. J Biol Chem 269:31190–31197.
63. Moss B, Cooper N. 1982. Genetic Evidence for Vaccinia Virus-Encoded DNA Polymerase: Isolation of Phosphonoacetate-Resistant Enzyme from the Cytoplasm of Cells Infected with Mutant Virus. J Virol 43:673–678.
64. Sridhar P, Condit RC. 1983. Selection for temperature-sensitive mutations in specific vaccinia virus genes: isolation and characterization of a virus mutant which encodes a phosphonoacetic acid-resistant, temperature-sensitive DNA polymerase. Virology 128:444–457.
65. Traktman P, Sridhar P, Condit RC, Roberts1 BE. 1984. Transcriptional Mapping of the DNA Polymerase Gene of Vaccinia Virus. J Virol 49:125–131.

66. Earl PL, Jones E V, Moss B. 1986. Homology between DNA polymerases of poxviruses, herpesviruses, and adenoviruses: nucleotide sequence of the vaccinia virus DNA polymerase gene. Proc Natl Acad Sci U S A 83:3659–3663.
67. Li Y, Shen Y, Hu Z, Yan R. 2023. Structural basis for the assembly of the DNA polymerase holoenzyme from a monkeypox virus variant. Sci Adv 9:eadg2331.
68. Peng Q, Xie Y, Kuai L, Wang H, Qi J, Gao GF, Shi Y. 2023. Structure of monkeypox virus DNA polymerase holoenzyme. Science (1979) 379:100–105.
69. Czarnecki MW, Traktman P. 2017. The vaccinia virus DNA polymerase and its processivity factor. Virus Res 234:193–206.
70. De Silva FS, Moss B. 2003. Vaccinia Virus Uracil DNA Glycosylase Has an Essential Role in DNA Synthesis That Is Independent of Its Glycosylase Activity: Catalytic Site Mutations Reduce Virulence but Not Virus Replication in Cultured Cells. J Virol 77:159–166.
71. Klemperer N, McDonald W, Boyle K, Unger B, Traktman P. 2001. The A20R Protein Is a Stoichiometric Component of the Processive Form of Vaccinia Virus DNA Polymerase. J Virol 75:12298–12307.
72. Greseth MD, Boyle KA, Bluma MS, Unger B, Wiebe MS, Soares-Martins JA, Wickramasekera NT, Wahlberg J, Traktman P. 2012. Molecular Genetic and Biochemical Characterization of the Vaccinia Virus I3 Protein, the Replicative Single-Stranded DNA Binding Protein. J Virol 86:6197–6209.
73. Harrison ML, Desaulniers MA, Noyce RS, Evans DH. 2016. The acidic C-terminus of vaccinia virus I3 single-strand binding protein promotes proper assembly of DNA-protein complexes. Virology 489:212–222.
74. Greseth MD, Czarnecki MW, Bluma MS, Traktman P. 2018. Isolation and Characterization of vΔI3 Confirm that Vaccinia Virus SSB Plays an Essential Role in Viral Replication. J Virol 92:e01719-17.
75. Evans DH. 2022. Poxvirus Recombination. Pathogens 11:896.
76. Szostak JW, Orr-Weaver TL, Rothstein RJ, Stahl FW. 1983. The Double-Strand-Break Repair Model for Recombination. Cell 33:25–35.
77. San Filippo J, Sung P, Klein H. 2008. Mechanism of eukaryotic homologous recombination. Annu Rev Biochem 77:229–257.
78. Willer DO, Mann MJ, Zhang W, Evans DH. 1999. Vaccinia Virus DNA Polymerase Promotes DNA Pairing and Strand-Transfer Reactions. Virology 257:511–523.
79. Hamilton MD, Evans DH. 2005. Enzymatic processing of replication and recombination intermediates by the vaccinia virus DNA polymerase. Nucleic Acids Res 33:2259–2268.
80. Hamilton MD, Nuara AA, Gammon DB, Buller RM, Evans DH. 2007. Duplex strand joining reactions catalyzed by vaccinia virus DNA polymerase. Nucleic Acids Res 35:143–151.
81. Senkevich TG, Koonin E V, Moss B. 2009. Predicted poxvirus FEN1-like nuclease required for homologous recombination, double-strand break repair and full-size genome formation. Proc Natl Acad Sci U S A 106:17921–17926.
82. Evans E, Traktman P. 1987. Molecular Genetic Analysis of a Vaccinia Virus Gene with an Essential Role in DNA Replication. J Virol 61:3152–3162.

83. Evans E, Klemperer N, Ghosh R, Traktman P. 1995. The Vaccinia Virus D5 Protein, Which Is Required for DNA Replication, Is a Nucleic Acid-Independent Nucleoside Triphosphatase. J Virol 69:5353–5361.
84. De Silva FS, Lewis W, Berglund P, Koonin E V, Moss B. 2007. Poxvirus DNA primase. Proc Natl Acad Sci U S A 104:18724–18729.
85. Hutin S, Ling WL, Tarbouriech N, Schoehn G, Grimm C, Fischer U, Burmeister WP. 2022. The Vaccinia Virus DNA Helicase Structure from Combined Single-Particle Cryo-Electron Microscopy and AlphaFold2 Prediction. Viruses 14:2206.
86. Li Y, Zhu J, Guo Y, Yan R. 2024. Structural insight into the assembly and working mechanism of helicase-primase D5 from Mpox virus. Nat Struct Mol Biol 31:68–81.
87. Kerr SM, Smith GL. 1989. Vaccinia virus encodes a polypeptide with DNA ligase activity. Nucleic Acids Res 17:9039–9050.
88. Smith GL, Chan YS, Kerr SM. 1989. Transcriptional mapping and nucleotide sequence of a vacciniia virus gene encoding a polypeptide with extensive homology to DNA ligases. Nucleic Acids Res 17:9051–9062.
89. Kerr SM, Johnston LH, Odell M, Duncan SA, Law KM, Smith GL. 1991. Vaccinia DNA ligase complements Saccharomyces cerevisiae cdc9, localizes in cytoplasmic factories and affects virulence and virus sensitivity to DNA damaging agents. EMBO J 10:4343–4350.
90. Colinas R, Goebel S, Davis S, Johnson G, Norton E, Paoletti E. 1990. A DNA ligase gene in the Copenhagen strain of vaccinia virus is nonessential for viral replication and recombination. Virology 179:267–275.
91. Kerr S, Smith G. 1991. Vaccinia virus DNA ligase is nonessential for virus replication: recovery of plasmids from virus-infected cells. Virology 180:625–632.
92. Paran N, De Silva FS, Senkevich TG, Moss B. 2009. Cellular DNA Ligase I Is Recruited to Cytoplasmic Vaccinia Virus Factories and Masks the Role of the Vaccinia Ligase in Viral DNA Replication. Cell Host Microbe 6:563–569.
93. Lin Y-CJ, Li J, Irwin CR, Jenkins H, DeLange L, Evans DH. 2008. Vaccinia Virus DNA Ligase Recruits Cellular Topoisomerase II to Sites of Viral Replication and Assembly. J Virol 82:5922–5932.
94. Da Fonseca F, Moss B. 2003. Poxvirus DNA topoisomerase knockout mutant exhibits decreased infectivity associated with reduced early transcription. Proc Natl Acad Sci U S A 100:11291–11296.
95. Moyer RW, Graves RL. 1981. The Mechanism of Cytoplasmic Orthopoxvirus DNA Replication. Cell 27:391–401.
96. Pogo BGT. 1977. Elimination of naturally occurring crosslinks in vaccinia virus DNA after viral penetration into cells. Proc Natl Acad Sci U S A 74:1739–1742.
97. Pogo BG, O'Shea MT. 1978. The Mode of Replication of Vaccinia Virus DNA. Virology 84:1–8.
98. Senkevich TG, Bruno D, Martens C, Porcella SF, Wolf YI, Moss B. 2015. Mapping vaccinia virus DNA replication origins at nucleotide level by deep sequencing. Proc Natl Acad Sci U S A 112:10908–10913.

99. Garcia AD, Aravind L, Koonin E V, Moss B. 2000. Bacterial-type DNA Holliday junction resolvases in eukaryotic viruses. Proc Natl Acad Sci U S A 97:8926–8931.
100. Garcia AD, Moss B. 2001. Repression of Vaccinia Virus Holliday Junction Resolvase Inhibits Processing of Viral DNA into Unit-Length Genomes. J Virol 75:6460–6471.
101. Delange AM, Mcfadden G. 1986. Sequence-nonspecific replication of transfected plasmid DNA in poxvirus-infected cells. Proc Natl Acad Sci U S A 83:614–618.
102. Magee WC, Hostetler KY, Evans DH. 2005. Mechanism of inhibition of vaccinia virus DNA polymerase by cidofovir diphosphate. Antimicrob Agents Chemother 49:3153–3162.
103. Magee WC, Aldern KA, Hostetler KY, Evans DH. 2008. Cidofovir and (S)-9-[3-hydroxy-(2-phosphonomethoxy)propyl]adenine are highly effective inhibitors of vaccinia virus DNA polymerase when incorporated into the template strand. Antimicrob Agents Chemother 52:586–597.
104. Andrei G, Snoeck R. 2010. Cidofovir activity against poxvirus infections. Viruses 2:2803–2830.
105. Parker S, Touchette E, Oberle C, Almond M, Robertson A, Trost LC, Lampert B, Painter G, Buller RM. 2008. Efficacy of therapeutic intervention with an oral ether-lipid analogue of cidofovir (CMX001) in a lethal mousepox model. Antiviral Res 77:39–49.
106. Parker S, Crump R, Foster S, Hartzler H, Hembrador E, Lanier ER, Painter G, Schriewer J, Trost LC, Buller RM. 2014. Co-administration of the broad-spectrum antiviral, brincidofovir (CMX001), with smallpox vaccine does not compromise vaccine protection in mice challenged with ectromelia virus. Antiviral Res 111:42–52.
107. Trost LC, Rose ML, Khouri J, Keilholz L, Long J, Godin SJ, Foster SA. 2015. The efficacy and pharmacokinetics of brincidofovir for the treatment of lethal rabbitpox virus infection: A model of smallpox disease. Antiviral Res 117:115–121.
108. Grossi IM, Foster SA, Gainey MR, Krile RT, Dunn JA, Brundage T, Khouri JM. 2017. Efficacy of delayed brincidofovir treatment against a lethal rabbitpox virus challenge in New Zealand White rabbits. Antiviral Res 143:278–286.
109. Hutson CL, Kondas A V., Mauldin MR, Doty JB, Grossi IM, Morgan CN, Ostergaard SD, Hughes CM, Nakazawa Y, Kling C, Martin BE, Ellison JA, Carroll DD, Gallardo-Romero NF, Olson VA. 2021. Pharmacokinetics and Efficacy of a Potential Smallpox Therapeutic, Brincidofovir, in a Lethal Monkeypox Virus Animal Model. mSphere 6:e00927-20.
110. Adler H, Gould S, Hine P, Snell LB, Wong W, Houlihan CF, Osborne JC, Rampling T, Beadsworth MB, Duncan CJ, Dunning J, Fletcher TE, Hunter ER, Jacobs M, Khoo SH, Newsholme W, Porter D, Porter RJ, Ratcliffe L, Schmid ML, Semple MG, Tunbridge AJ, Wingfield T, Price NM, Abouyannis M, Al-Balushi A, Aston S, Ball R, Beeching NJ, Blanchard TJ, Carlin F, Davies G, Gillespie A, Hicks SR, Hoyle MC, Ilozue C, Mair L, Marshall S, Neary A, Nsutebu E, Parker S, Ryan H, Turtle L, Smith C, van Aartsen J, Walker NF, Woolley S, Chawla A, Hart I, Smielewska A, Joekes E, Benson C, Brindley C, Das U, Eyton-Chong CK,

Gnanalingham C, Halfhide C, Larru B, Mayell S, McBride J, Oliver C, Paul P, Riordan A, Sridhar L, Storey M, Abdul A, Abrahamsen J, Athan B, Bhagani S, Brown CS, Carpenter O, Cropley I, Frost K, Hopkins S, Joyce J, Lamb L, Lyons A, Mahungu T, Mepham S, Mukwaira E, Rodger A, Taylor C, Warren S, Williams A, Levitt D, Allen D, Dixon J, Evans A, McNicholas P, Payne B, Price DA, Schwab U, Sykes A, Taha Y, Ward M, Emonts M, Owens S, Botgros A, Douthwaite ST, Goodman A, Luintel A, MacMahon E, Nebbia G, O'Hara G, Parsons J, Sen A, Stevenson D, Sullivan T, Taj U, van Nipsen tot Pannerden C, Winslow H, Zatyka E, Alozie-Otuka E, Beviz C, Ceesay Y, Gargee L, Kabia M, Mitchell H, Perkins S, Sasson M, Sehmbey K, Tabios F, Wigglesworth N, Aarons EJ, Brooks T, Dryden M, Furneaux J, Gibney B, Small J, Truelove E, Warrell CE, Firth R, Hobson G, Johnson C, Dewynter A, Nixon S, Spence O, Bugert JJ, Hruby DE. 2022. Clinical features and management of human monkeypox: a retrospective observational study in the UK. Lancet Infect Dis 22:1153–1162.

111. Andrei G, Gammon DB, Fiten P, De Clercq E, Opdenakker G, Snoeck R, Evans DH. 2006. Cidofovir Resistance in Vaccinia Virus Is Linked to Diminished Virulence in Mice. J Virol 80:9391–9401.
112. Gammon DB, Evans DH. 2009. The 3′-to-5′ Exonuclease Activity of Vaccinia Virus DNA Polymerase Is Essential and Plays a Role in Promoting Virus Genetic Recombination. J Virol 83:4236–4250.
113. Gammon DB, Snoeck R, Fiten P, Krečmerová M, Holý A, De Clercq E, Opdenakker G, Evans DH, Andrei G. 2008. Mechanism of Antiviral Drug Resistance of Vaccinia Virus: Identification of Residues in the Viral DNA Polymerase Conferring Differential Resistance to Antipoxvirus Drugs. J Virol 82:12520–12534.
114. Andrei G, Fiten P, Krečmerová M, Opdenakker G, Topalis D, Snoeck R. 2022. Poxviruses Bearing DNA Polymerase Mutations Show Complex Patterns of Cross-Resistance. Biomedicines 10:580.
115. Diaz-Cánova D, Moens UL, Brinkmann A, Nitsche A, Okeke MI. 2022. Genomic Sequencing and Analysis of a Novel Human Cowpox Virus With Mosaic Sequences From North America and Old World Orthopoxvirus. Front Microbiol 13:868887.
116. Águeda-Pinto A, Matos AL de, Abrantes M, Kraberger S, Risalde MA, Gortázar C, McFadden G, Varsani A, Esteves PJ. 2019. Genetic characterization of a recombinant myxoma virus in the iberian hare (Lepus granatensis). Viruses 11:530.
117. Sprygin A, Babin Y, Pestova Y, Kononova S, Wallace DB, Van Schalkwyk A, Byadovskaya O, Diev V, Lozovoy D, Kononov A. 2018. Analysis and insights into recombination signals in lumpy skin disease virus recovered in the field. PLoS One 13:e0207480.
118. Sprygin A, Pestova Y, Bjadovskaya O, Prutnikov P, Zinyakov N, Kononova S, Ruchnova O, Lozovoy D, Chvala I, Kononov A. 2020. Evidence of recombination of vaccine strains of lumpy skin disease virus with field strains, causing disease. PLoS One 15:e0232584.

119. Kieser Q, Paszkowski P, Lin J, Evans D, Noyce R. 2019. Visualizing Poxvirus Replication and Recombination Using Live-Cell Imaging, p. 221–235. In Methods in Molecular Biology. Humana Press Inc.
120. Paszkowski P, Noyce RS, Evans DH. 2016. Live-Cell Imaging of Vaccinia Virus Recombination. PLoS Pathog 12:e1005824.
121. Lin Y-CJ, Evans DH. 2010. Vaccinia Virus Particles Mix Inefficiently, and in a Way That Would Restrict Viral Recombination, in Coinfected Cells. J Virol 84:2432–2443.
122. Brennan G, Stoian AMM, Yu H, Rahman MJ, Banerjee S, Stroup JN, Park C, Tazi L, Rothenburg S. 2023. Molecular Mechanisms of Poxvirus Evolution. mBio 14:e0152622.
123. Sambrook J, Padgett B, Tomkins J. 1966. Conditional lethal mutants of Rabbitpox Virus I. isolation of host cell-dependent and temperature-dependent mutants. Virology 28:592–599.
124. Condit R, Motyczka A. 1981. Isolation and preliminary characterization of temperature-sensitive mutants of vaccinia virus. Virology 113:224–241.
125. Condit R, Motyczka A, Spizz G. 1983. Isolation, characterization, and physical mapping of temperature-sensitive mutants of vaccinia virus. Virology 128:429–443.
126. Lackner C, D'Costa S, Buck C, Condit R. 2003. Complementation analysis of the Dales collection of vaccinia virus temperature-sensitive mutants. Virology 305:240–259.
127. Ensinger M. 1982. Isolation and genetic characterization of temperature-sensitive mutants of vaccinia virus WR. J Virol 43:778–790.
128. Fields B, Joklik W. 1969. Isolation and preliminary genetic and biochemical characterization of temperature-sensitive mutants of reovirus. Virology 37:335–342.
129. Mallardo M, Schleich S, Locker JK. 2001. Microtubule-dependent Organization of Vaccinia Virus Core-derived Early mRNAs into Distinct Cytoplasmic Structures. Mol Biol Cell 12:3875–3891.
130. Mallardo M, Leithe E, Schleich S, Roos N, Doglio L, Krijnse Locker J. 2002. Relationship between Vaccinia Virus Intracellular Cores, Early mRNAs, and DNA Replication Sites. J Virol 76:5167–5183.
131. Schindelin J, Arganda-Carreras I, Frise E, Kaynig V, Longair M, Pietzsch T, Preibisch S, Rueden C, Saalfeld S, Schmid B, Tinevez JY, White DJ, Hartenstein V, Eliceiri K, Tomancak P, Cardona A. 2012. Fiji: An open-source platform for biological-image analysis. Nat Methods 9:676–682.
132. Ptashne M, Jeffrey A, Johnson AD, Maurer F, Meyer J, Roberts TM, Sauer RT. 1980. How the X Repressor and Cro Work Review. Cell 19:1–11.
133. Shcherbo D, Murphy CS, Ermakova G V., Solovieva EA, Chepurnykh T V., Shcheglov AS, Verkhusha V V., Pletnev VZ, Hazelwood KL, Roche PM, Lukyanov S, Zaraisky AG, Davidson MW, Chudakov DM. 2009. Far-red fluorescent tags for protein imaging in living tissues. Biochemical Journal 418:567–574.

134. Mackett M, Smith GL, Moss B. 1984. General Method for Production and Selection of Infectious Vaccinia Virus Recombinants Expressing Foreign Genes. J Virol 49:857–864.
135. Lambert TJ. 2019. FPbase: a community-editable fluorescent protein database. Nat Methods 16:277–278.
136. Weisberg AS, Maruri-Avidal L, Bisht H, Hansen BT, Schwartz CL, Fischer ER, Meng X, Xiang Y, Moss B. 2017. Enigmatic origin of the poxvirus membrane from the endoplasmic reticulum shown by 3D imaging of vaccinia virus assembly mutants. Proc Natl Acad Sci U S A 114:E11001–E11009.
137. Jesus DM, Costa LT, Gonçalves DL, Achete CA, Attias M, Moussatché N, Damaso CR. 2009. Cidofovir Inhibits Genome Encapsidation and Affects Morphogenesis during the Replication of Vaccinia Virus. J Virol 83:11477–11490.
138. Connelly MC, Robbins BL, Fridland A. 1993. Mechanism of uptake of the phosphonate analog (S)-1-(3-hydroxy-2-phosphonylmethoxypropyl)cytosine (HPMPC) in Vero cells. Biochem Pharmacol 46:1053–1057.
139. Cihlar T, Chen MS. 1996. Phosphorylation of Cidofovir by Cellular Enzymes. Mol Pharmacol 50:1502–1510.
140. Mcdonald WF, Crozel-Goudot V, Traktman P. 1992. Transient Expression of the Vaccinia Virus DNA Polymerase Is an Intrinsic Feature of the Early Phase of Infection and Is Unlinked to DNA Replication and Late Gene Expression. J Virol 66:534–547.
141. Fantoni NZ, El-Sagheer AH, Brown T. 2021. A Hitchhiker's Guide to Click-Chemistry with Nucleic Acids. Chem Rev 121:7122–7154.
142. Landgraf D, Okumus B, Chien P, Baker TA, Paulsson J. 2012. Segregation of molecules at cell division reveals native protein localization. Nat Methods 9:480–482.
143. DeMasi J, Du S, Lennon D, Traktman P. 2001. Vaccinia Virus Telomeres: Interaction with the Viral I1, I6, and K4 Proteins. J Virol 75:10090–10105.
144. Ichihashi Y, Oie M, Tsuruhara T. 1984. Location of DNA-Binding Proteins and Disulfide-Linked Proteins in Vaccinia Virus Structural Elements. J Virol 50:929–938.
145. Irwin CR, Hitt MM, Evans DH. 2017. Targeting nucleotide biosynthesis: A strategy for improving the oncolytic potential of DNA viruses. Front Oncol 7:229.
146. Hollenbaugh JA, Gee P, Baker J, Daly MB, Amie SM, Tate J, Kasai N, Kanemura Y, Kim DH, Ward BM, Koyanagi Y, Kim B. 2013. Host Factor SAMHD1 Restricts DNA Viruses in Non-Dividing Myeloid Cells. PLoS Pathog 9:e1003481.
147. Julien O, Beadle JR, Magee WC, Chatterjee S, Hostetler KY, Evans DH, Sykes BD. 2011. Solution structure of a DNA duplex containing the potent anti-poxvirus agent cidofovir. J Am Chem Soc 133:2264–2274.
148. Gammon DB, Evans DH. 2009. The 3′-to-5′ Exonuclease Activity of Vaccinia Virus DNA Polymerase Is Essential and Plays a Role in Promoting Virus Genetic Recombination. J Virol 83:4236–4250.
149. Chou S. 2021. Opposite effects of cytomegalovirus UL54 exonuclease domain mutations on acyclovir and cidofovir susceptibility. Antiviral Res 195:105181.
150. Trompet E, Temblador A, Gillemot S, Topalis D, Snoeck R, Andrei G. 2021. An mhv-68 mutator phenotype mutant virus, confirmed by crispr/cas9-mediated gene

editing of the viral dna polymerase gene, shows reduced viral fitness. Viruses 13:985.
151. Taddie J, Traktman P. 1991. Genetic Characterization of the Vaccinia Virus DNA Polymerase: Identification of Point Mutations Conferring Altered Drug Sensitivities and Reduced Fidelity. J Virol 65:869–879.
152. Hall JD, Coen DM, Fisher BL, Weisslitz M, Randall S, Almy RE, Gelep PT, Schaffert PA. 1934. Generation of Genetic Diversity in Herpes Simplex Virus: An Antimutator Phenotype Maps to the DNA Polymerase Locus. Virology 132:26–37.
153. Hall JD, Woodward S. 1989. Aphidicolin Resistance in Herpes Simplex Virus Type 1 Appears To Alter Substrate Specificity in the DNA Polymerase. J Virol 63:2874–2876.
154. Hall JD, Furman PA, St Clair MH, Knopf CW. 1985. Reduced in vivo mutagenesis by mutant herpes simplex DNA polymerase involves improved nucleotide selection. Proc Natl Acad Sci U S A 82:3889–3893.
155. Tsurumi T, Maeno K, Nishiyama Y. 1987. A Single-Base Change within the DNA Polymerase Locus of Herpes Simplex Virus Type 2 Can Confer Resistance to Aphidicolin. J Virol 61:388–394.
156. Liu PK, Chang C-C, Trosko JE, Dube DK, Martin GM, Loeb LA. 1983. Mammalian mutator mutant with an aphidicolin-resistant DNA polymerase alpha. Proc Natl Acad Sci USA 80:797–801.
157. Smith TG, Gigante CM, Wynn NT, Matheny A, Davidson W, Yang Y, Condori RE, O'Connell K, Kovar L, Williams TL, Yu YC, Petersen BW, Baird N, Lowe D, Li Y, Satheshkumar PS, Hutson CL. 2023. Tecovirimat Resistance in Mpox Patients, United States, 2022-2023. Emerg Infect Dis 29:2426–2432.
158. Garrigues JM, Hemarajata P, Espinosa A, Hacker JK, Wynn NT, Smith TG, Gigante CM, Davidson W, Vega J, Edmondson H, Karan A, Marutani AN, Kim M, Terashita D, Balter SE, Hutson CL, Green NM. 2023. Community spread of a human monkeypox virus variant with a tecovirimat resistance-associated mutation. Antimicrob Agents Chemother 67:e0097223.
159. Noyce RS, Lederman S, Evans DH. 2018. Construction of an infectious horsepox virus vaccine from chemically synthesized DNA fragments. PLoS One 13:e0188453.
160. Khuperkar D, Hoek TA, Sonneveld S, Verhagen BMP, Boersma S, Tanenbaum ME. 2020. Quantification of mRNA translation in live cells using single-molecule imaging. Nat Protoc 15:1371–1398.
161. Duraffour S, Lorenzo MM, Zöller G, Topalis D, Grosenbach D, Hruby DE, Andrei G, Blasco R, Meyer H, Snoeck R. 2015. ST-246 is a key antiviral to inhibit the viral F13L phospholipase, one of the essential proteins for orthopoxvirus wrapping. Journal of Antimicrobial Chemotherapy 70:1367–1380.
162. Christen L, Seto J, Niles EG. 1990. Superinfection Exclusion of Vaccinia Virus in Virus-Infected Cell Cultures. Virology 174:35–42.
163. Doceul V, Hollinshead M, Van Der Linden L, Smith GL. 2010. Repulsion of Superinfecting Virions: A Mechanism for Rapid Virus Spread. Science (1979) 327:873–876.

164. Laliberte JP, Moss B. 2014. A Novel Mode of Poxvirus Superinfection Exclusion That Prevents Fusion of the Lipid Bilayers of Viral and Cellular Membranes. J Virol 88:9751–9768.
165. Huang I-C, Li W, Sui J, Marasco W, Choe H, Farzan M. 2008. Influenza A Virus Neuraminidase Limits Viral Superinfection. J Virol 82:4834–4843.
166. Boussier J, Levi L, Weger-Lucarelli J, Poirier EZ, Vignuzzi M, Albert ML. 2020. Chikungunya virus superinfection exclusion is mediated by a block in viral replication and does not rely on non-structural protein 2. PLoS One 15:e0241592.
167. Biggs KRH, Bailes CL, Scott L, Wichman HA, Schwartz EJ. 2021. Ecological approach to understanding superinfection inhibition in bacteriophage. Viruses 13:1389.
168. Charity JC, Katz E, Moss B. 2007. Amino acid substitutions at multiple sites within the vaccinia virus D13 scaffold protein confer resistance to rifampicin. Virology 359:227–232.
169. Yang G, Pevear DC, Davies MH, Collett MS, Bailey T, Rippen S, Barone L, Burns C, Rhodes G, Tohan S, Huggins JW, Baker RO, Buller RLM, Touchette E, Waller K, Schriewer J, Neyts J, DeClercq E, Jones K, Hruby D, Jordan R. 2005. An Orally Bioavailable Antipoxvirus Compound (ST-246) Inhibits Extracellular Virus Formation and Protects Mice from Lethal Orthopoxvirus Challenge. J Virol 79:13139–13149.
170. Lederman ER, Davidson W, Groff HL, Smith SK, Warkentien T, Li Y, Wilkins KA, Karem KL, Akondy RS, Ahmed R, Frace M, Shieh WJ, Zaki S, Hruby DE, Painter WP, Bergman KL, Cohen JI, Damon IK. 2012. Progressive vaccinia: Case description and laboratory-guided therapy with vaccinia immune globulin, ST-246, and CMX001. Journal of Infectious Diseases 206:1372–1385.
171. Elde NC, Child SJ, Eickbush MT, Kitzman JO, Rogers KS, Shendure J, Geballe AP, Malik HS. 2012. Poxviruses deploy genomic accordions to adapt rapidly against host antiviral defenses. Cell 150:831–841.
172. Park C, Peng C, Rahman MJ, Haller SL, Tazi L, Brennan G, Rothenburg S. 2021. Orthopoxvirus K3 orthologs show virus- And host-specific inhibition of the antiviral protein kinase PKR. PLoS Pathog 17:e1009183.
173. Brennan G, Kitzman JO, Rothenburg S, Shendure J, Geballe AP. 2014. Adaptive Gene Amplification As an Intermediate Step in the Expansion of Virus Host Range. PLoS Pathog 10:e1004002.
174. Banerjee S, Smith C, Geballe AP, Rothenburg S, Kitzman JO, Brennan G. 2022. Gene amplification acts as a molecular foothold to facilitate cross-species adaptation and evasion of multiple antiviral pathways. Virus Evol 8:veac105.
175. Kerr PJ, Ghedin E, DePasse J V., Fitch A, Cattadori IM, Hudson PJ, Tscharke DC, Read AF, Holmes EC. 2012. Evolutionary History and Attenuation of Myxoma Virus on Two Continents. PLoS Pathog 8:e1002950.
176. Kerr PJ, Rogers MB, Fitch A, DePasse J V., Cattadori IM, Twaddle AC, Hudson PJ, Tscharke DC, Read AF, Holmes EC, Ghedin E. 2013. Genome Scale Evolution of Myxoma Virus Reveals Host-Pathogen Adaptation and Rapid Geographic Spread. J Virol 87:12900–12915.
177. Kerr PJ, Rogers MB, Fitch A, DePasse J V., Cattadori IM, Hudson PJ, Tscharke DC, Holmes EC, Ghedin E. 2013. Comparative Analysis of the Complete Genome

Sequence of the California MSW Strain of Myxoma Virus Reveals Potential Host Adaptations. J Virol 87:12080–12089.
178. Kerr PJ, Cattadori IM, Rogers MB, Fitch A, Geber A, Liu J, Sim DG, Boag B, Eden JS, Ghedin E, Read AF, Holmes EC. 2017. Genomic and phenotypic characterization of myxoma virus from Great Britain reveals multiple evolutionary pathways distinct from those in Australia. PLoS Pathog 13:e1006252.
179. Kerr PJ, Eden J-S, Di Giallonardo F, Peacock D, Liu J, Strive T, Read AF, Holmes EC. 2019. Punctuated Evolution of Myxoma Virus: Rapid and Disjunct Evolution of a Recent Viral Lineage in Australia. J Virol 93:e01994-18.
180. Firth C, Kitchen A, Shapiro B, Suchard MA, Holmes EC, Rambaut A. 2010. Using time-structured data to estimate evolutionary rates of double-stranded DNA viruses. Mol Biol Evol 27:2038–2051.

Appendix

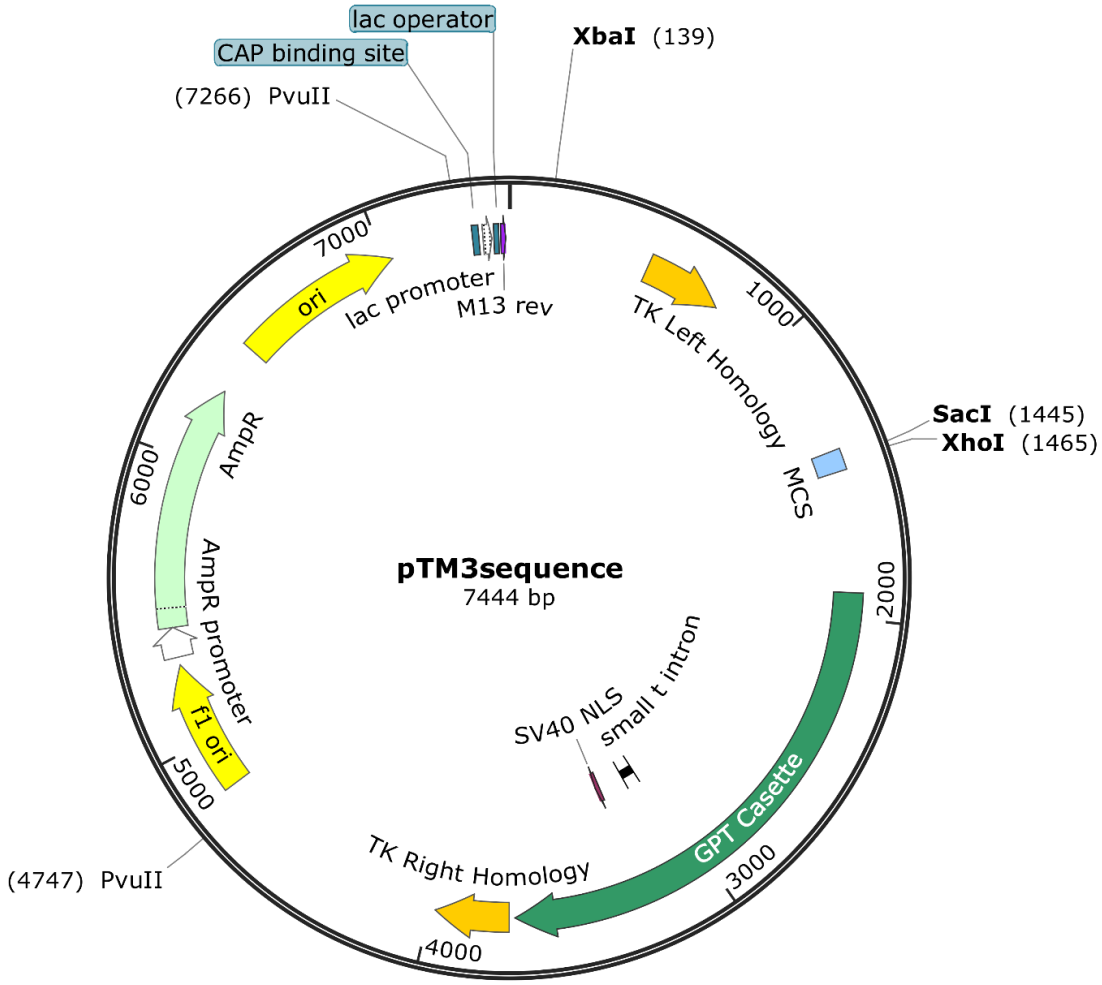

Figure A.1. Plasmid map of pTM3 shuttle vector.

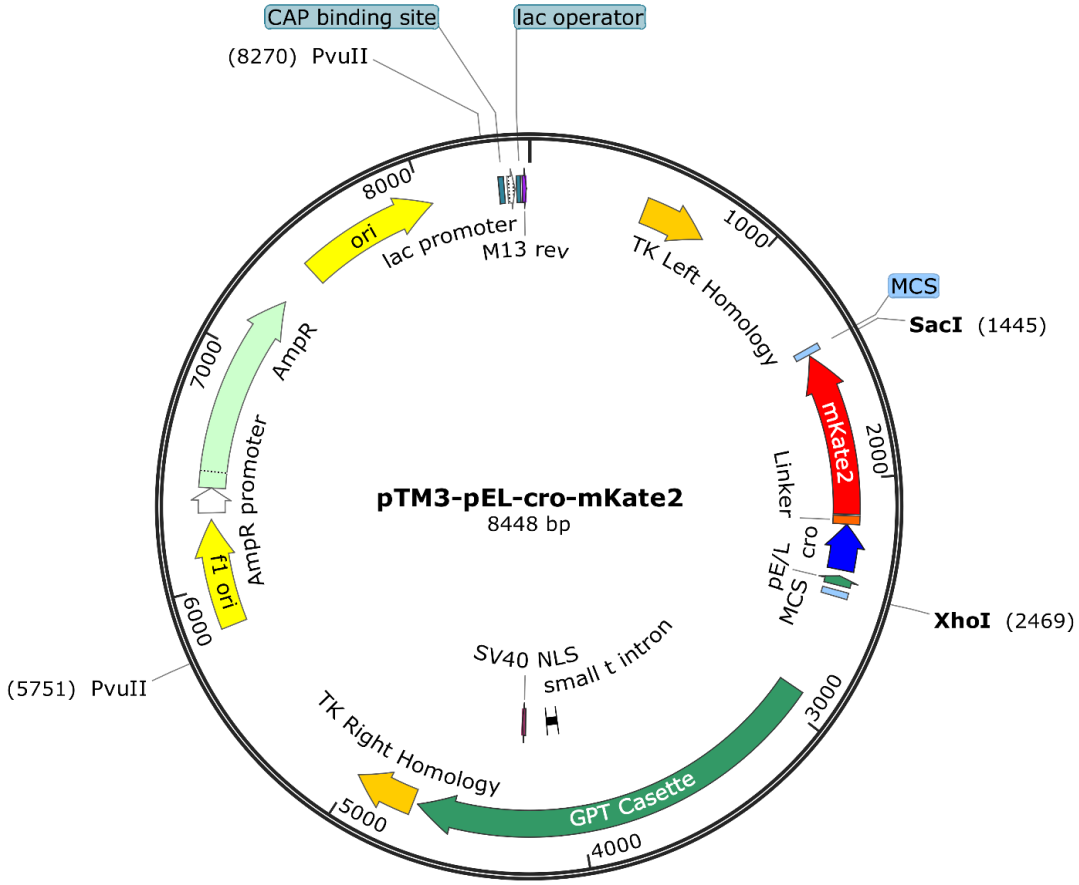

Figure A.2. Plasmid map of pTM3-pE/L-cro-mKate2. This plasmid was used to generate recombinant viruses expressing cro-mKate2 (See Methods).

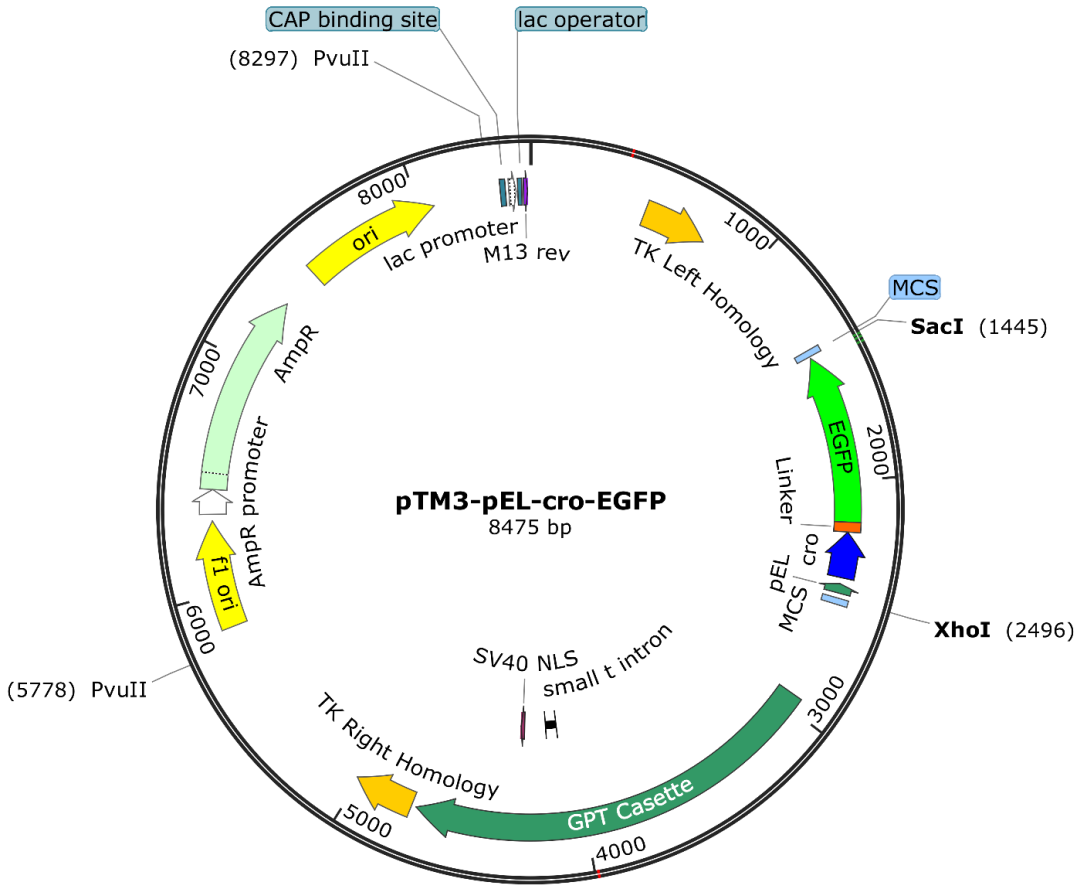

Figure A.3. Plasmid map of pTM3-pE/L-cro-EGFP. This plasmid was used to generate recombinant viruses expressing cro-EGFP (See Methods).

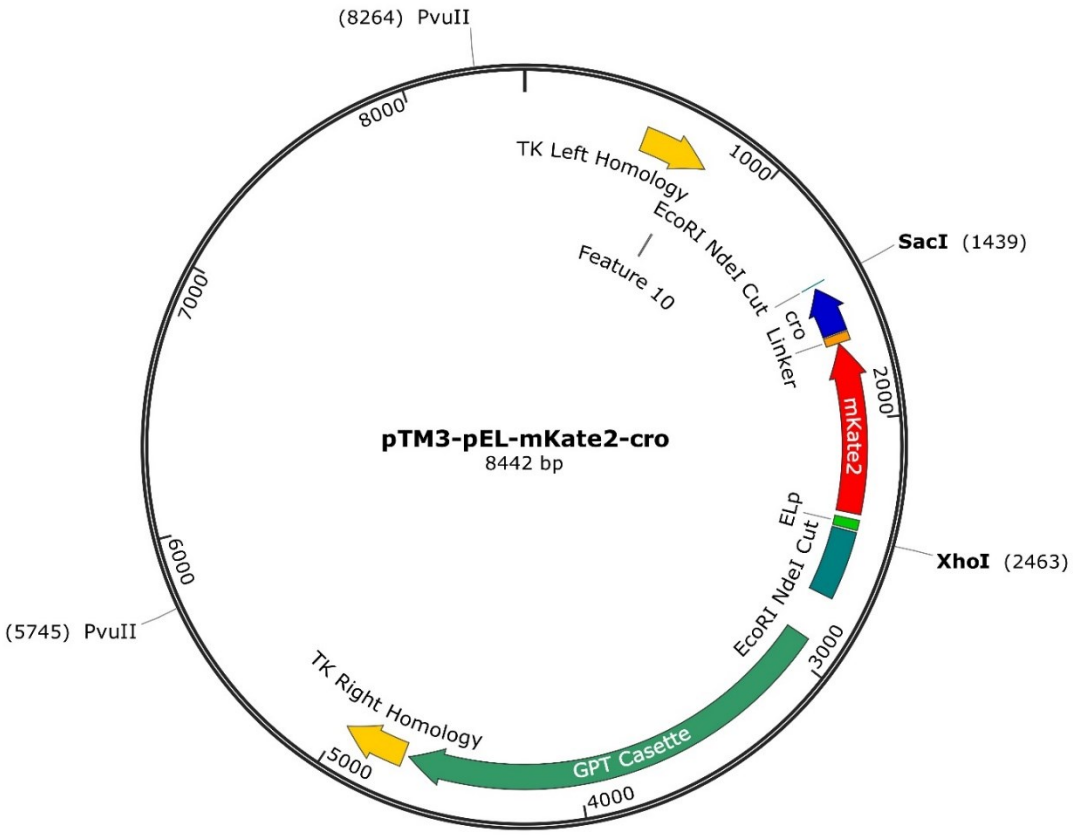

Figure A.4. Plasmid map of pTM3-pE/L-mKate2-cro. This plasmid was used to generate recombinant viruses but this was abandoned due to difficulties in purifying viruses expressing mKate2-cro or EGFP-cro.

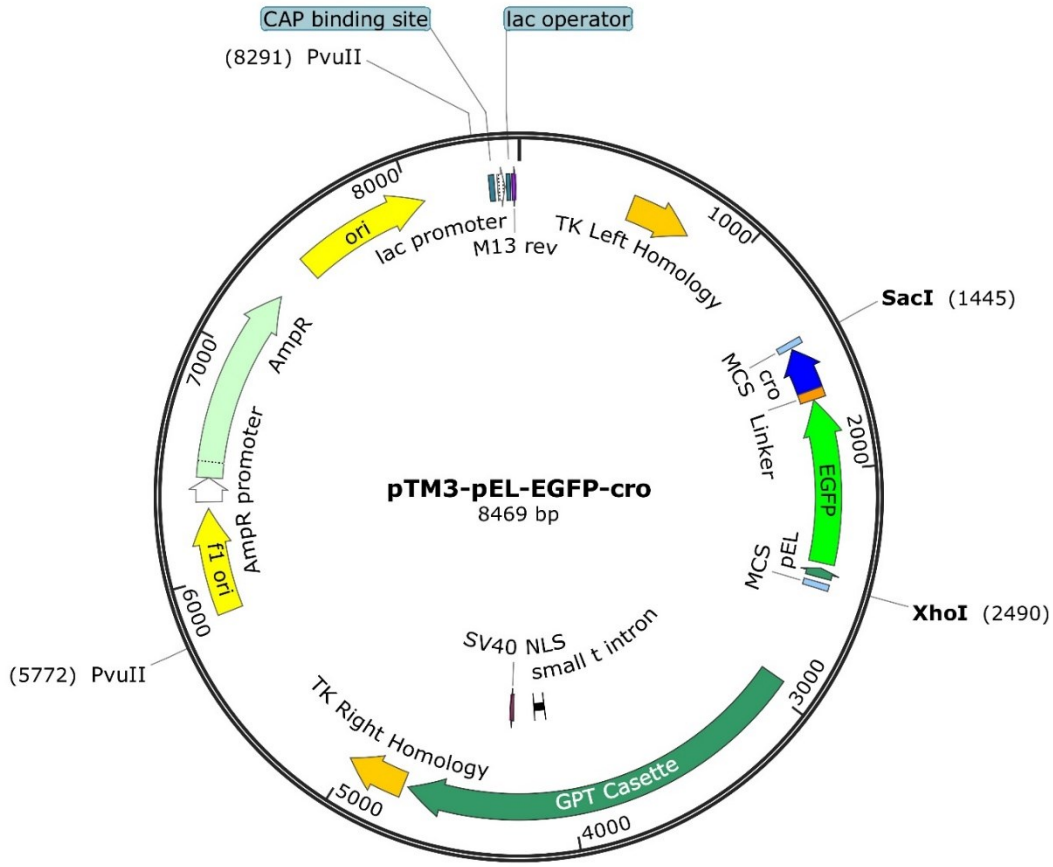

Figure A.4. Plasmid map of pTM3-pE/L-EGFP-cro. This plasmid was used to generate recombinant viruses but this was abandoned due to difficulties in purifying viruses expressing mKate2-cro or EGFP-cro.

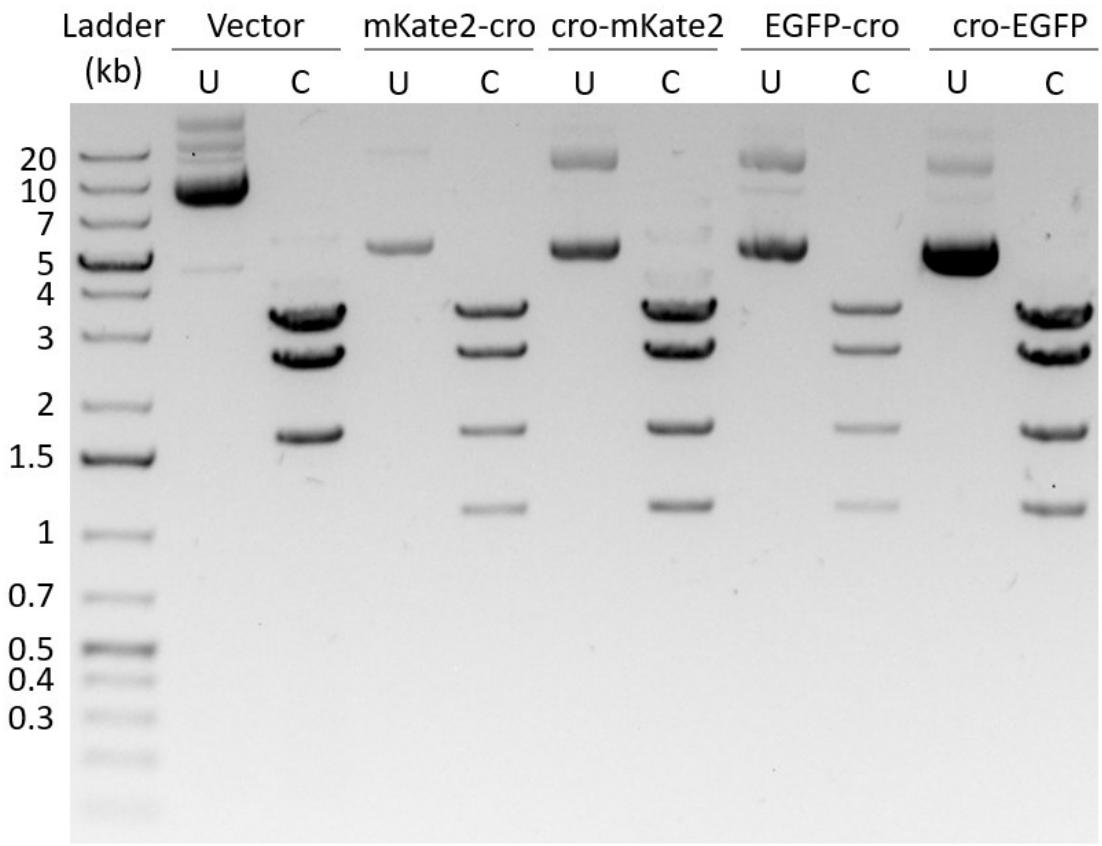

Figure A.5. Restriction digestion of recombinant pTM3 shuttle vectors carrying inserts. Plasmids were digested with *PvuII*, *SacI*, and *XhoI* enzymes (1 unit each) for 1 hour and fragments were separated on a 0.8% agarose gel. Based on the above plasmid maps, the expected fragment sizes are as follows: *SacI* → *XhoI* = 1kb; *XhoI* → *PvuII* = 3.3kb; *PvuII* → *PvuII* = 2.5kb; *PvuII* → *SacI* = 1.6kb.

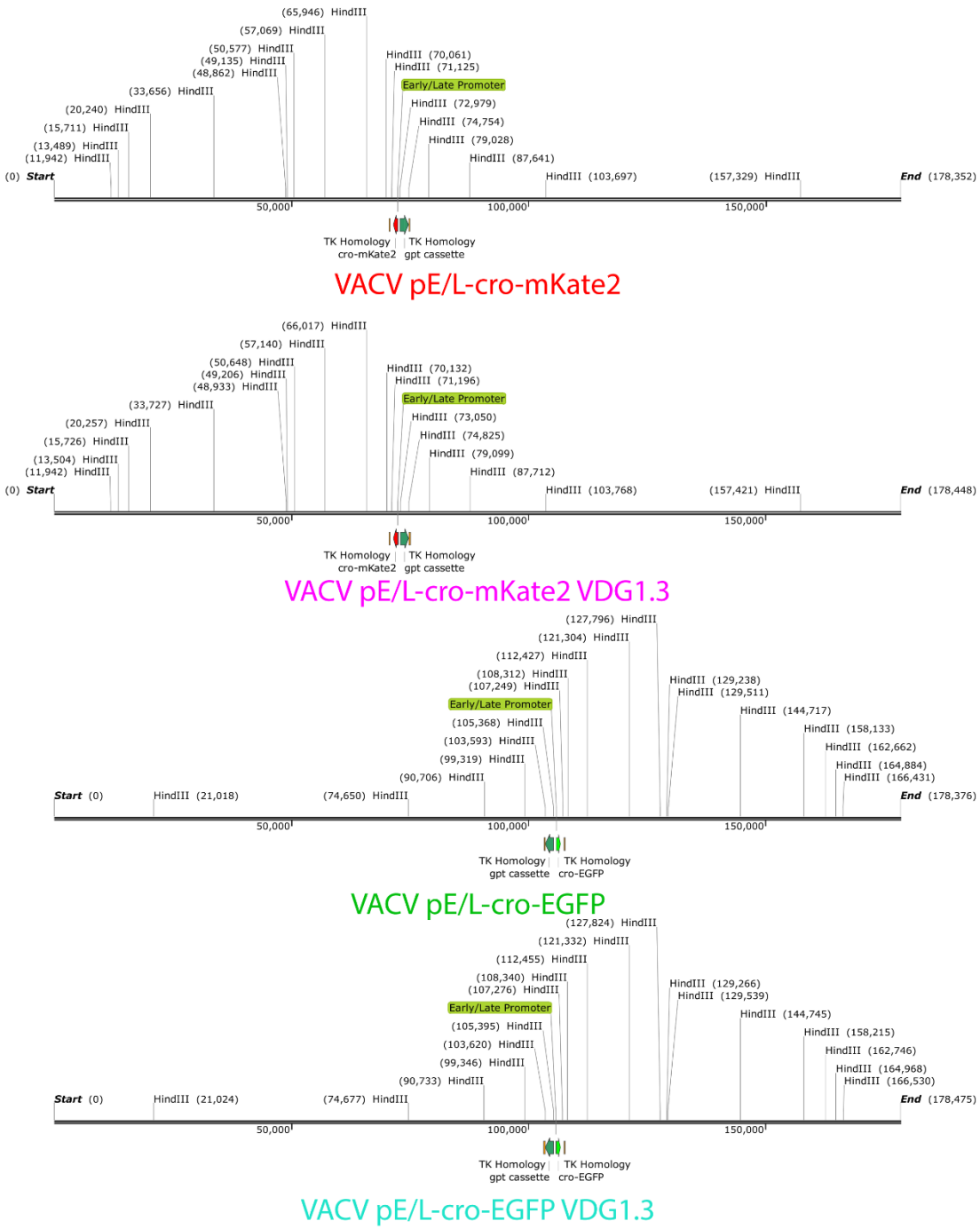

Figure A.6. Maps of recombinant viruses expressing cro-EGFP or cro-mKate2. Sequences were assembled *de novo* from NGS conducted by the University of Alberta Advanced Cell Exploration Core. Dr. Ryan Noyce helped assemble the reads.